DTU Fotonik
Department of Photonics Engineering

Validation of a Novel Solar Radiation Sensor for Use in BIPV Applications

Daniel Álvarez Mira (s171660)

Supervisors:
Nicholas Riedel
Sune Thorsteinsson
Mario Po (external)

Risø, 2020

b

Abstract

The solar radiation assessment is a key factor for this growth as it is the critical variable for all solar energy generation systems. EKO instruments has developed a sensor that integrates six photodiodes to measure solar irradiance upwards (global horizontal), downwards (ground reflected) and irradiance in all four cardinal directions for vertical surfaces. It is believed that the extra data would reduce uncertainty in prediction of PV outputs during the design phase and performance verification during the PV plant operation. This could therefore enhance the investment in vertical PV systems such as BIPV or east-west BF plants.

In the first place, an investigation on the optimal transposition model for BIPV facades with GHI as the only input was carried out. A decomposition model fitted for the studied region was created. Two different study cases were conducted with the intention of identifying the optimal transposition model among the five studied and to account for the inaccuracies that the new decomposition model might introduced to the process. The results validated the use of the new decomposition model for south facing surfaces. Nevertheless, its use for non south-facing surfaces did not show the same accuracy, which was increased when the uncertainties of the GHI sensor were taken into account. None of the anisotropic studied models can be declared as the best performing, nor does any particular model demonstrate clear advantages over the others for the location and scenarios studied here.

The measurements from the vertical sensors in the MDPD within a five month period were compared to the transposed irradiance from a PD installed nearby. The inherent errors that project developers of vertical PV systems should account for in the choice between the use of measured (MDPD) or transposed data (and the associated transposition model choice) were accurately quantified. For north facing surfaces, the average error of each predicted irradiance value over the measured one (RMSE) can be up to 11.2 W/m^2, overestimating the solar irradiance by 6 W/m^2 should they choose to not use measured data, or the optimal transposition model. In the case of a south-facing surface those errors can be up to 45.5 W/m^2 and 12.8 W/m^2 respectively. The east and west facing surfaces could show RMSE of 26.5 W/m^2 and 24.2 W/m^2, and MBE of -4.5 W/m^2 and 4.6 W/m^2 respectively.

Preface

This MSc thesis was prepared at the department of Photonics Engineering at the Technical University of Denmark in Risø, in collaboration with the company EKO Instruments Europe B.V. in partial fulfillment of the requirements for acquiring a Master of Science degree in Sustainable Energy with a specialization in Energy Savings.

Risø, February 2, 2020

Daniel Álvarez Mira (s171660)

Acknowledgements

I would like to express my gratitude to my supervisors Nicholas Riedel and Sune Thorsteinsson for giving me freedom and autonomy throughout the whole Master Thesis. They have always supported me, also given me new insights, offering constructive solutions to any challenges encountered. They helped me with my organization and always pointed me in the right direction.

A special thanks to Nicholas, for he has fed my curiosity allowing me to build my work and take inspiration especially in the unclear, and abstract beginning.

I am also very grateful for the help provided by EKO Instruments, specifically Mario Po, my supervisor in the company, who was always quick and generous with answering questions and providing useful insight and documentation.

I would also like to thank Simon, Janne and Adam, that received me, in some cases more than once, and offered their knowledge and support.

Particularly, I want to express my special gratitude to Gaspard, Emilie, Solène and Paul for offering their priceless help from a very different environment in a completely altruistic effort. And finally thank you very much to my loving family, Javier, Alberto, los TZ and The Fellowship of The Ring for their everyday support. They have been a light to me in dark places, when all other lights went out.

Contents

Abstract i

Preface iii

Acknowledgements v

Contents vii

List of Figures ix

List of Tables xi

Abbreviations and nomenclature xiii
Abbreviations . . . xiii
Nomenclature . . . xiv

1 Introduction 1
1.1 Motivation . . . 3
1.2 Content . . . 5

2 Methodology - solar radiation assessment 7
2.1 Data collection - Measurements of solar irradiance . . . 7
2.2 Data analysis - Python . . . 12
2.3 Results analysis - Statistical error indicators . . . 13
2.4 Solar irradiance modeling . . . 15
2.5 Energy assessment . . . 25

3 Decomposition model creation 27
3.1 Data acquisition and filtering . . . 27
3.2 Analysis of available data and pre-development of the model . . . 29
3.3 Curve fitting and model creation . . . 32
3.4 Decomposition model validation . . . 38

4 Transposition models 39
4.1 Optimal transposition model research . . . 39

5 MDPD assessment **55**
5.1 MDPD measurements vs transposed irradiance 55
5.2 Energy yield 62
5.3 MDPD uncertainty assessment 64

6 Conclusion **69**
6.1 Future work 72

Bibliography **75**

A BSRN recommendations for QC tests, V2.0 **79**

B Uncertainty calculations I: GHI pyranometer uncertainty in measurement assessment. Process and results. **83**
B.1 Measurement equation 84
B.2 Standard uncertainties 84
B.3 Combined standard uncertainty 89
B.4 Expanded uncertainty 90
B.5 Application of the uncertainty measurement 90

C MDPD plots and graphs. **91**
C.1 MDPD north sensor additional plots 92
C.2 MDPD south sensor additional plots 93
C.3 MDPD east sensor additional plots 94
C.4 MDPD west sensor additional plots 95

D Uncertainty calculations II: MDPD uncertainty in measurement assessment. Process and results. **97**
D.1 Measurement equation 98
D.2 Standard uncertainties 98
D.3 Combined standard uncertainty 100
D.4 Expanded uncertainty 101

List of Figures

1.1 Total anthropogenic greenhouse gas emissions (GtCO2eq/yr) by economic sector in 2010. Source: [3] 1
1.2 UNEP information on PV development and price reductions. Source [7] . 2
1.3 Renewable capacity growth between 2019 and 2024 by technology. Source: [14] 4

2.1 MDPD manufactured by EKO Instruments 8
2.2 MS-802F thermopile pyranometer manufactured by EKO Instruments. Source: [17] 9
2.3 ML-02 photodiode pyranometer manufactured by EKO Instruments. Source: [18] 10
2.4 Annual solar radiation in six Danish regions as defined in the Design Reference Year (DRY). The location of the Risø campus is circled in red. Source: [19] 11
2.5 Pictures from the main weather station at DTU campus in Risø 12
2.6 Python's development environment used (Spyder 3.3.6) 13
2.7 Diagram of the process to estimate irradiance on tilted surfaces as a function of the available data 15
2.8 Components of the global horizontal irradiance. Source: [23]. 16
2.9 Comparison of three piecewise decomposition models. (Blue = Erbs, Red = Orgill and Hollands, and Green= Reindl et al. Model 1). The blue data points are hourly averaged measurements from Florida for September 2013. Source: [26] 17
2.10 Reindl decomposition models compared to measured data. Source: [28] . 18
2.11 Radiation components over a tilted surface. Source: [23] 19

3.1 Measured data from February 14^{th} 2017 to November 15^{th} 2019 after filters have been applied 30
3.2 Raw data measured every 10 seconds and resampled at different frequencies 31
3.3 Measured and averaged raw data versus averaged data at different resample frequencies 32
3.4 Hourly averaged data and weighted curve used to create the decomposition model 33

3.5 Subplot of different parameters behavior for great clearness index values . 34
3.7 Relative humidity relation with diffuse fraction and clearness index 35
3.6 Correlation matrix between the diffuse fraction and other parameters . . . 36
3.8 Piecewise curve fitting with three different linear functions for the creation of the decomposition model 37
3.9 Piecewise curve fitting with three different linear functions for both the creation and validation datasets 38

4.1 Aerial view of the testing field at Risø 40
4.2 Diagram of the process followed to identify the optimal transposition model and validate the decomposition model 40
4.3 Pyranometer on fixed tilt array. 41
4.4 Comparison between measured and transposed irradiance on a 25°tilted surface 44
4.5 Scenario 1 metrics comparison for the different transposition models . . . 45
4.6 Daily RMSE over the daily averages of clearness index for scenario 1 and different transposition models 46
4.7 Pyranometer on the horizontal single axis tracker system 47
4.8 Evolution of the single axis tracker inclination throughout a day. 49
4.9 Evolution of the single axis tracker inclination throughout a day. 49
4.10 Comparison between measured and transposed irradiance on the surface of the single axis tracker 50
4.11 Scenario 2 metrics comparison for the different transposition models . . . 51
4.12 Polar plot comparing measured irradiance versus calculated with the Reindl transposition model 52
4.13 Scenario 2 metrics comparison for the different transposition models only for surface inclinations between 50 and 60° 53

5.1 MDPD measured data in October 2019 56
5.2 MDPD measurements for different sky conditions and year season 57
5.3 Inclinometers raw data for both axis of the MDPD 58
5.4 Inclinometers data for both axis of the MDPD after adjustments 59
5.5 Metrics comparison for each transposition model grouped by sensor . . . 59
5.6 Comparison of outliers for east and west facing sensors for the Perez transposition model 60
5.7 BIVP system defined in PVsyst to make energy comparisons 62
5.8 Error from Pvsysts "retransposition" method 63
5.9 Kernel density estimation of the expanded uncertainty for all the MDPD sensors 65
5.10 Expanded uncertainty of the different MDPD sensors for two different days as function of time of day 66
5.11 Density distributions of the difference between the uncertainty of MDPD vertical sensors measurements and the GHI measurements uncertainty . . 67

5.12 Metrics comparison for the south sensor accounting on the GHI PD and the MDPD uncertainties 68

B.1 Directional response uncertainty as a function of the zenith angle. 88
B.2 Evolution of the uncertainty in the GHI measurement for two sunny days 90

C.1 Comparison between the MDPD north sensor measured irradiance and transposed to that surface 92
C.2 Comparison between the MDPD south sensor measured irradiance and transposed to that surface 93
C.3 Comparison between the MDPD east sensor measured irradiance and transposed to that surface 94
C.4 Comparison between the MDPD west sensor measured irradiance and transposed to that surface 95

D.1 Laboratory measurements of the directional response error as a function of the angle of incidence. 99
D.2 Directional response contribution to the sensitivity's uncertainty as a function of the angle of incidence. 99

List of Tables

2.1 Comparison of characteristics between thermopile and photodiode pyranometers used in this study 10
2.2 Coefficients for the Perez diffuse irradiance model[35] 23

4.1 Filtering conditions applied to the dataset for scenario 1 42
4.2 Available data rows for scenario 1 after each of the data processing steps . 42
4.3 Filtering conditions applied to the dataset for scenario 2 48
4.4 Available data rows for scenario 2 after each of the data processing steps . 48

5.1 Filtering conditions applied to the data used for the MDPD assessment . 56
5.2 Available data rows for scenario 2 after each of the data processing steps . 58

B.1 Standard uncertainty estimation for common distributions. Source: NREL [46] 85
B.2 EKO MS-802F pyranometer specifications. 86
B.3 Summary of uncertainty contributions for the MS-802F pyranometer . . . 88

B.4 Standard uncertainties for the measurement equation parameters of the MS-802F. 89

D.1 Summary of uncertainty contributions 100
D.2 Standard uncertainties for the measurement equation parameters. 100

Abbreviations and nomenclature

Abbreviations

AI	Anisotropy Index
AM	Air Mass
AOI	Angle Of Incidence
BF	Bifacial
BIPV	Building Integrated Photovoltaics
BSRN	Baseline Surface Radiation Network
CET	Central European Time
DHI	Diffuse Horizontal Irradiance
DMI	Danish Meteorological Institute
DNI	Direct Normal Irradiance
DrHI	Direct beam irradiance on a horizontal surface
DST	Daylight Saving Time
DTU	Technical University of Denmark (Danmarks Tekniske Universitet)
FPV	Floating Photovoltaics
GHI	Global Horizontal Irradiance
IEA	International Energy Agency
IPCC	Intergovernmental Panel on Climate Change
MAPE	Mean Absolute Percentage Error
MBE	Mean Bias Error
MDPD	Multi-directional Photodiode
MSE	Mean Square Error

NREL	National Renewable Energy Laboratory
PD	Photodiode
POA	Plane Of Array
PV	Photovoltaic
QC	Quality Control
RMSE	Root Mean Square Error
RSS	Root Sum of Squares
SQL	Structured Query Language
U	Expanded uncertainty
u	Standard uncertainty

Nomenclature

β	Surface inclination of the solar collector
γ	Surface azimuth
ϵ	Sky's clearness
γ_S	Solar azimuth angle
θ	Angle of incidence (AOI)
θ_z	Zenith angle
ρ_g	Ground albedo
AI	Anisotropy Index
C_n	Calculated data points
DF	Diffuse fraction
DHI	Diffuse Horizontal Irradiance
DNI	Direct Normal Irradiance
DrHI	Direct beam irradiance on a horizontal surface
E_0	Extraterrestrial irradiance on a horizontal surface
E_{0n}	Extraterrestrial irradiance on a surface normal to the sun
GHI	Global Horizontal Irradiance
I_b	Direct or beam radiation
$I_{b,POA}$	Direct radiation on a tilted surface

I_d	Diffuse radiation
I_{POA}	Total radiation on a tilted surface
I_r	Ground reflected irradiance
K_t	Clearness index
M_n	Measured data points
R_b	Geometric factor (ratio of beam radiation on a tilted surface to that on a horizontal surface)

CHAPTER 1

Introduction

97% of the scientific community agree that climate change trends over the past century are certainly a result of human activities [1]. Most of the worldwide scientific organizations such as Intergovernmental Panel on Climate Change (IPCC) or the U.S. Global Change Research Program, have endorsed this opinion [2].

Electricity generation is currently one of the main source of greenhouse gas emissions, which are considered as the main cause of climate change. In fact, according to the IPCC it represents 25% of global emissions [3]. Figure 1.1 shows the breakdown of those gases emissions by economic sector.

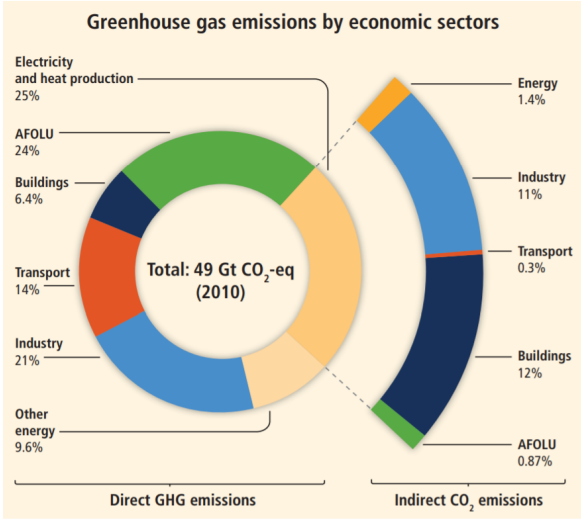

Figure 1.1: Total anthropogenic greenhouse gas emissions (GtCO2eq/yr) by economic sector in 2010. Source: [3]

Beginning in the late 1990s, several agreements and efforts at the international level have been launched, namely the Kyoto protocol in 1997, the pact at the COP 21 summit in 2015 and the 2020 targets proposed by the European Commission.

These agreements are leading a middle term transition to a full sustainable energy generation system. Nonetheless, latest findings and studies already predict inevitable catastrophic consequences from climate change should improvement continue at the current, actual rate. The Paris agreement (2016) set the global mean temperature increase limit to 2°C above the pre-industrial baseline (1850-1900), and to pursue efforts to limit the increase to 1.5 °C to avoid irreversible consequences. Nevertheless, in 2018 the global mean temperature was estimated to be 1°C above this limit already. The consequences of the impact of global warming of 1.5°C have been reported to highlight the need for strengthening the global response to the threat of climate change, and the need of sustainable development and poverty eradication [4–6].

In the solar photovoltaic (PV) energy field, innovation and incentive policies have shaped the way PV energy is developing, seen to be constantly exceeding forecasts (Figure 1.2a). Many factors have driven down PV cost dramatically. A combination of economies of scale, R&D and lowered profit margins through increasing competition have made PV prices fall by about 99.5% from 1975 to 2016 (Figure 1.2b) [7]. At the end of 2018, the combination of these innovation, cost reductions and supportive policies led to a total PV power generation capacity of 486 GW, almost 20 times more than it was in 2009 [8].

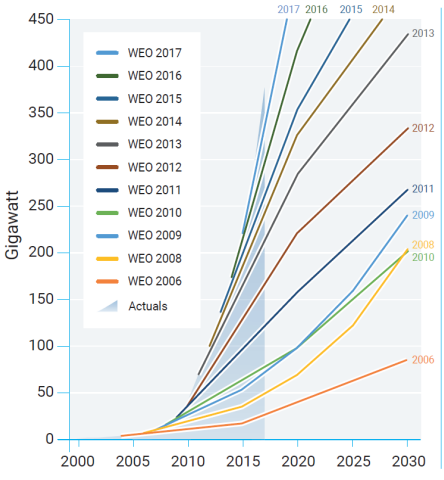

(a) Cumulative solar PV installations compared to forecasts from various IEA World Energy Outlooks (WEO)

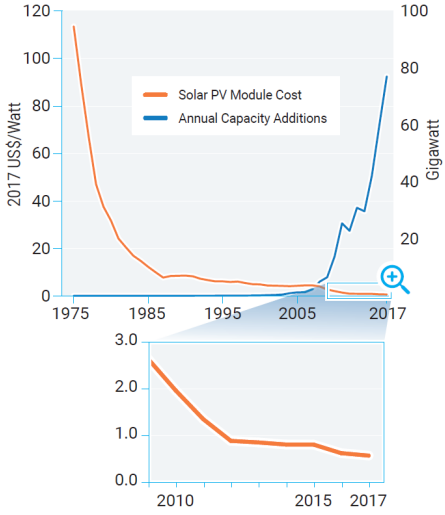

(b) Historical price reductions and annual installations, 1975–2017

Figure 1.2: UNEP information on PV development and price reductions. Source [7]

These efforts have led to both the development of new, more efficient photovoltaic cells, such as tandem cells which currently show a maximum efficiency around 40% [9]; alongside the design of new PV systems such as bifacial (BF) modules and building integrated photovoltaic (BIPV) systems. BF modules produce solar power from both sides of the panel and manufacturers claim up to a 30% increase in production can be achieved just from the extra power generated from the rear. At the end of 2019, the total installed BF capacity was equal to 8.2 GW and its share of the total annual installed capacity is expected to be 17% by 2024, quadrupling its current share [10]. On the other side, BIPV are PV products that are fully integrated with building materials. Despite the efforts and high stakeholder interest in building-integrated PV (BIPV), the deployment of PV systems that are partially or fully integrated with building materials is low compared with rack-mounted PV systems [11].

Other emerging designs are just entering the PV market such as floating solar photovoltaic (FPV) systems. FPV is an emerging technology in which a PV system is placed directly atop a body of water. FPV installations have grown rapidly from an installed capacity of 90 MW in 2016 to 587 MW in 2018. Moreover, annual FPV installations are expected to grow over 1.5 GW yearly until 2022 [12]. On the other hand, companies such as Next2Sun are investigating the advantages of vertical BF systems. This design generates energy peaks where conventional installations do not, which would help balancing the sustainable energy production . Additionally, the wider distance between rows will make it possible to keep use the land simultaneously for agricultural purposes [13].

1.1 Motivation

According to the International Energy Agency (IEA), the capacity of renewable power is set to expand by 50% before 2024. An increase of 1200 GW led by solar photovoltaic is expected. Solar PV accounts for the majority (60%) of the expected growth, followed by onshore wind with approximately one-quarter (Figure 1.3). IEA reports show a 26% higher forecast in the accelerate case where governments address the following challenges: policy and regulatory uncertainty; high investment risks in developing countries; and system integration of wind and solar in some countries [14].

The solar radiation assessment is a key factor for this growth as it is the critical variable for all solar energy generation systems. Measured solar irradiance provides knowledge to make important decisions on future energy yield, efficiency, performance and maintenance, which are crucial factors for investments.

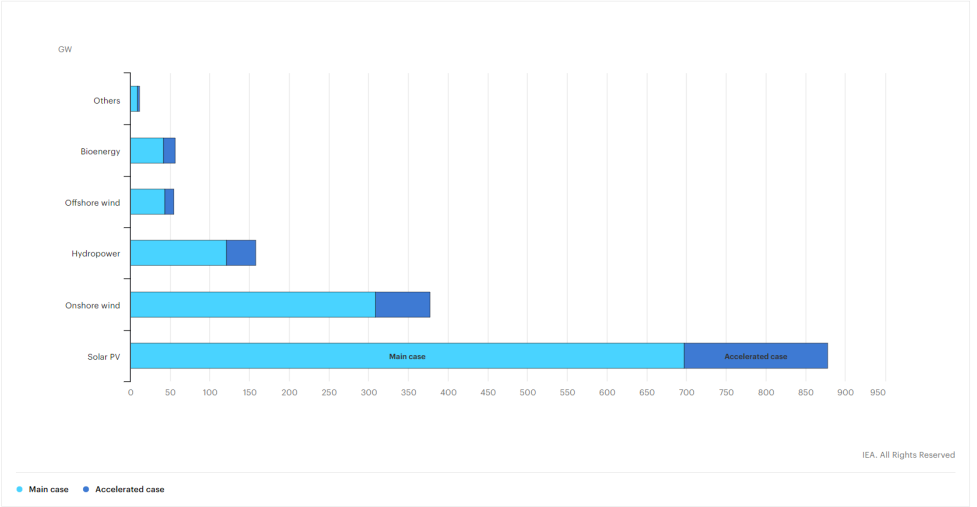

Figure 1.3: Renewable capacity growth between 2019 and 2024 by technology. Source: [14]

Significantly smaller plane of array (POA) irradiances computed by the transposition models are observed when the PV panel deviates from the azimuthal direction of the sun. Reducing uncertainty in the prediction and/or verification of PV plant output can directly increase the expected return on investment for each party in a contract, likely leading to more favorable terms for the contract, including a possible reduction in interest rates [15, 16].

Therefore, in order to enhance the investment in BIPV, EKO instruments has developed a sensor that integrates six photodiodes to measure solar irradiance upwards (global horizontal), downwards (ground reflected) and irradiance in all four cardinal directions for vertical surfaces. With regards to BIPV applications, it is believed that the extra data would reduce uncertainty in prediction of PV outputs during the design phase and performance verification during the PV plant operation, hence contribute to the expected PV growth. Additionally, the extra data measured by the MDPD is expected to benefit not only BIPV applications, but other systems such as BF were the ground reflected irradiance measurements could reduce uncertainties in the solar irradiance assessment.

In order to validate the MDPD sensor, a study has been carried out where the main purpose was to perform a quantitative analysis of the error that project developers risk if they do not use the correct transposition model or the extra information provided by the sensor for their solar resource assessment. For this purpose, an investigation on the optimal transposition model for BIPV facades with GHI as the only

input will be carried out.

1.2 Content

The following sections of the report provide an structured explanation of the process followed to achieved the project's objectives. In **Chapter 2**, the methodology created to achieve the objectives of the present study are detailed: starting with a description of how the data has been collected and analyzed; followed by a brief explanation regarding solar irradiance assessment and modeling; completed with a comment on how the MDPD benefits are evaluated. Results are divided in the following three chapters with their corresponding discussion enclosed. In the first of them, **Chapter 3**, all the details regarding the decomposition model construction are explained. In **Chapter 4**, two different scenarios with the available resources are set up to identify the optimal transposition model for the studied location and to validate the created decomposition model. Following this quantitative study on the optimal transposition model, in **Chapter 5** the MDPD benefits over commonly used irradiance modeling tools. The numerical model created in Chapter 3 alongside the aforementioned transposition models are tested against the MDPD measurements, as well as an uncertainty evaluation on the MDPD measurements. **Chapter 6** serves as a summary of the work carried out, where the conclusions extracted are detailed and future steps and propositions are presented to culminate the report. Additionally, the appendixes contain extra plots, information, and calculations made in parallel such as data filtering conditions or uncertainty in the measurements calculations.

CHAPTER 2

Methodology - solar radiation assessment

In this chapter, the methodology used through the project in order to assessing potential advantages of the MDPD sensor is described. In the first place, solar irradiance measurements from different sensors were used to identify the optimal transposition model for vertical surfaces in climate regions similar to Denmark. Finally, measured irradiance from the MDPD was compared with transposed data from horizontal measurements to show how PV yield predictions are affected by the use of one method over the other, and the associated bias error.

To that end, the following steps were followed. In the first place, the sensors used in the data collection process are described, as well as the location where the study was conducted. Secondly, it is explained how the data was treated and the different statistical error indicators used to assess the results. Then, the process to evaluate solar irradiation on tilted planes is explained. In order to identify the optimal transposition model to use when only GHI measurements are available, decomposition models and transposition models (the ones studied within the scope of this project) are defined in Sections 2.4.1 and 2.4.2 respectively. Finally, Section 2.5 describes the processes followed to answer the question: what is the bias error that BIPV project developers risk by choosing one transposition model over others, or by not using MDPD measurements?

2.1 Data collection - Measurements of solar irradiance

Three different types of pyranometers have been used to measure solar irradiance for decades. These instruments can be grouped in two different technologies: thermopile or silicon semiconductor, which have very different characteristics such as response time or spectral response. Thermopile pyranometers are a ”pile” of thermocouples that measure irradiance as a temperature difference between the junction exposed to solar radiation (the hot junction) and the one that are protected from it (the cold junction). On the other side, silicon semiconductors are photodiode-based pyranome-

ters, which operate using the photoelectric principle. There are two different types of silicon semiconductor sensors. The first type is the silicon pyranometer (referred as PD in this report) which uses a photodiode and a diffuser or optical filters. The second type is a photovoltaic pyranometer (most commonly referred as reference cells) which is made of a small photovoltaic cell working at or near short-circuit conditions.

The main sensors used during this project are the MS-802F pyranometer and the ML-02 fast-silicon photodiode both manufactured by EKO Instruments. The multi-directional photodiode (MDPD) analyzed in this thesis integrates six of the ML-02 sensors into a 3D printed sphere (Figure 2.1). Other irradiance sensors were used such as a pyrheliometer to measure direct normal irradiance (DNI) and another MS-802F pyranometer with a shading ball to measure diffuse horizontal irradiance (DHI). Both of these sensors were used to create a decomposition model. Two additional thermopile pyranometers measuring solar irradiance in the plane of a 25°static tilt and a horizontal single axis tracker array were used for comparing to the transposition modeling results. Nevertheless, only the MF-802F and the ML-02 will be described in depth due to their relevance for the project.

Figure 2.1: MDPD manufactured by EKO Instruments

2.1.1 MS-802F Pyranometer

The MS-802F pyranometer is a high-precision thermopile pyranometer (Figure 2.2). It is designed to be used in outdoor environments for photovoltaic or meteorological applications. The MS-802F is a ISO 9060:2018 Class A sensor able to measure global broad-brand solar irradiance with high accuracy. This version of the MS-802 includes a ventilation system to minimize the negative effect of frost, snow and dust. It was last calibrated in September 2017. The most relevant characteristics of the MS-802F pyranometer can be seen in Table 2.1 where they are compared with those of the ML-02.

Figure 2.2: MS-802F thermopile pyranometer manufactured by EKO Instruments. Source: [17]

2.1.2 Multi-directional photodiode (MDPD)

The MPDP sensor is the object of analysis in this project. It integrates six ML-02 sensors fabricated by EKO Instruments. The ML-02 is a low-profile silicon-pyranometer (PD) classified as ISO 9060:2019 Class C. It integrates a UV resistant diffuser that gives a proper cosine response (even at low incident angles) and it is shaped to avoid effects of soiling, lingering water and dust. EKO claims that compared to reference cells, the ML-02 sensor is more compact and has an ideal cosine response. This means that the sensor has equivalent behavior in terms of response time, spectral and temperature response. These characteristics, combined with its compact dimensions make it easy to integrate within any application e.g. the MDPD itself, BIPV systems or East-West vertical bifacial PV installations.

Figure 2.3: ML-02 photodiode pyranometer manufactured by EKO Instruments. Source: [18]

Table 2.1 summarizes the most relevant differences between both described sensors. These characteristics and their effects on the measurement's uncertainty are further detailed in Appendixes B and D.

Table 2.1: Comparison of characteristics between thermopile and photodiode pyranometers used in this study

Parameter	MS-802F	ML-02
ISO 9060:2018 class	Class A	Class C
Sub-category "Spectrally flat"	Compliant	Not compliant
Sub-category "fast response"	Not compliant	Compliant
Output	Analog (mV)	Analog (mV)
Response time 95%	< 5 sec	< 1 ms
Zero off-set a)	$< 6\ W/m^2$	$0\ W/m^2$
Zero off-set b)	$\pm\ 2\ W/m^2$	$0\ W/m^2$
Complete zero off-set c)	-	$0\ W/m^2$
Non-stability change/1 year	$\pm$ 0.5 %	$\pm$ 2 %
Non-linearity at 1000 W/m^2	$\pm$ 0.2 %	$<$ 0.2 %
Directional response at 1000 W/m^2	$\pm\ 10\ W/m^2$	$< 10\ W/m^2$
Spectral error	$\pm$ 0.23 %	$\pm$ 3.07 %
Temperature response -10°C + 40°C	$\pm$ 1 %	$<$ 0.15 %/°C
Temperature response -20°C + 50°C	$\pm$ 1 %	-
Tilt response	$\pm$ 0.2 %	0 %
Operating temperature range	[-40, 80] °C	[-30, 70] °C
Irradiance range	[0, 4000] W/m^2	[0, 2000] W/m^2
Wavelength range	[285, 3000] nm	[400, 1100] nm

2.1.3 Study location

All the above described sensors are located at DTU's campus in Risø (55.693°N; 12.100°E; 12m above mean sea level). Risø campus is located in the eastern Sealand region (Figure 2.4), which belongs to the fifth solar radiation zone defined by the

Danish Meteorological Institute (DMI).

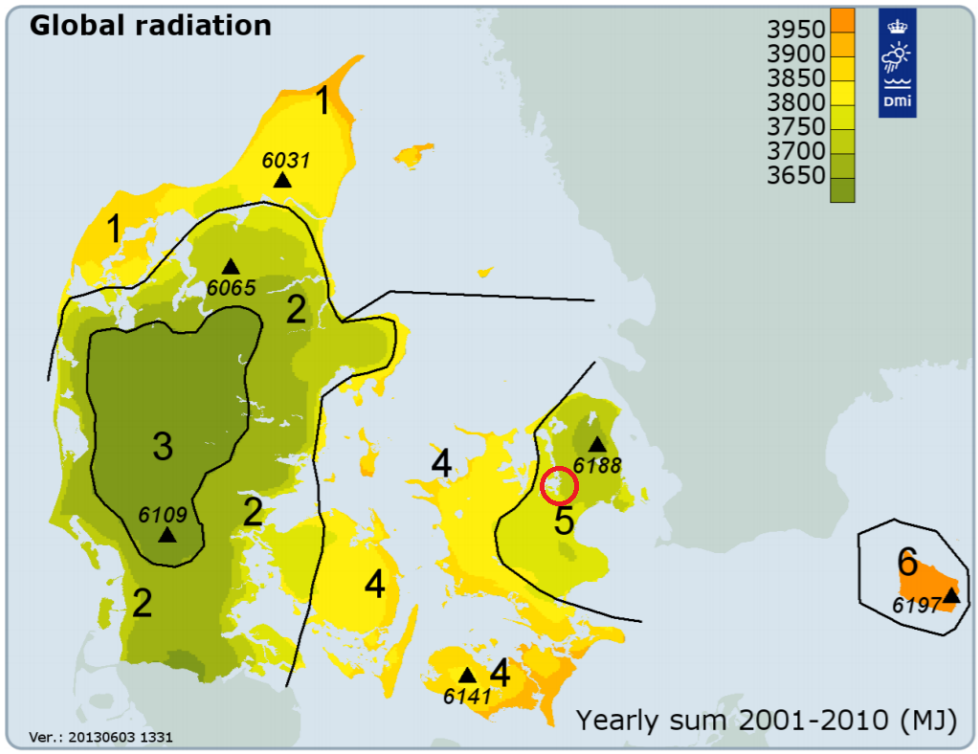

Figure 2.4: Annual solar radiation in six Danish regions as defined in the Design Reference Year (DRY). The location of the Risø campus is circled in red. Source: [19]

The DTU Fotonik facilities are divided in two locations that contain sensors for the measurement of solar radiation: Building 130 (referred as main weather station), and the testing field situated about 400 meters north from this building (bifacial PV testing field).

The sensors at the main weather station were the most used during this project, while the two pyranometers in the testing field were used only for comparisons to find optimal transposition models and to validate the decomposition model. In Figure 2.5 different views of the main weather station and some of the installed sensors can be seen. Figure 2.5c shows the MDPD (sphere in the top center area) already set up in the main weather station as well as the MS-802F sensor you used for decomposition and transposition (in the foreground).

(a) Main weather station aerial view

(b) Main weather station sensors

(c) Main weather station MDPD

Figure 2.5: Pictures from the main weather station at DTU campus in Risø

2.2 Data analysis - Python

All available meteorological data and irradiance measurements were analyzed with the programming language Python 3.7 [20]. Python's development environment Spyder 3.3.6 was used to code all calculations and plot results. Figure 2.6 shows a caption of Spyder's environment. Structured Query Language (SQL) was used to access all collected and stored data in DTU's database. SQL is a domain-specific language where

the main advantage is the ability of accessing many records with one single command.

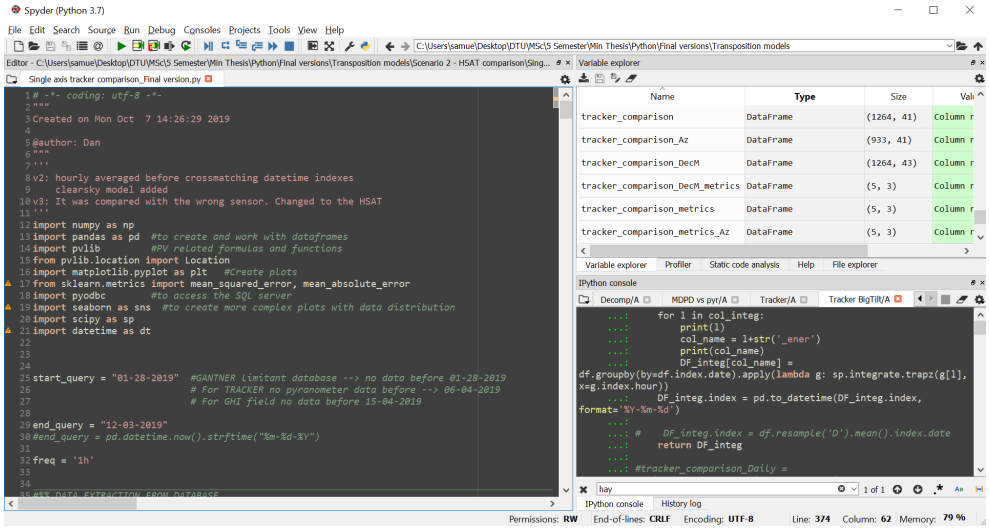

Figure 2.6: Python's development environment used (Spyder 3.3.6)

Despite the zero precedent experience that the author had before starting this project, Python language was chosen due to the advantages that open source coding languages (specially Python) offer. Community and open source development leads to extensive support libraries access, such as Numpy (used for numerical calculations) or Pandas (data analysis and dataframes/matrices structuring). It is a high-level and object-oriented language that allows easy "date and time" structured data handling. Hence, there is an increasing trend in the industry towards its use.

One such open source library, pvlib python, was used extensively and was extremely helpful in the development of the project. *pvlib python* module provides a set of functions for simulating PV energy systems performance. It implements many of the methods developed at Sandia National Laboratories [21][22]. Some of the functions used in this study are described in this chapter.

2.3 Results analysis - Statistical error indicators

In this section, the statistical error indicators used to compare the results are described. Four indicators were used in this project: mean square error (MSE), root mean square error (RMSE), mean absolute percentage error (MAPE) and mean bias

error (MBE). Their formulations are listed below, where M_n and C_n stands for measured and calculated data points respectively, and n represents the number of measurements available.

1. MSE:
   The mean square error measures the average of the squares of the errors, thus it can only be positive. The closer to zero the MSE is, the better the model's correlation is. It is calculated as follows:

$$MSE = \frac{1}{n}\sum_{1}^{n}(M_n - C_n)^2 \tag{2.1}$$

   MSE tends to weight towards larger differences and it is not very intuitive since its unit is the square of the measured variable. In this work the MSE is used only for creating the decomposition model.

2. RMSE:
   The root mean square error provides information on the short-term performance of a correlation by comparing term by term the actual measured value and the correlated one. It can only be positive and the smaller the value the better the model's performance. Its formulation can be seen in Equation (2.2).

$$RMSE = \sqrt{\frac{1}{n}\sum_{1}^{n}(M_n - C_n)^2} \tag{2.2}$$

   As it can be seen, it is basically the square root of the MSE. By doing this, the error is obtained in the same units as the measured parameter which gives a better sense of the differences between the measurements and the model. Similar to MSE it also gives more weight to big differences.

3. MAPE:
   The mean absolute percentage error is an indicator of accuracy expressed as a percentage of the measured data. It is calculated as follows:

$$MAPE = \frac{1}{n}\sum_{1}^{n}\left|\frac{M_n - C_n}{M_n}\right| \cdot 100 \tag{2.3}$$

   Despite its very intuitive interpretation, this indicator has some drawbacks. Outliers, especially for small values of the measured data, can cause very large changes in the absolute percentage error. Moreover, registered values equal to zero would create a singularity problem in the form of dividing by zero. Nevertheless in this case, and as will be explained in the following sections, data has been filtered for values greater than zero, which avoided this kind of error.

4. MBE:
   The mean bias error provides information on the long-term performance of the correlation, since positive errors can be canceled by negative ones. MBE represents the systematic error of a model and is given by:

$$MBE = \frac{1}{n}\sum_{1}^{n}(M_n - C_n) \tag{2.4}$$

   It indicates if the correlation tends to underestimate or overestimate the modeled variable. Ideally it should be equal to zero. In this case, negative values indicate overestimation while positive values indicate the opposite.

2.4 Solar irradiance modeling

Solar irradiance data is essential to properly design solar energy installations. In this regard, many mathematical and empirical models have been developed to calculate solar irradiance in planes with different orientations and inclinations. The process to estimate available irradiance on a tilted surface from horizontal irradiance depends on the solar radiation data available to the user. Figure 2.7 synthesizes this process.

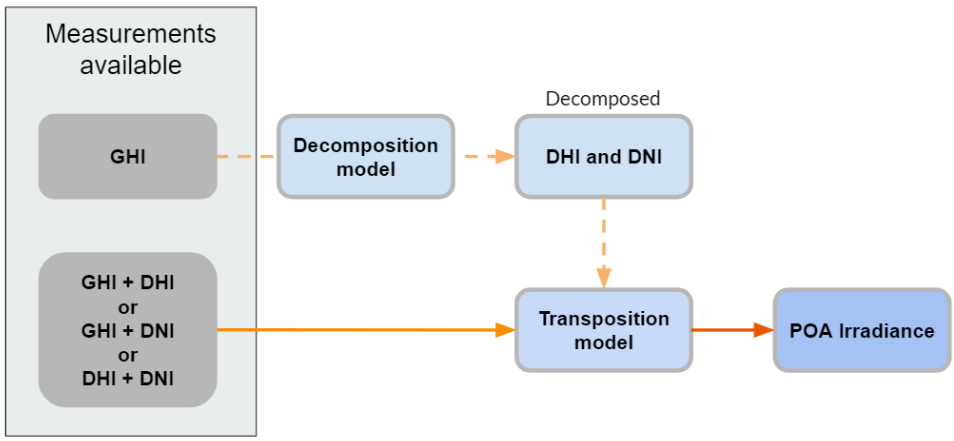

Figure 2.7: Diagram of the process to estimate irradiance on tilted surfaces as a function of the available data

Global horizontal irradiance is the minimum parameter needed as an input to design and develop solar energy projects. If only GHI data is available, decomposition models are used to estimate the diffuse component which is subsequently needed in the transposition models (decomposition models are further explained in Section 2.4.1). Otherwise, if measured diffuse or direct components are also available, the

transposition models can be directly used to estimate global irradiance on the plane of array (POA) (transposition models are further explained in Section 2.4.2).

Global radiation on a horizontal surface is composed of: a direct or beam component (I_b) and a diffuse component (I_d) as it can be seen in Figure 2.8. Beam radiation is the component approaching the device or element in a straight collimated line from the sun, while the diffuse radiation is scattered either by particles in the atmosphere or by clouds, Rayleigh scattering (small particles) or Mie scattering (aerosols or dust)[23]. Ideally, when the sensor has no shadowing elements in its field of view, it receives diffuse radiation distributed throughout the sky dome from all angles from -90°to 90°.

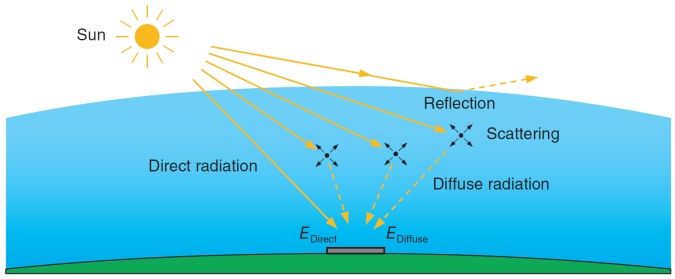

Figure 2.8: Components of the global horizontal irradiance. Source: [23].

2.4.1 Decomposition model creation

Decomposition models are empirical correlations derived from extensive databases of irradiation measurements that are used to estimate the diffuse fraction of the global horizontal irradiation. These spectrally independent methods are also known as diffuse fraction correlations. They basically calculate the diffuse fraction (ratio of the DHI component to the GHI) as a function of different variables such as clearness index, sun elevation angle or other atmospheric parameters.

The most simple models calculate the diffuse fraction only as a function of the clearness index (K_t). The clearness index or clear sky index is defined as the proportion of extraterrestrial irradiance that reaches the earth's surface for the given time and location. Equation 2.5 shows its formulation.

$$K_t = \frac{GHI}{E_0} \tag{2.5}$$

Where E_0 refers to the extraterrestrial irradiance on a horizontal surface.

Extraterrestrial irradiance on a surface normal to the sun (E_{0n}) has to be estimated before derivation of K_t is possible. Afterwards, its fraction onto a horizontal surface (E_0) is weighted by the cosine of the solar zenith angle as shown in Equation (2.7). Extraterrestrial irradiance is not constant, but it can be estimated for every day of the year (n) with the following equation [24]:

$$E_{0n} = 1366.1 \cdot \left(1 + 0.033 \cdot cos\frac{360 \cdot n}{365}\right) \tag{2.6}$$

$$E_0 = E_{0n} \cdot cos(\theta_Z) \tag{2.7}$$

where θ_Z is the zenith angle.

The first term in Equation (2.6) represents the solar constant (i.e. the irradiance on the outer edge of the earth's atmosphere). The introduced value 1366.1 W/m^2 is the default value in the pvlib python module function used in this project (pvlib.irradiance.get_extra_radiation). However, solar constant values ranging from 1360 W/m^2 to 1377 W/m^2 can be found in the literature [25]. Figure 2.9 shows three of the most commonly used decomposition models: Erbs, Orgill & Hollands and Reindl (model 1).

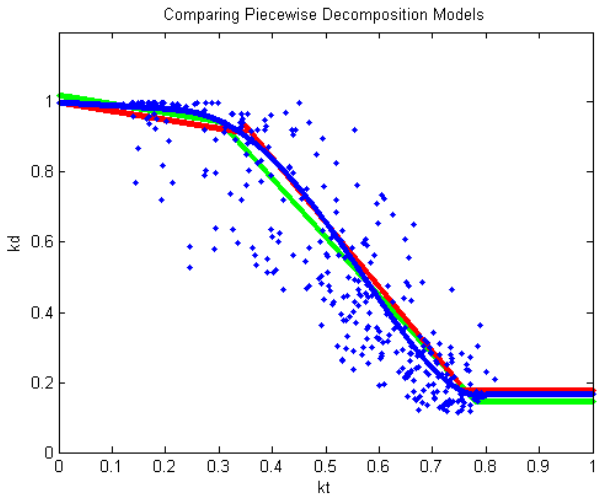

Figure 2.9: Comparison of three piecewise decomposition models. (Blue = Erbs, Red = Orgill and Hollands, and Green= Reindl et al. Model 1). The blue data points are hourly averaged measurements from Florida for September 2013. Source: [26]

Reindl created three different decomposition models: a version only including K_t (shown as case 3 in Figure 2.10) and two others including more variables. Version 2

(shown as case 2) adds solar elevation angle to the equation, while version 3 (shown as case 1) includes also ambient temperature and relative humidity [27]. Those three versions can be seen in Figure 2.10.

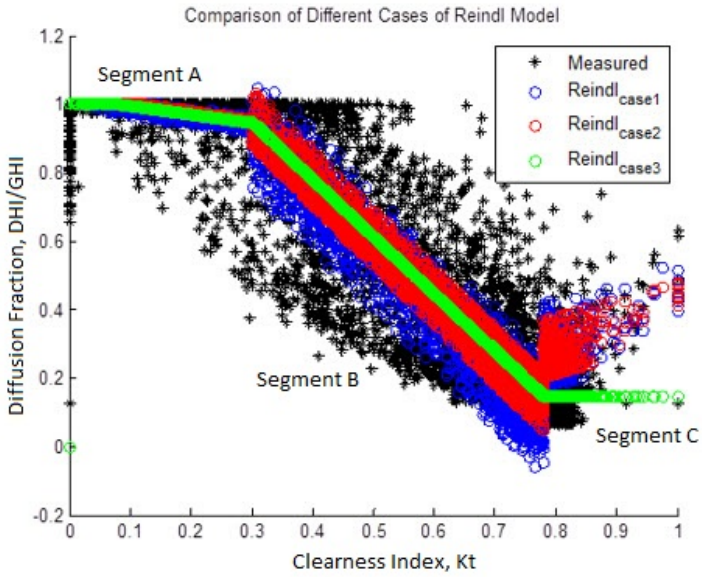

Figure 2.10: Reindl decomposition models compared to measured data. Source: [28]

Reindl realized the drawbacks with diffuse fraction correlations are the high standard error of estimating the diffuse fraction and the accuracy of the correlation being potentially dependent on location. Therefore, in order to identify the best transposition model for vertical surfaces when only GHI data is available, a decomposition model fitted to long term data measured at the Risø test site was created. Even though a correlation model was already created for a nearby location (DTU's Lyngby campus) [29], due to the availability of measured data and differences in irradiance levels according to the DMI (see Figure 2.4), a new decomposition model was created. Its creation process and results are described in Chapter 3.

2.4.2 Optimal transposition model research

Transposition models are tools based on empirical observations and geometric equations that lift horizontal radiation onto a surface with a different inclination.

With regards to tilted surfaces, similarly to the horizontal described above, it receives both direct and diffuse radiation, as well as a portion of the diffuse and beam

radiation which is reflected off the ground and commonly referred as ground reflected irradiance (I_r) as it is shown in Figure 2.11. Therefore, total radiation on a tilted surface (I_{POA}) is composed of three different components: beam, diffuse and ground reflected radiation (Equation (2.8)). The proportion of irradiance reflected depends on two factors: ground properties and surface inclination. The former influences the amount of radiation reflected, while the latter only affects to the ratio of this radiation "seen" by the surface (field of view). For instance, a grass ground surface is assumed to reflect 25% of the incident radiation, while fresh snow can reflect more than 80%. In general, if the ground is unknown values of 20% for albedo can be assumed [30].

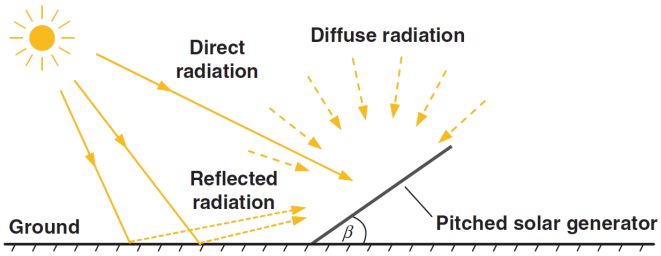

Figure 2.11: Radiation components over a tilted surface. Source: [23]

$$I_{POA} = I_b + I_d + I_r \tag{2.8}$$

On one hand, direct and ground reflected components are a simple matter of geometrical relations. Equations (2.9) and (2.10) show how to calculate beam and ground reflected components respectively. The angle θ refers to the angle of incidence (AOI) and β to the surface inclination of the solar collector. The ground albedo is represented by the Greek letter ρ_g.

$$I_b = DNI \cdot cos(\theta) \tag{2.9}$$

$$I_r = GHI \cdot \rho_g \cdot \left(\frac{(1 - cos\beta)}{2} \right) \tag{2.10}$$

The angle of incidence is the angle between the beam radiation and the normal vector to the solar collector surface. It is calculated as a function of the solar position in the sky dome and the surface inclination as follows:

$$cos(\theta) = cos(\beta) \cdot cos(\theta_Z) + sin(\beta) \cdot sin(\theta_Z) \cdot cos(\gamma_S - \gamma) \tag{2.11}$$

Where γ_S is the solar azimuth angle and γ is the surface azimuth.

On the other hand, the diffuse component is not easily calculated due to the additional sub-components of the diffuse radiation, which include the circumsolar and horizon brightening components. The circumsolar diffuse part is received from forward dispersion of solar radiation and is concentrated in the sky region around the sun. The circumsolar component is brightest under clear sky conditions. The horizon brightening component is concentrated near the horizon and it is most obvious during clear sky conditions.

Transposition models of diffuse radiation use a combination of geometrical and empirical relationships that allow one to calculate the amount of diffuse light impinging on a tilted surface. There are different degrees of complexity from very simple model where diffuse radiation is considered equally distributed over the sky dome (isotropic models) to more complicated ones that assume different diffuse components to account on the different intensity of the diffuse radiation in different regions of the sky (i.e. circumsolar and horizon brightening components). Furthermore, the amount of diffuse radiation in the collector depends on the portion of the sky viewed by the element, as well as other parameters such as: the amount of clouds or water content in the atmosphere.

2.4.3 Analyzed transposition models

There are a lot of transposition models and studies analyzing the benefits of one over the other and yet, none of them is universally know as the best one [31]. Their performance has great influence on the earth location and local weather. For the scope of this project five well-known models have been studied: isotropic, Klucher, Perez, Hay & Davies and Reindl. These models have been chosen for different reasons: there is extensive literature and studies about them and they are implemented in the python library *pvlib*. In fact, many transposition models not studied here, are merely variants with only small modifications to the transposition models studied in this work. The studied transposition models are presented below.

2.4.3.1 Liu & Jordan model

In 1963 Benjamin YH Liu and Richard C. Jordan created an isotropic sky model that described the irradiance on a tilted surface [32]. In their model it is assumed that all diffuse irradiance is uniformly distributed over the sky dome. Therefore, as a matter of fact, diffuse irradiance on the tilted surface was considered only as a function of the field of view. It is the simplest of the presented transposition models and is formulated as follows:

$$I_{d,iso} = DHI \cdot (\frac{(1 + cos\beta)}{2}) \tag{2.12}$$

Liu and Jordan model has proven to have a good performance during cloudy and overcast skies but loses its accuracy as the sky becomes clearer.

2.4.3.2 Klucher model

In 1979, Thomas M. Klucher did a validation on two existing models to predict irradiation on tilted surfaces and in the process created his own model [33]. He compared the performance of the isotropic model above described (Section 2.4.3.1) and the Temps & Coulson anisotropic clear-sky model, by means of comparison to measured irradiance. For the period between January and June 1977, pyranometers on tilted surfaces at 37º and 60º (towards the equator) measured hourly average insolation in Cleveland, Ohio.

The Temps & Coulson model combines the isotropic model with three correction factors that account for the three regions of anisotropy in the radiation field. Klucher didn't take into consideration the factor accounting for surface reflection due to the way the pyranometers were installed (and it won't be considered in this project either since albedo is calculated separately). Temps & Coulson model is described in Equation (2.13).

$$I_{d,T\&C} = DHI \cdot (\frac{(1+cos\beta)}{2})[1+sin^3(\frac{\beta}{2})][1+cos^2(\theta)sin^3(\theta_Z)] \tag{2.13}$$

Where the last two factors shown in brackets account for the horizon brightening and circumsolar components respectively.

Klucher realized that the isotropic model showed a good performance under overcast skies, while Temps & Coulson performed better for clear skies but overestimated irradiation under overcast and cloudy conditions and therefore, he adjusted Term & Coulson's factors with a simple function containing the diffuse fraction. By adding the diffuse fraction (F), the accuracy is improved because the horizon brightening and circumsolar components are reduced as the diffuse fraction increases. The horizon brightening and circumsolar components are both equal to zero during completely overcast days. The Klucher model for irradiance on tilted surfaces can be seen in Equation (2.14).

$$I_{d,Klu} = DHI \cdot (\frac{(1+cos\beta)}{2})[1+Fsin^3(\frac{\beta}{2})][1+Fcos^2(\theta)sin^3(\theta_Z)] \tag{2.14}$$

F represents the function above mentioned and was tested by Klucher as $F = 1 - DHI/GHI$ and $F = 1-(DHI/GHI)^2$. He concluded the quadratic version performs better and therefore, this diffuse fraction will be used. Even though python pvliv description states it uses the linear version, in the source code of its *pvlib.irradiance.klucher* function the quadratic version is used [34]. The needed inputs for this function are: surface tilt and azimuth, DHI, GHI, solar zenith and solar azimuth.

2.4.3.3 Perez model

Richard Perez et al. presented in 1990 two models for daylight availability and one irradiance model [35]. The latter is the newest version of the previously published models that predict diffuse irradiance received on tilted surfaces.

The three models were validated for both hourly and 15-minute data, and parameterize insolation conditions from four basic components derived from the inputs. Only three of them are used in the diffuse irradiance model and are listed below.

1. Solar zenith angle (θ_Z)
2. Sky's clearness (ϵ):

$$\epsilon = \frac{[(DHI + DNI)/DNI] + \kappa(\theta_Z)^3}{1 + \kappa(\theta_Z)^3} \tag{2.15}$$

   Where κ is a constant equal to 1.041 for zenith angle in radians.

3. Sky's brightness (Δ):

$$\Delta = \frac{DHI \cdot AM}{E_{0n}} \tag{2.16}$$

   Where AM is the relative optical airmass and E_{0n} the extraterrestrial irradiance.

This new Perez model is based on the anisotropic diffuse model developed two years earlier by himself and is shown in Equation (2.17).

$$I_{d,Per} = DHI \cdot [(1 - F_1)(\frac{(1 + cos\beta)}{2}) + F_1 \cdot (\frac{a}{b}) + F_2 \cdot sin(\beta)] \tag{2.17}$$

F_1 and F_2 are coefficients expressing the degree of circumsolar and horizon/zenith anisotropy respectively, which are functions of the sky (insolation) condition. The surface tilt is represented by β, and the terms a and b are calculated as follows:

$a = max[0, cos(\theta)]$ and $b = max[0.087, cos(\theta_Z)]$

Where θ is the angle of incidence, i.e. angle between the sun and the normal to the considered surface.

In the same article, a set of recommended coefficients based on data from different locations in the USA and three different cities in Europe is presented. It is argued however, that the choice between which set of coefficients to use is far from critical. The "all-site" set of coefficients achieved an asymptotic level of optimization[35]. Therefore, this set of coefficients has been used for this project. They are summarized in Table 2.2 for different sky clearness bins and Equations (2.18) and (2.19) show how they must be calculated.

Table 2.2: Coefficients for the Perez diffuse irradiance model[35]

ϵ Bin	f11	f12	f13	f21	f22	f33
1	-0.008	0.588	-0.062	-0.060	0.072	-0.022
2	0.130	0.683	-0.151	-0.019	0.066	-0.029
3	0.330	0.487	-0.221	0.055	-0.064	-0.026
4	0.568	0.187	-0.295	0.109	-0.152	-0.014
5	0.875	-0.392	-0.362	0.226	-0.462	0.001
6	1.132	-1.237	-0.412	0.288	-0.823	0.056
7	1.060	-1.600	-0.359	0.264	-1.127	0.131
8	0.678	-0.327	-0.250	0.156	-1.377	0.251

$$F_1 = max[0, (f_{11} + f_{12} \cdot \Delta + f_{13} \cdot \frac{\pi\theta_Z}{180})] \tag{2.18}$$

$$F_2 = (f_{21} + f_{22} \cdot \Delta + f_{23} \cdot \frac{\pi\theta_Z}{180}) \tag{2.19}$$

The Perez model will be implemented in the python code with the build-in function of the pvlib module: *pvlib.irradiance.perez* [36]. This function takes as inputs: surface tilt and azimuth, DHI, DNI, E_{0n}, solar zenith and azimuth, AM and a last parameter where the location-specific coefficient table is chosen. As explained before, the "all-site" table developed in 1990 has been the one used for this project.

2.4.3.4 Hay & Davies model

J. E. Hay and J. A. Davies created an anisotropic model that accounts for both isotropic and circumsolar components of the diffuse irradiance [37]. They realized that the effects of the circumsolar component become more pronounced under clear sky conditions, thus defined an index to weight both components. It is referred as anisotropy index (AI) and it is defined as the ratio between the direct normal irradiance over the extraterrestrial normal irradiance (Equation (2.20)).

$$AI = \frac{DNI}{E_{0n}} \tag{2.20}$$

This index is used to define the portion of diffuse irradiance to be considered circumsolar with the remaining portion being considered as isotropic. Equation (2.21) shows Hay & Davies model.

$$I_{d,HD} = DHI \cdot \left[(1 - AI)\frac{(1 + cos\beta)}{2} + (AI \cdot R_b)\right] \tag{2.21}$$

The geometric factor R_b - as defined by Duffie & Beckman [38] - represents the ratio between the direct radiation on a tilted surface to the direct radiation on a horizontal surface (Equation (2.22)). Since circumsolar radiation is originated in the sky regions around the sun, is projected into the tilted surface in the same way as the beam radiation.

$$R_b = \frac{I_{b,POA}}{DrHI} = \frac{I_b \cdot cos(\theta)}{I_b \cdot cos(\theta_Z)} = \frac{cos(\theta)}{cos(\theta_Z)} \tag{2.22}$$

Hay & Davies model has potential weaknesses. It does not include horizon brightening, hence the model can underestimate radiation under certain conditions. For AOI (θ) greater than 90°, the circumsolar radiation is set to zero because the sun is not on the surface's field of view. Additionally, if at the same time the AI is greater than zero, the model will predict lower diffuse values than the isotropic model.

The Hay & Davies model was implemented in python with the its pvlib module function: *pvlib.irradiance.haydavies* [39]. In this case, function's inputs are: surface tilt and azimuth, DHI, DNI, E_{0n}, solar zenith and solar azimuth.

2.4.3.5 Reindl model

Reindl created a model as a modification of Hay & Davies to include the horizon brightening component. Following a similar model creation process as the one used by Klucher (explained in Section 2.4.3.2), Reindl added to the Hay & Davies model the horizon brightening factor developed by Temps & Coulson and a similar modulating factor (f) as the one included in Klucher model. Equation (2.23) shows Reindl's transposition model [27].

$$I_{d,Rei} = DHI \cdot \left[(1 - AI) \cdot \frac{(1 + cos\beta)}{2} \cdot [1 + f \cdot sin^3(\frac{\beta}{2})] + (AI \cdot R_b)\right] \tag{2.23}$$

In other words, Reindl added to H&D model the horizon brightening used by Klucher with a different modulating factor. He defined f as the square root of the ratio between the beam irradiance in a horizontal surface to the global irradiance (Equation (2.24)).

$$f = \sqrt{\frac{DrHI}{GHI}} \tag{2.24}$$

The idea is that, under cloudy skies the modulating factor and AI go to zero and the model reverts to the isotropic model. The model will predict equal or greater

values than the Hay & Davies model, and the aforementioned weaknesses are mitigated by the addition of the horizon brightening term. Nonetheless, on one side, for completely overcast days f will be close to zero, which would mean unnoticeable differences with the Hay & Davies model. While on the other side, for clear days it would be closer to 1, as it will do the anisotropic index (AI) reducing the first term of the product and thus leading to the same situation where no big differences can be seen. The Reindl transposition model was implemented with pvlib's function: *pvlib.irradiance.reindl* [40]. Inputs used for this model are: surface tilt and azimuth, DHI, DNI, GHI, E_{0n}, solar zenith and solar azimuth.

2.5 Energy assessment

The initial idea was to run energy simulations with different inputs, in order to investigate the bias error that BIPV project developers might risk associated to the transposition model choice or whether they used measured data or transposed. Unfortunately, as it is explained in Section 5.2 the chosen software to perform the simulations (PVsyst 6.7.8) did not allow to use measured data in the POA and showed big differences in the comparison of measured irradiance in the POA versus how PVsyst processes this irradiance in the POA. Besides, less than five months of data was available. Therefore, only comparisons between measured and transposed data in vertical surfaces and the measurement's uncertainty were assessed. Chapter 5 details the results.

CHAPTER 3

Decomposition model creation

In this section, the creation process for a decomposition model is detailed. The steps followed were: data acquisition and filtering, analysis of the available data (or pre-creation), curve fitting and model creation, and decomposition model validation.

3.1 Data acquisition and filtering

The DTU campus at Risø contains a range of different sensors deployed to measure fundamental meteorological parameters. For the creation of the decomposition model the focus is set at the two pyranometers used to measure Global Horizontal Irradiance (GHI) and Diffuse Horizontal Irradiance (DHI) at their main weather station on top of Building 130 (see Section 2.1). Data from these pyranometers and other sensors placed at the mentioned weather station has been stored in DTU's SQL database since February 14^{th} 2017 at different time steps, most sensors are sampled every 10 seconds. These measured or derived (calculated from measurements or date and time) parameters include: Direct Normal Irradiance (DNI), solar geometry values and other atmospheric conditions such as temperature, rainfall or relative humidity.

This data has been continuously recorded and stored in DTU's database. All the available data until November 15^{th} 2019 was used for both creating and validating a decomposition model for the studied location and other locations in Denmark with similar irradiances (see Section 2.1.3, Figure 2.4). Data stored during this 33 months period, have resulted in a total of 6,358,792 data points for each of the measured and calculated parameters.

In the first filtering step, the data within this period has been studied in order to find and remove unreliable data. The "quality assurance and performance monitoring log", created by the department employees, gave a hint on which periods of time must be removed or at least checked as is the case of: sensor calibration periods, unexpected performance or failure events. This resulted in the elimination of more than

300,000 timestamp rows containing compromised or unreliable data points (6,030,574 rows left).

Once this corrupted or non-valid data has been removed, a first Quality Control (QC) has been carried out accordingly with the BSRN Global Network recommendations [41]. The Baseline Surface Radiation Network (BSRN) is a project aimed at detecting important changes in the Earth's radiation field at the Earth's surface which may be related to climate changes. It is a project of the Global Energy and Water Cycle Experiment (GEWEX) under the umbrella of the World Climate Research Programme (WCRP).

This QC measure is a three-step process where first any measurements exceeding physical limits are removed. Next, data outside of what it are considered extremely rare limits are removed. Finally, comparisons based on empirical relations between the different measured parameters are used to delete smaller errors which may have escaped the previous filters.

The limits mentioned in the document are set in order to accommodate all latitudes and climate regimes in the BSRN Program, which covers a latitude range from 80ºN to 90ºS. For detailed information about the QC recommendations made by BSRN refer to Appendix A. All the equations listed in the appendix were implemented in the model excluding filtering conditions applied to ground reflected irradiance (albedo) and long wave measurements since these parameters are not currently measured. After these filters were applied to the dataset, the number of usable rows (time stamps) was reduced to 3,827,771.

At this point, and after BSRN guidelines were applied, other assumptions were made to discard more noise or unreliable data. The following list enumerates the condition applied to the dataset. Data matching these criteria are considered reliable and useful.

1. Elevation angle:
    - Greater elevation angles than 3°[1]
2. Negative irradiation values:
    - GHI values greater than 0
    - DHI values greater than 0
    - DNI values greater than 0

[1] After the uncertainty assessment of the GHI measurements (see Appendix B), it was increased to 5°, which proved to reduce maximum uncertainty from 19.3% to 11.8%.

3. Short wave sum:

    - The sum of short wave radiation ($DHI + DNI \cdot cos(\theta_Z)$) deviation from GHI within 5%

Conditions 1 & 2 have been applied to the measured data in order to avoid nighttime periods where only non-valuable irradiance is measured. These filters also account for early morning and late evening periods when the sun is above the horizon, but irradiance can be measured as negative - due to clear sky radiation losses or reflection losses on the pyranometers dome.

Besides, and even though BSRN guidelines already contemplate rules on the ratio of the GHI over the summed short wave radiation, a more strict filter was applied on this empirical relation. Condition 3 was applied to account for the possible uncertainty in the measurements, any data point with a summed short wave radiation (DHI + DrHI) outside the range of a ± 5 % of the GHI has also been discarded.[2]

3.2 Analysis of available data and pre-development of the model

As described in Section 2.4, a decomposition model relates diffuse fraction to other parameters such as clearness index or solar elevation angle. For the scope of the project, the goal is to create a simple decomposition model for hourly averaged data as a function of the clearness index only. Therefore, once the data was filtered, diffuse fraction and clearness index (as described in Section 2.4 - Equations (2.5) to (2.7)) were calculated for each timestamp.

Once these parameters were calculated, the stored data was filtered again. Apart from the BSRN QC procedure and other filtering assumptions explained in Section 3.1, new conditions regarding these two variables (and other parameters calculated in intermediate steps) were applied to the dataset.

4. Diffuse fraction:

    - Within the range from 0 to 1.05

5. Direct normal irradiance:

    - DNI values must be smaller than the extraterrestrial irradiation

[2]Uncertainty evaluation over the measurements of the GHI has been assessed and is further discussed in Appendix B

6. Clearness index:
    - Within the range from 0 to 1.1

It is physically impossible to get greater diffuse fraction values than 1 yet, part of the measured data (less than 1%) showed to be above this value. Filter condition 4 has been applied to remove corrupted data and still leave margin for the inherent uncertainties in the measured data.

Conditions 5 and 6 are applied to remove data outside physical limits. Even though it can seem that the ratio between GHI and extraterrestrial irradiance in a plane normal to the earth surface (where the sensor is installed) can not be greater than one, it can be for short periods with partly cloudy conditions due to reflected radiation off of the clouds [27], this is a phenomenon sometimes referred to as cloud enhancement. That is why the limit of condition 6 has been set at 1.1.

After the filtering process, the total usable data accounts for almost 3,4 million rows with measurement for each parameter. Figure 3.1 plots diffuse fraction as a function of clearness index with the aforementioned filters applied over the 33 month period studied.

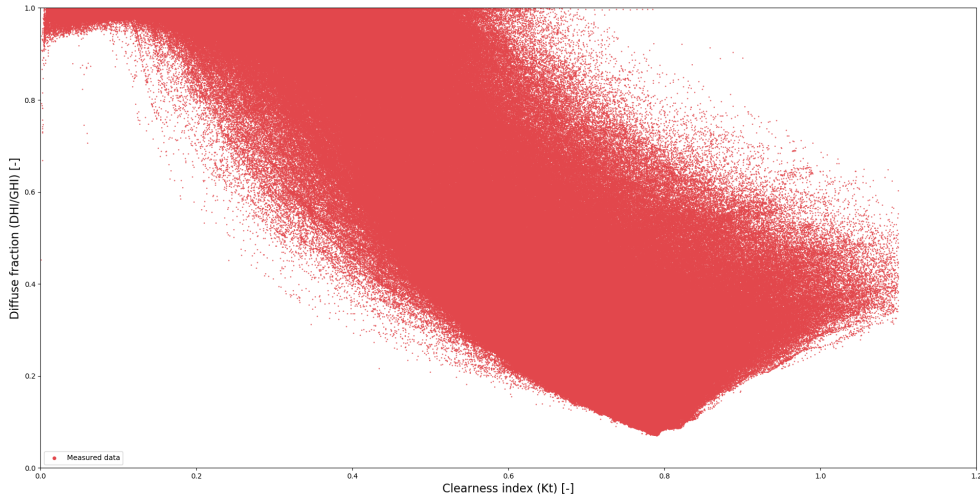

Figure 3.1: Measured data from February 14^{th} 2017 to November 15^{th} 2019 after filters have been applied

As it can be seen, the shape of the represented data differs from the idealized case (as the one shown in Figure 2.9). It is wider in the direction of the x-axis, which is fully related with the measurement frequency. Often, atmospheric variations occur

on short timescales. When the sky is not fully overcast but has some drifting clouds, irradiance values can have big variations in a matter of seconds. Therefore, a 10-second measurement frequency could capture short term atmospheric effects that are not representative of the long-term radiation. By resampling and averaging at smaller frequencies, these 'short-lived' atmospheric events are smoothed out to obtain more relevant irradiance results to the final application of the model. Figure 3.2 shows the effects of resampling the measured data in smaller frequencies. The resampling method used was the average of the measured variables within the resample period. The less frequently the data is sampled, the fewer outliers. The data that is difficult to physically explain, such as the instances with low clearness index and low diffuse fraction or the opposite case, where clearness index is greater than 0.5 and yet diffuse fraction shows big values, are transformed into more reasonable values showing an expected trend as the one mentioned above.

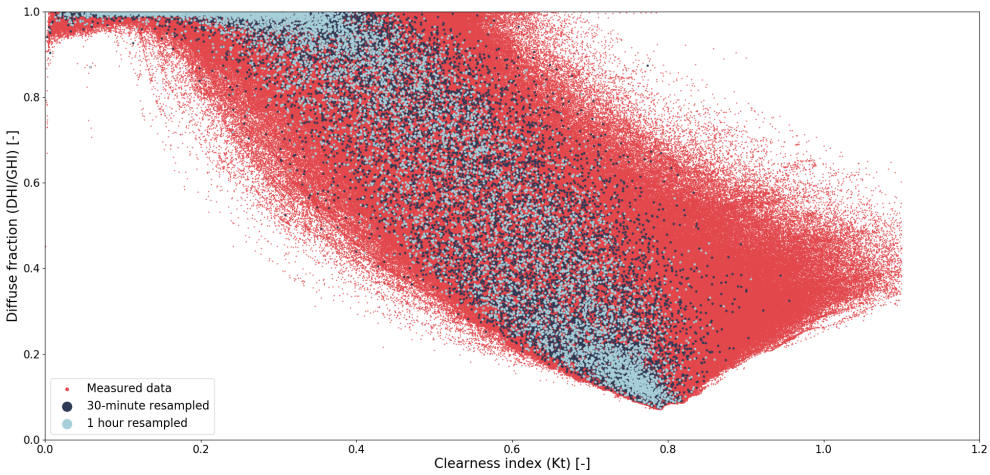

Figure 3.2: Raw data measured every 10 seconds and resampled at different frequencies

Once the data was filtered and the necessary parameters calculated, the dataset was split into two subsets: the first one is used to create a decomposition model (training dataset) and the second subset is used to validate the model (withhold dataset). In the first case, data from February 14^{th} 2017 to August 14^{th} 2018, in which averaging the data on an hourly basis results in 5,950 hours. On the other side, remaining data from August 15^{th} 2018 until November 15^{th} 2019 was used for the second case (validation) and it corresponds to 5,222 rows of hourly averaged data.

In order to transform this "cloud of dots" into a functional curve that can be used to develop the model, diffuse fraction values were averaged for small intervals of clear-

ness index (K_t). Figure 3.3 shows the results of this process. The grey dots show the raw 10-second measured data, while red dots represent the average diffuse fraction for small clearness index binning intervals (in this case 0.001 Kt bins were used). A similar process was followed with the dataset resampled at different frequencies (5 minutes, 30 minutes and 1 hour), and afterwards averaged in a similar manner as the previous case but this time using K_t steps equal to 0.01. The results of these three different resampled datasets are also displayed in Figure 3.3.

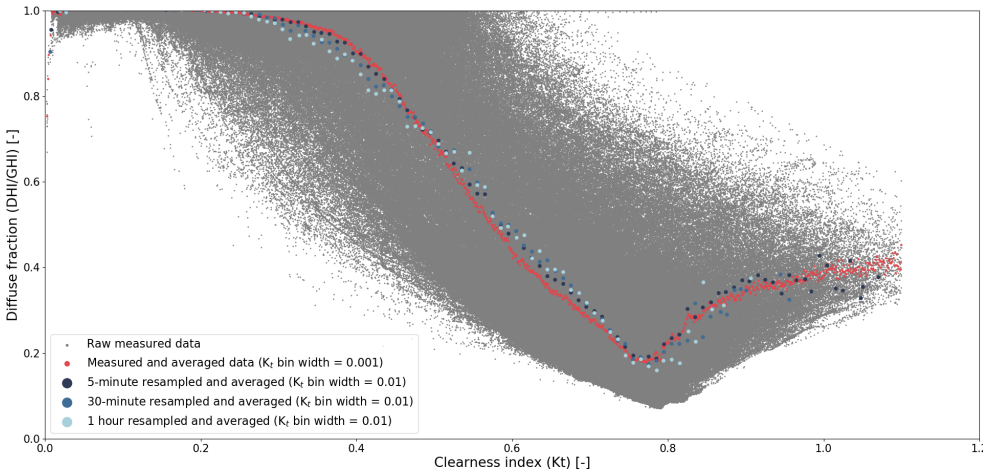

Figure 3.3: Measured and averaged raw data versus averaged data at different resample frequencies

Since the objective is to create a tool accessible for users working in the solar energy field within the Sealand region, the model should be created using sampling frequencies similar to those that will be used in practice (mostly hourly or daily values). In this sense, and with consideration to the above mentioned issues associated with high frequency measurements, and the positive results observed when resampling at smaller frequencies similar to the ones commonly used in the industry of solar energy applications, hourly resampled and averaged data was chosen to create the decomposition model.

3.3 Curve fitting and model creation

At this point, after analyzing and filtering the available data measured at DTU Risø campus, the dataset used for the decomposition model creation is plotted in Figure 3.4 as diffuse fraction versus clearness index.

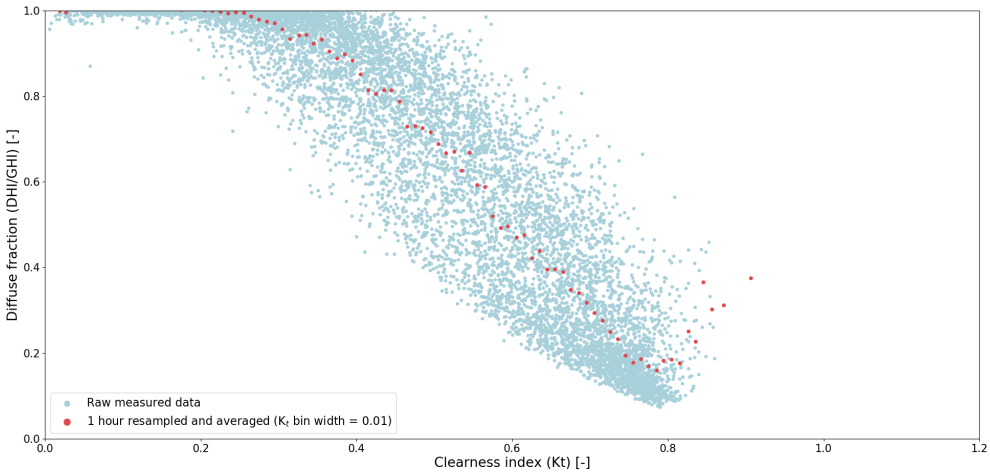

Figure 3.4: Hourly averaged data and weighted curve used to create the decomposition model

As it can be seen in Figure 3.4 and Figure 3.3, the shape of the averaged curves differs from the usual decomposition models explained at Section 2.4.1, mostly in the region with clearness index values greater than 0.8, where other decomposition models consider it as constant. This is due to the fact that diffuse fraction has been modeled only as a function of clearness index when in reality, there are other atmospheric parameters such as relative humidity that contribute to the value of the diffuse ratio. For instance, Douglas T. Reindl developed in 1988 as part of his thesis a decomposition model as a function of: clearness index, solar altitude, ambient temperature, and relative humidity; and a ”reduced” version which considers only the diffuse fraction as a function of clearness index and solar altitude. In fact, Reindl's model shows a similar trend in the region where clearness index is greater than 0.8. He concluded that compared with Lui & Jordan correlation model (which only takes into consideration clearness index), the advance model shows a diffuse fraction reduction in the residual sum of squares by 14%, while the ”reduced” version shows a 9% reduction [27].

Research has been done on what could create this unexpected increase in diffuse fraction for the above mentioned region of the plot (Figures 3.3 and 3.4). As a first step, different parameters were plotted in the clear sky index range from 0.8 to 1.1. This was done to analyze if any particular parameter could explain the behavior in that region (Figure 3.5). Parameters such as solar elevation angle, extraterrestrial irradiance, relative humidity, azimuth or precipitation were investigated.

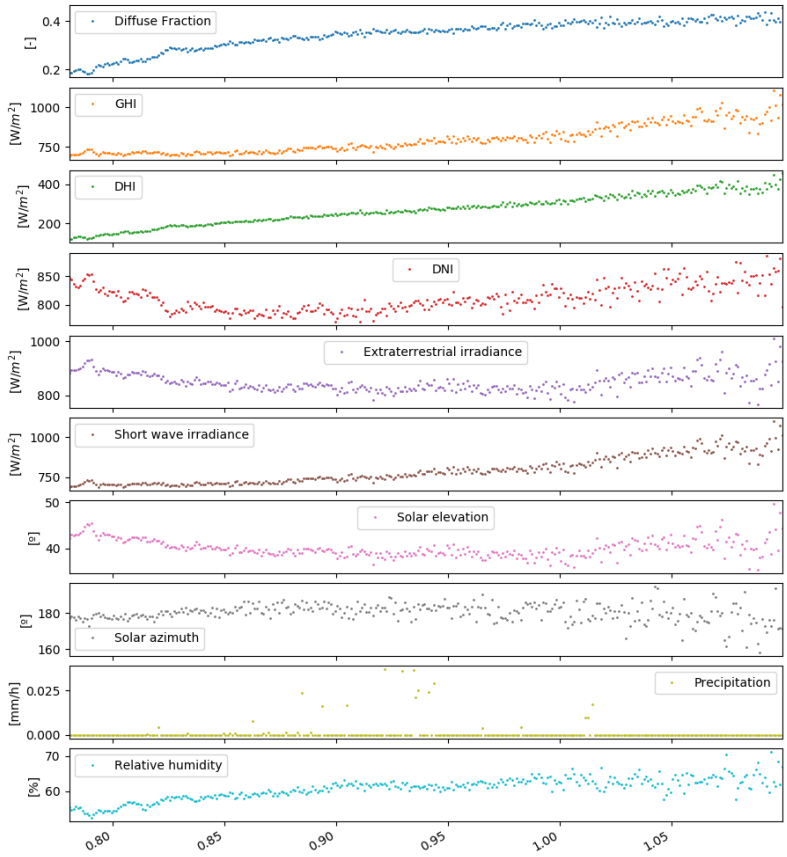

Figure 3.5: Subplot of different parameters behavior for great clearness index values

Apart from the parameters that directly influence diffuse fraction or clear sky index (as GHI, DHI or DNI), it can be seen that relative humidity has a positive correlation within the investigated clear sky index interval.

In order to confirm any possible correlation between the diffuse fraction and other parameters a correlation matrix was calculated with python tools for all the hourly averaged available data. Figure 3.6 shows the results after using the correlation function (.corr()) from python's library pandas. This function calculates Pearson's standard correlation coefficient for linear correlation. Even though it shows the relative humidity has a mid-strong correlation (showing the highest of the non-irradiance related parameters), when it is calculated only for the above mentioned region its correlation is reduced to 0.2. Diffuse fraction, clearness index and relative humidity are also plot with color maps (Figure 3.7) which have not revealed a clear correlation. It was also checked if data measured for large clearness index values are seasonally-dependent

i.e. concentrated in any specific period of time or time of the year, but no further correlations were found.

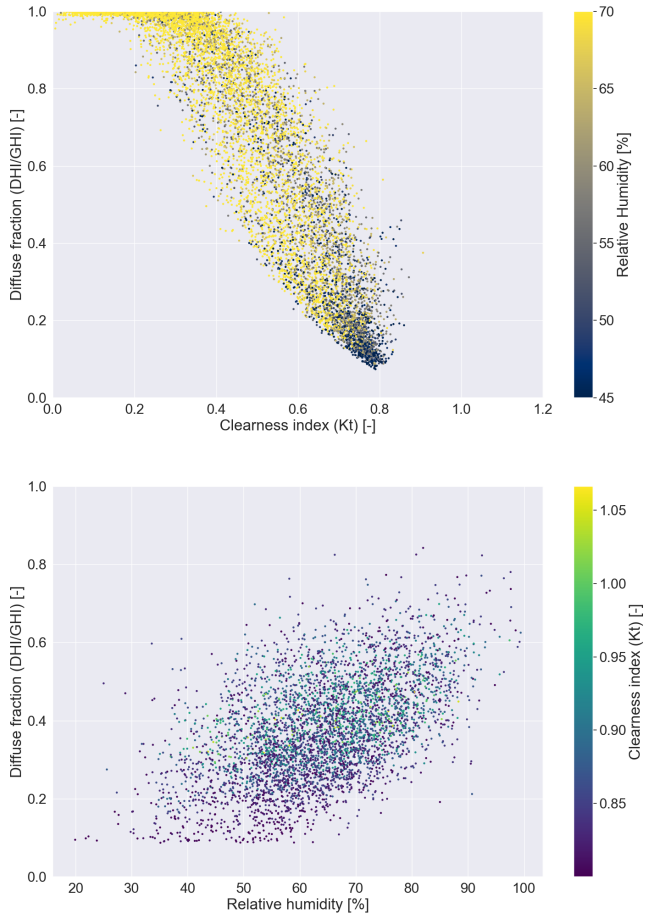

Figure 3.7: Relative humidity relation with diffuse fraction and clearness index

Despite these results, and due to the objective of developing a simple model, any possible correlation with clear sky index (e.g. relative humidity) hasn't been further investigated. End users do not always have access to meteorological parameters other than global horizontal irradiance measurements, and therefore the model has been kept as a simple correlation between diffuse fraction and clearness index. Therefore, data for large values of clear sky index (K_t) have been fitted to a horizontal line. Data in this region only accounts for 1% of the whole dataset, so this assumption won't have great influence on the results. In fact, if one were to dig into the pvlib function

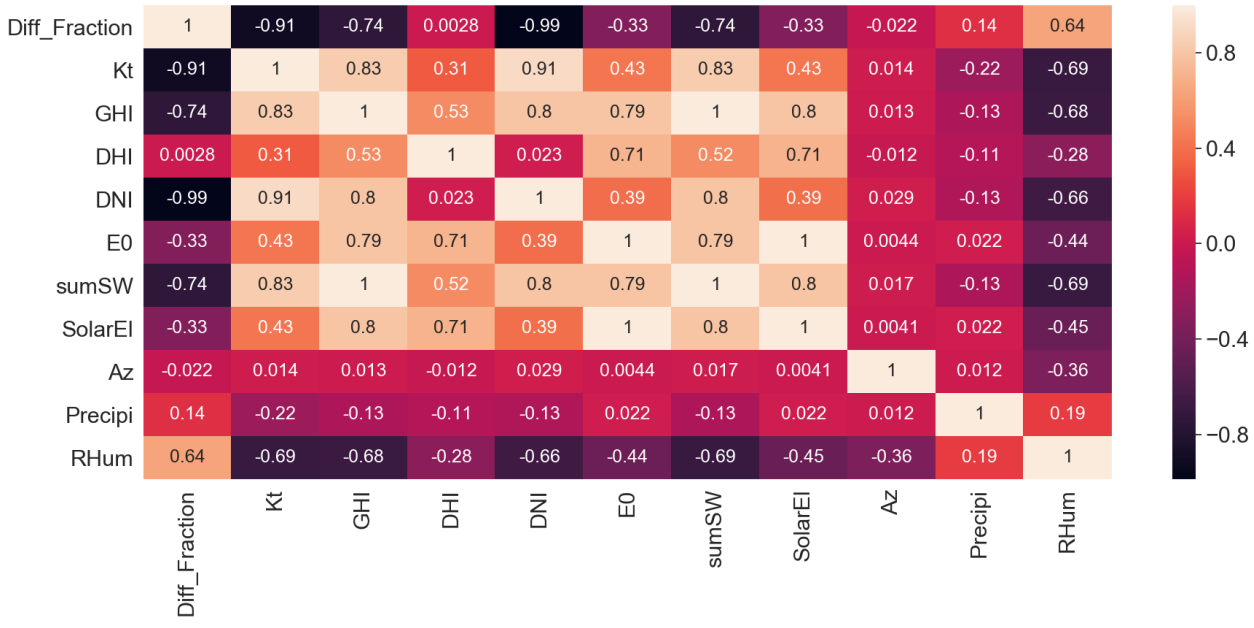

Figure 3.6: Correlation matrix between the diffuse fraction and other parameters

irradiance.clearness_index you would discover that the National Renewable Energy Laboratory (NREL) fortran code and the photovoltaic software widely used by the industry PVsyst, limit the clearness index value for hourly averaged measurements to 0.82 as a default value found in ”preferences”.

At this point fitting the diffuse fraction piecewise to the clearness index is reasonable. Similarly to other decomposition models a three interval piecewise function was created using the dataset shown in Figure 3.4. Piecewise regression functions were used to create a model that fits the hourly averaged data. In order to achieve the best possible fit, regression goodness of fit metrics were used. A function that iterates the borders of the three different regions for different clearness index values in order to minimize the mean square error (MSE) indicator (Equation (2.1)) was implemented in python to find the curve that fits the best the model. The built in function gave as the best model the one shown in Figure 3.8.

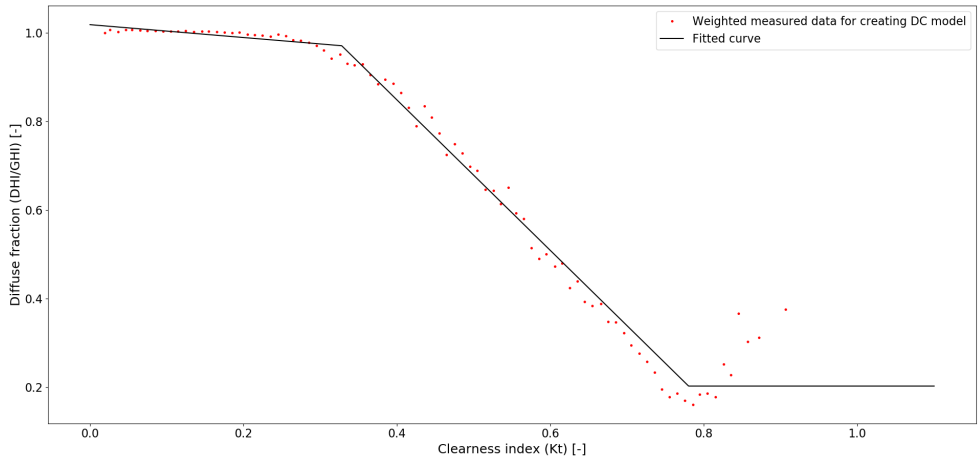

Figure 3.8: Piecewise curve fitting with three different linear functions for the creation of the decomposition model

The final decomposition model created shows a minimum MSE of 0.0015 and can be described as follows:

$$DF(K_t) = \begin{cases} 1.019275 - 0.152132 \cdot Kt & K_t <= 0.331 \\ 1.533974 - 1.707113 \cdot Kt & 0.331 < K_t <= 0.78 \\ 0.20 & 0.78 < K_t <= 1.1 \end{cases} \tag{3.1}$$

3.4 Decomposition model validation

In order to validate the decomposition model, the MSE of the withheld dataset was calculated. Surprisingly, when applied to the hourly averaged dataset from August 15^{th} 2018 until November 15^{th} 2019, this indicator was reduced by half, showing a MSE of 0.0008. Thus it is concluded that the decomposition model is not overfit and is generalizeable to other solar radiation measurements. However, future work should include cross-validating the decomposition model to solar radiation measured elsewhere in the Sealand region. Figure 3.9 displays both datasets over the created decomposition model. In addition, as a double check, the created decomposition model will be tested when comparing transposition models in the following chapter.

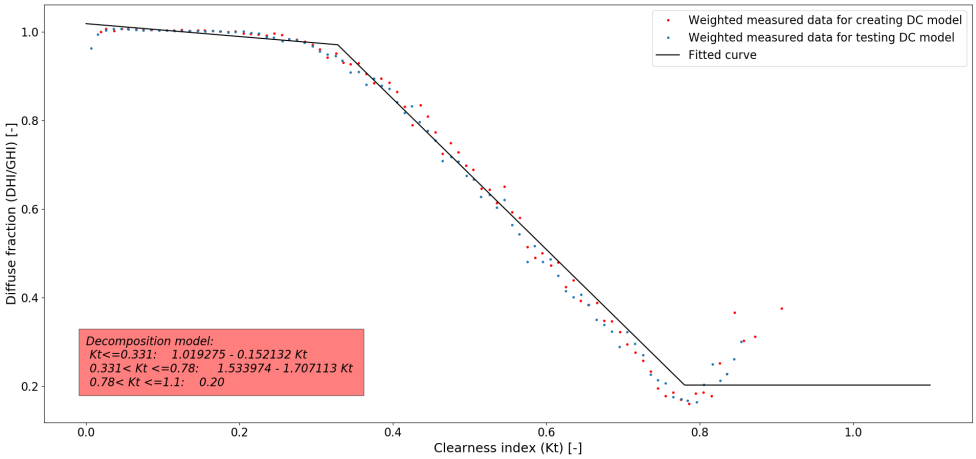

Figure 3.9: Piecewise curve fitting with three different linear functions for both the creation and validation datasets

CHAPTER 4

Transposition models

In this chapter, the description of the analyzed transposition models (described in Section 2.4.2) and the process to identify the optimal model for vertical surfaces in the Northern Sealand region is explained.

4.1 Optimal transposition model research

As a first step to analyze the accuracy of the different transposition models, radiation measured by two tilted pyranometers at the testing field were compared with radiation transposed to the plane of array from the horizontal plane. This constitutes two different scenarios with two different goals. A first scenario where data from a pyranometer installed on a south facing 25°fixed tilt array was compared with the horizontal irradiance data transposed using different transposition models and a second scenario where measured data from a pyranometer mounted on a horizontal single axis tracker (HSAT) was compared to data transposed using different transposition models. Each scenario was analyzed using two different input data sets for the transposition: firstly using all broadband measurements (GHI, DHI, DNI) from the main weather station, and secondly with the same GHI but with DHI and DNI calculated by means of the decomposition model described in Chapter 3. Figure 4.1 shows an aerial view of the testing field. The pyranometer on the fixed tilt array is circled in red and the one installed on the HSAT is circled in blue. Figure 4.2 shows the diagram of this process. In this way, the influence of using measured GHI, DHI and DNI data against the use of a decomposition model fitted for a certain location can be discussed.

The previously explained transposition models were used only to calculate the diffuse component in the plane of array. The beam radiation and ground reflected components in the collector plane of array are calculated using the same approach for all transposition calculations as explained in Equations (2.9) and (2.10).

Figure 4.1: Aerial view of the testing field at Risø

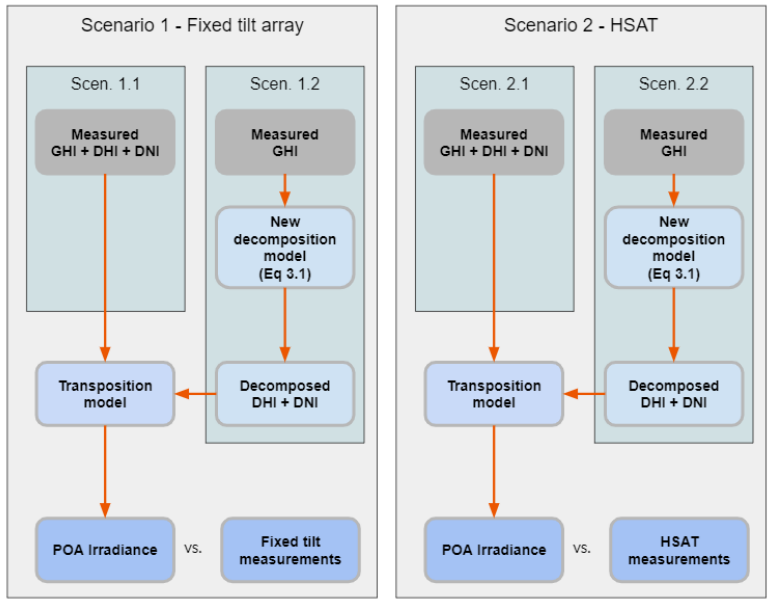

Figure 4.2: Diagram of the process followed to identify the optimal transposition model and validate the decomposition model

4.1.1 Scenario 1 - Fixed tilt pyranometer

In a first case, measurements from a pyranometer located at the bottom end of a fixed array (Figure 4.3) - south facing with 25°inclination - are compared with the

transposed irradiance from the horizontal one measured in the main weather station. This comparison is intended to find which transposition models perform better at this location and to have a better understanding of the differences between them.

Figure 4.3: Pyranometer on fixed tilt array.

4.1.1.1 Data acquisition and filtering

In this case, available measurements from the fixed tilt pyranometer start on January 28^{th} 2019 and therefore, comparisons could not been made before that date. The comparison period was from January 28^{th} 2019 to December 3^{rd} 2019. Unfortunately, measurements from the fixed pyranometers are stored in a different database and with different time format than the sensors at the main weather station. On one hand, all timestamps in the main weather station's database are naive, which means they hold no timezone information. While on the other hand, the fixed tilt pyranometers database is timezone aware and changes for Daylight Saving Time (DST) are recorded. This means that, in order to be able to compare both databases, timestamps had to be transformed into the same time format and timezone. It was known that the main weather station database was using constant timezone equal to UTC +1, even though this information is not included in the database. Therefore, python tools were used to adjust both databases to Denmark's time i.e Central European Time (CET) as well as to change for DST.

The same BSRN QC limits and similar filters to the ones explained in Section 3.1 were applied to the measurements of the tilted pyranometer. Table 4.1 sums up

the filtering conditions applied apart from the BSRN ones. The fixed pyranometer measurements were also filtered to account only in positive values of global irradiance in the plane of array (POA).

Table 4.1: Filtering conditions applied to the dataset for scenario 1

Parameter	lower limit	upper limit
Solar elevation angle [°]	16	-
GHI [W/m^2]	0	-
DHI [W/m^2]	0	-
DNI [W/m^2]	0	E_{0N}
Short wave sum [W/m^2]	GHI -5%	GHI +5%
I_{POA}[1] [W/m^2]	0	-
Diffuse fraction (DHI/GHI) [-]	0	1.05
Clearness index (K_t) [-]	0	1.1

[1] Where I_{POA} refers to the irradiance measured by the pyranometer

When analyzing possible shadowing it was discovered that, due to the distribution of the arrays in the field, the sensor gets shadowing from the previous array for profile angles lower than 16°. Therefore, all the data collected when the sensor was shaded was removed. Unfortunately, at this latitude, sun angles do not reach that elevation during most of the winter period which limited the available data until beginning of November only.

Once both datasets were filtered and the timestamp formats were unified, the dataframes were resampled such that only hourly timestamps remained. Afterwards, a new dataframe was created that joined rows with a common timestamp from both datasets. The purpose was to have a fair comparison between both databases since they might have different maintenance or calibration periods, then in this way those won't be considered. Table 4.2 shows the available data after each of those steps. After the filtering, averaging and cross matching process, a total of 2,828 hours were available for the comparison within the nearly 11 month period studied here.

Table 4.2: Available data rows for scenario 1 after each of the data processing steps

Dataset	Initial	Filtering	Resampling	Final
Main weather station data	2,489,831	151,166	2,877	-
Pyranometer measurements (gantner)	182,963	124,894	5,878	-
Scenario 1.1	-	-	-	**2,827**
Scenario 1.2	-	-	-	**2,827**

4.1.1.2 Transposition models comparison

After the data was filtered and cross-matched between both databases, the angle of incidence between the sun and the normal to the pyranometer was calculated by means of the pvlib function *pvlib.irradiance.aoi* which calculates AOI as explained in Equation (2.11). Once the AOI was defined, beam radiation and ground reflected radiation were calculated for each timestamp with Equations (2.9) and (2.10) respectively. Furthermore, DHI and DNI for Scenario 1.2 were also calculated with the diffuse correlation model created in Chapter 3

The diffuse component in the plane of array was calculated with the 5 different transposition models previously described and added afterwards to the calculated POA beam and ground reflected radiation. Figure 4.4 shows the measured irradiance by the pyranometer versus the transposed irradiance to that same plane for the 5 different models.

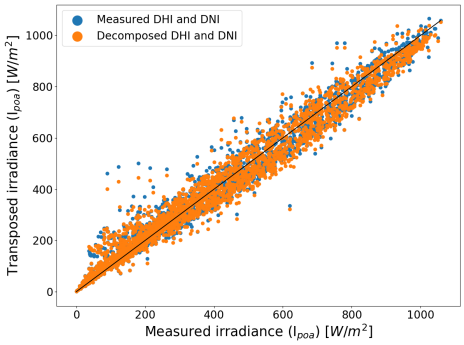

(a) Isotropic (Liu & Jordan) model

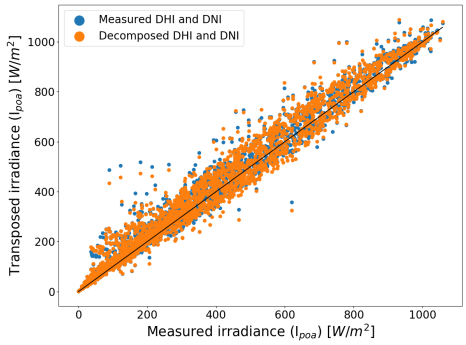

(b) Klucher model

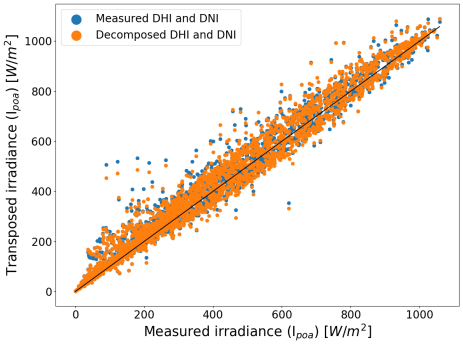

(c) Perez model

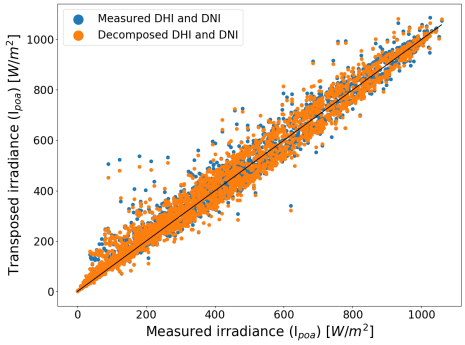

(d) Hay & Davies model

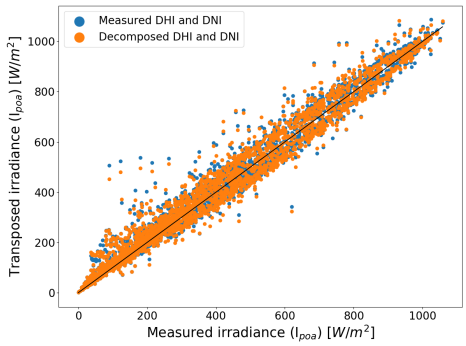

(e) Reindl model

Figure 4.4: Comparison between measured and transposed irradiance on a 25°tilted surface

As it can be seen in Figure 4.4, all of them show a similar shape around the black line, which shows the unity line (what would be a perfect fit). At this point, none of them clearly show better performance over the other. Furthermore, it seems that the choice of using measured DHI and DNI versus decomposed DHI and DNI does not have significant influence on the results.

In order to better quantify the performance of the different transposition models, the "goodness of fit" metrics described in Section 2.3 were used. Root mean square error (RMSE), mean absolute percentage error (MAPE) and mean bias error (MBE) were calculated for each model and both variant of scenario 1. Results are displayed in Figure 4.5. The error bars account for the uncertainty of the GHI sensor. They show how different the statistical results would have been after varying the GHI measurements to their uncertainty limits.

Two straight-forward observations can be seen in Figure 4.5: all different transposition models show similar results (same order of magnitude) and there are no big differences between using measured or decomposed data. Nonetheless, the case where decomposed data was used shows a high variability when uncertainties in the GHI were introduced.

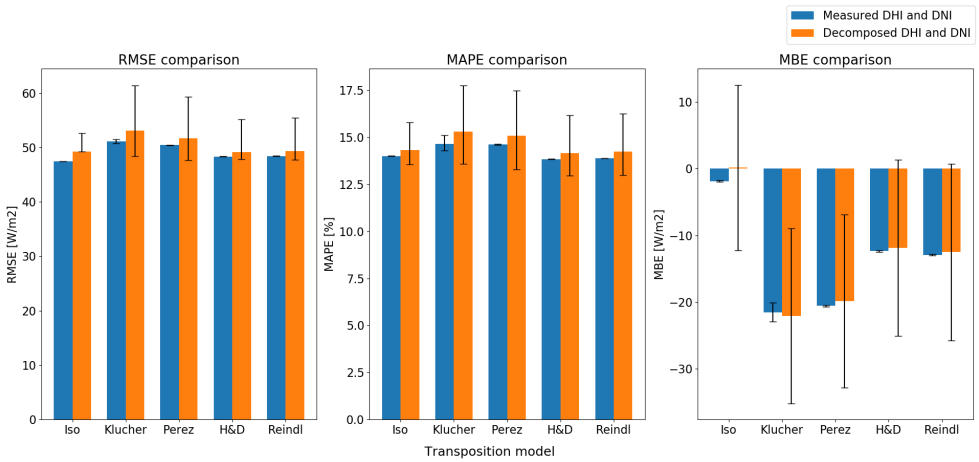

Figure 4.5: Scenario 1 metrics comparison for the different transposition models

Several unexpected results were obtained. The isotropic model (Liu & Jordan), which does not consider circumsolar and horizon brightening diffuse components. Surprisingly, MBE values for the isotropic model show overestimation on average for scenario 1.1 (measured DHI and DNI) and an almost imperceptible underestimation for scenario 1.2 (decomposed DHI and DNI), which is the most surprising result. Moreover, Klucher model is supposed to be an improvement of the isotropic model but shows a worse performance. Namely, the Klucher model introduces two factors to account on the other regions of anisotropy in the diffuse radiation field, what should show an improvement in the performance compared with the isotropic model, but is not the case for the dataset studied here.

Furthermore, Hay & Davies and Reindl models show similar results. The only difference between both models is that Reindl incorporates Temps & Coulson's horizontal brightening factor to the isotropic term in Hay & Davies formula.

In addition, for this specific scenario, since the pyranometer is tilted 25°(β) the sinusoidal term equals to 0.01, meaning the horizontal brightening component won't have much influence in any case.

In order to see if there is any relationship between the sky conditions and the error on the transposition model, daily RMSE was plotted over daily averages of the clearness index. Figure 4.6 shows the results. It can be seen how the error between the measurements and the modeled irradiance increases as the clearness index increases.

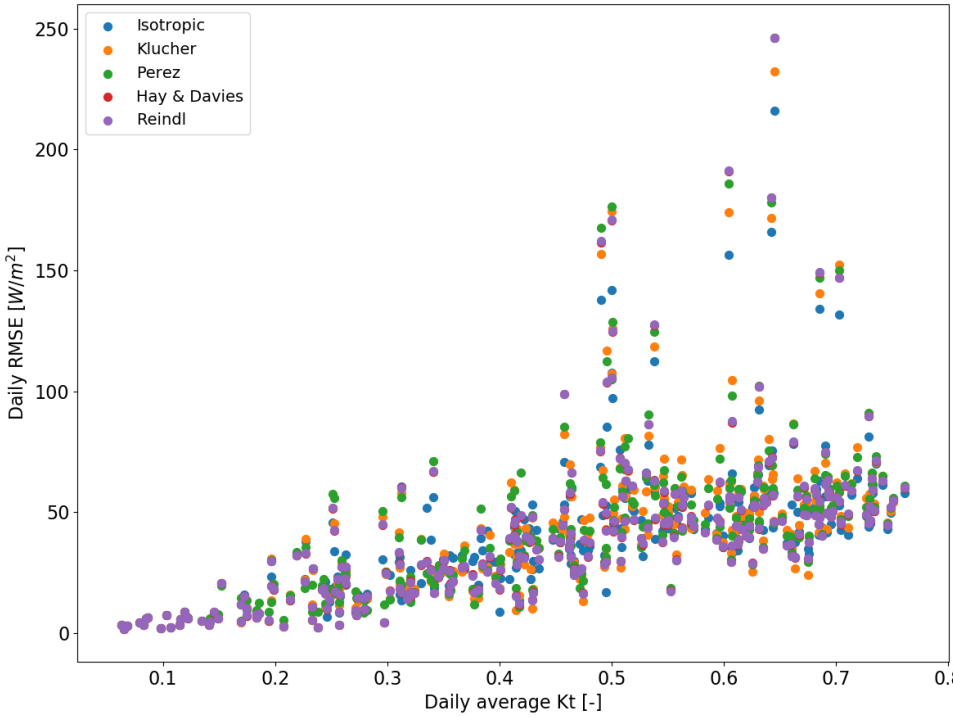

Figure 4.6: Daily RMSE over the daily averages of clearness index for scenario 1 and different transposition models

In view of the results, none of the transposition models can be declared as the best performing nor does any particular model demonstrate clear advantages over the others for the location and scenario studied here. Hence, all of them were considered in the next scenario.

4.1.2 Scenario 2 - Single axis tracker pyranometer

A second scenario was analyzed where measurements from a pyranometer mounted on a horizontal single-axis tracker system were compared with the different transposition models. Figure 4.7 shows the pyranometer experiencing dome frost. Besides, it can also be seen in Figure 4.7 that the back tracking is not optimal, since the last row of the following tracker is shadowed. The tracker axis is mounted on the north-south direction and goes from 60°tilt facing east to the same inclination pointing to the west. In other words, the azimuth angle is 90°before solar noon and 270°after solar noon. It is equipped with a back-tracking system that avoids shadowing between arrays at low elevation angles.

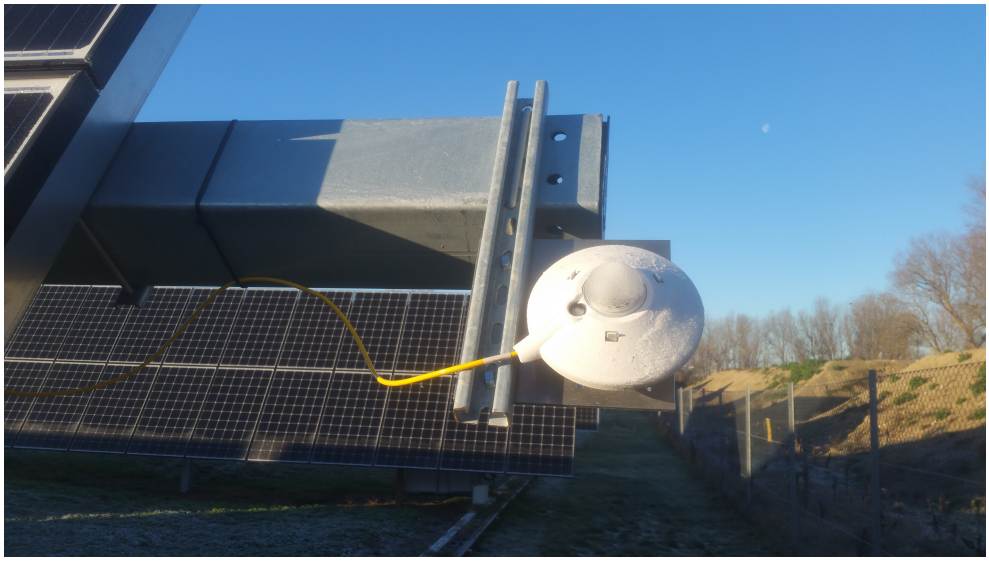

Figure 4.7: Pyranometer on the horizontal single axis tracker system

The main objective of this comparison was to see which transposition models perform better for steep non-south facing surfaces. Therefore, special attention was paid to morning and evening hours when the tracker angle was between 50°and 60°. In addition, it was taken as a double-check test to see if results in scenario 2 support those exposed in scenario 1.

4.1.2.1 Data acquisition and filtering

The same databases as in scenario 1 were used thus, a similar data acquisition and filtering process was followed. Measurements on the pyranometer mounted on the single axis tracker are stored in the "gantner" database (same as the fixed tilt pyranometer), but data on the surface angle is stored in a different one that records all tracker's data. Similarly to Section 4.1.1 the first step was to unify date-time format for the three different datasets used in this case. Both BSRN QC limits and own defined filters were applied to the data. Table 4.3 shows the filter conditions defined for this scenario.

Table 4.3: Filtering conditions applied to the dataset for scenario 2

Parameter	lower limit	upper limit
Solar elevation angle [°]	5	-
GHI [W/m^2]	0	-
DHI [W/m^2]	0	-
DNI [W/m^2]	0	E_{0N}
Short wave sum [W/m^2]	GHI -5%	GHI +5%
I_{POA}[1] [W/m^2]	0	-
Diffuse fraction (DHI/GHI) [-]	0	1.05
Clearness index (K_t) [-]	0	1.1

[1] Where I_{POA} refers to the irradiance measured by the pyranometer

After the acquisition, filtering and resampling steps, all the relevant data was concatenated into two different dataframes (one for each sub-scenario). The pyranometer on the single axis tracker was installed at the same time as the one on the fix tilted array (January 28^{th} 2019). The comparison period was from that date until December the 3^{rd} 2019 (approximately 9 months). Table 4.4 summarizes the number of timestamps available after each of the mentioned steps for the different datasets. The final column shows the number of common timestamps (hours) available for each scenario after cross-matching the three databases indexes.

Table 4.4: Available data rows for scenario 2 after each of the data processing steps

Dataset	Initial	Filtering	Resampling	Final
Main weather station data	2,489,831	208,347	3,860	-
Pyranometer measurements (gantner)	182,963	130,104	5,917	-
Tracker position	429,815	429,634	7,187	-
Scenario 2.1	-	-	-	**3,699**
Scenario 2.2	-	-	-	**3,689**

4.1.2.2 Transposition models comparison

For this scenario, the angle of incidence (AOI) is not a simple mater of the sun position in the sky dome since the pyranometer is constantly moving as well. In the tracker position dataset, only the array's slope is stored. Figure 4.8, shows the slope value throughout one day. It is calculated for each day of the year and it is defined as follows: negative inclination values means that the array is pointing to the east, while for positives values it is pointing towards the west.

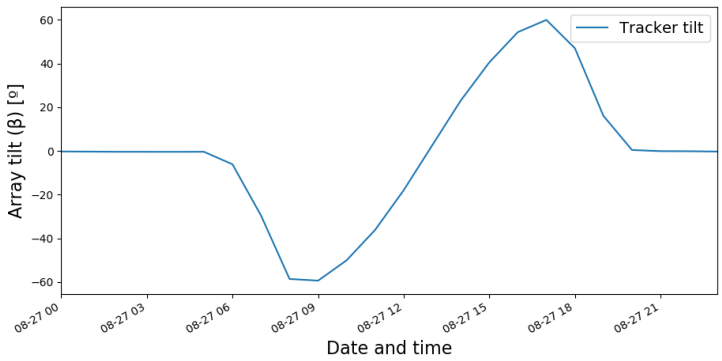

Figure 4.8: Evolution of the single axis tracker inclination throughout a day.

In order to be able to calculate the real AOI and thus, the three irradiance components, stored tilt data had to be redefined as shown in Figure 4.9.

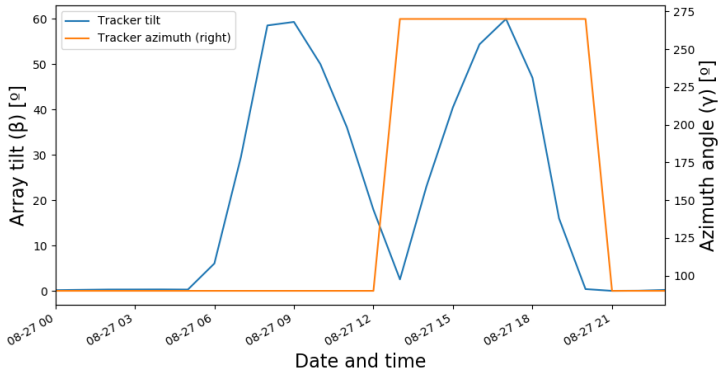

Figure 4.9: Evolution of the single axis tracker inclination throughout a day.

Basically, a new column with azimuth information has been add to the dataframe. It was set to 90°for negative values of the tracker slope and to 270°otherwise. When the tracker is 0°the surface azimuth can technically be any angle because the tracker is horizontal[42]. Afterwards, the tracker slope was changed to its absolute value.

After the surface position was redefined the AOI could be calculated and subsequently, the three irradiance components were calculated in the same manner with scenario 1. Figure 4.10 show the results for each transposition model compared with the measured irradiance in the plane of array.

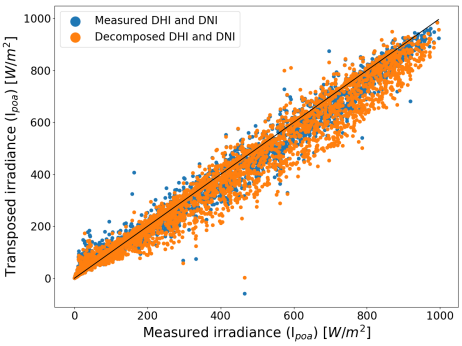

(a) Isotropic (Liu & Jordan) model

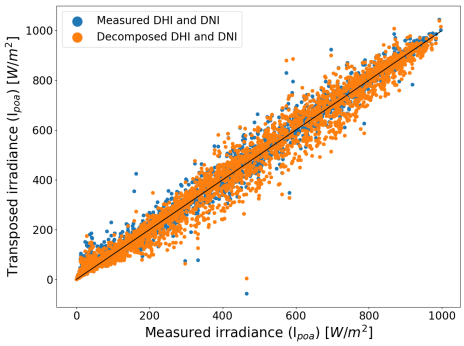

(b) Klucher model

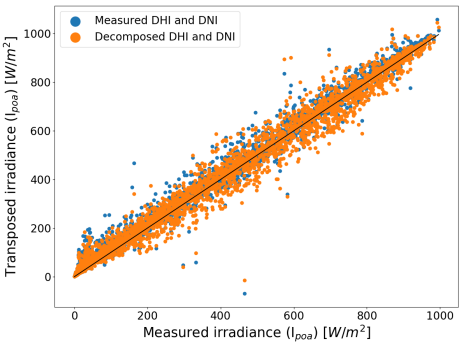

(c) Perez model

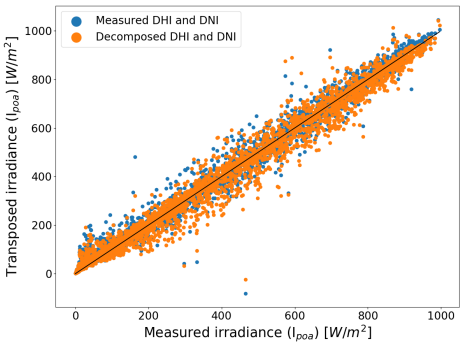

(d) Hay & Davies model

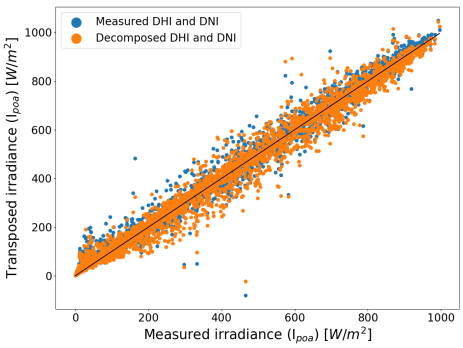

(e) Reindl model

Figure 4.10: Comparison between measured and transposed irradiance on the surface of the single axis tracker

These plots show similar results as the one obtained for scenario 1. Regardless the Isotropic model, which - specially for scenario 2.2 - seems to underestimate measurements more than the previous scenario (its shape looks a bit wider under the black unity line). In order to better analyze the accuracy of the different models, the same statistical error indicators as in scenario 1 are shown in Figure 4.11.

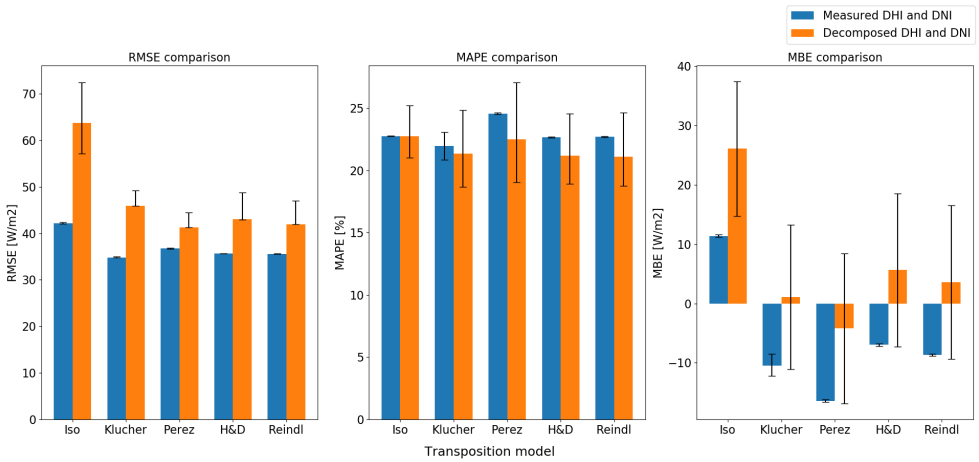

Figure 4.11: Scenario 2 metrics comparison for the different transposition models

As a first observation, it can be seen that the differences in the RMSE between both scenarios (2.1 and 2.2) are greater than in scenario 1. They show differences between 5-11 W/m^2, aside from the isotropic model which RMSE has peaked up to 20 W/m^2, whereas these differences for the fixed tilt comparison were lower than 2 W/m^2. The created decomposition model in Chapter 3 seems to perform a bit worst for non-fixed and non south-facing surfaces.

The anisotropic models show better results in terms of RMSE and MBE. Nevertheless, their MAPE results show an increase close to 10% in comparison to the same errors for scenario 1. As it has been explained in Section 2.3, this indicator is highly influenced by outliers.

One hypothesis was that the pyranometer could have been shadowed in the early morning or early afternoon by the nearby installations e.g. by the fixed tilt rows to the east (see Figure 4.1), or the small hill and trees to the north (see Figure 4.3). If so RMSE and MBE would have not show big increases but such outliers due to shadowing from nearby obstacles could have increased the MAPE values. In order to confirm this theory, measured versus Reindl transposed irradiance was plotted as a function of the azimuth angle. Figure 4.12 shows the results.

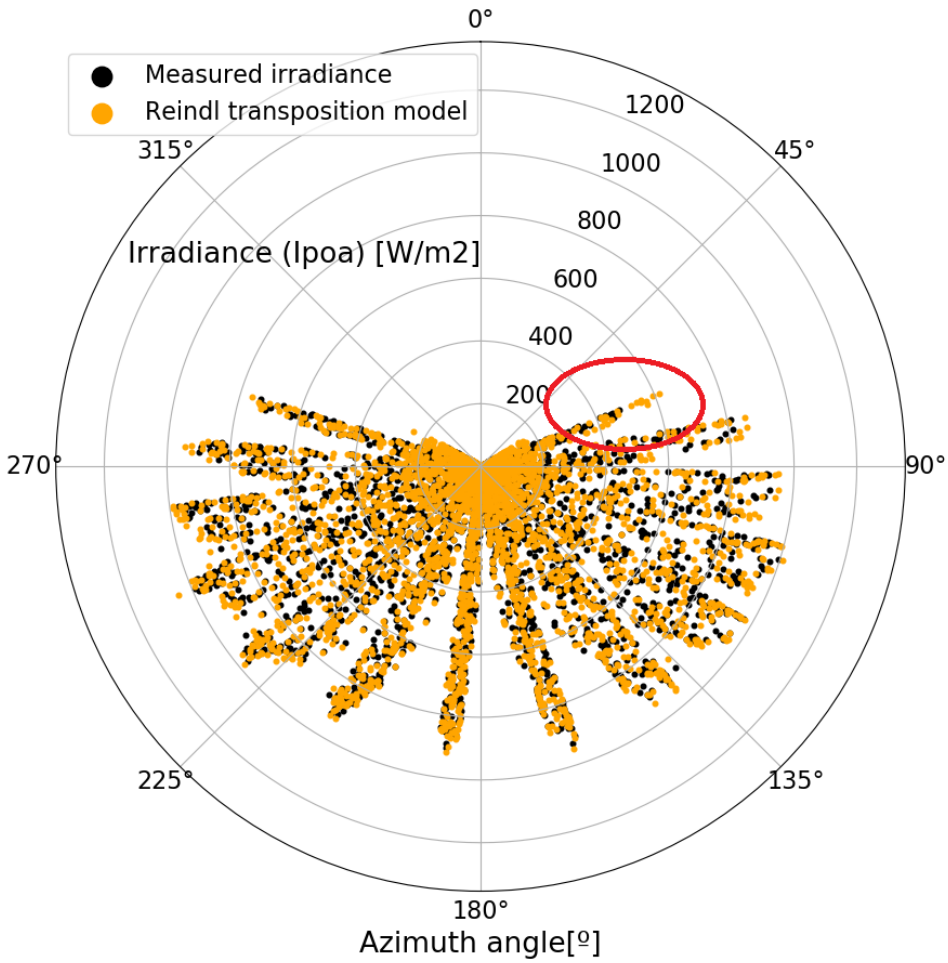

Figure 4.12: Polar plot comparing measured irradiance versus calculated with the Reindl transposition model

As it can be seen, transposed irradiance shows higher values for the solar azimuth regions approximately between 45-75°, during this time the sun is North-East of the pyranometer. In this region of the studied single axis tracker there is a row of threes (see Figure 4.3) which could be creating some shadowing in the morning for those azimuth angles (45-75°). Nonetheless, since the objective of this comparison was to analyze models performance for surfaces close to vertical, this possible shadowing effect was not investigated further and proposed as future work. However, a more

thorough analysis was carried only for tracker tilts between 50-60°, which is the maximum inclination reached fy the tracker surface.

Figure 4.13 shows the statistical error indicators for the comparison only for instances where the inclination of the tracker was between 50-60°.

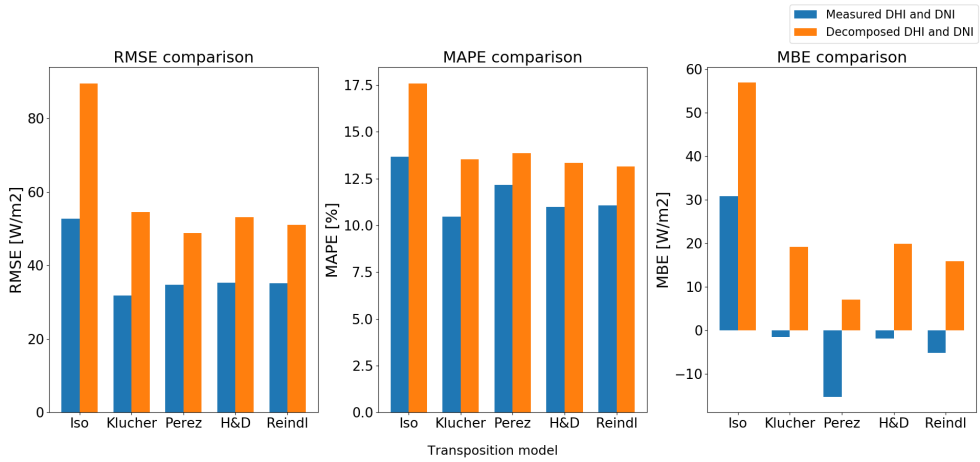

Figure 4.13: Scenario 2 metrics comparison for the different transposition models only for surface inclinations between 50 and 60°

With regard to sloped surfaces with steep inclinations, the differences between scenario 2.1 and 2.2 increased. Even though the MAPE indicator overall has been reduced approximately by half (with the exception of the isotropic model for scenario 2.2), the other indicators have drastically worsened, but only when decomposed data is used. For the anisotropic models, a similar pattern of results was found in the RMSE (which remained almost the same) and MAPE (reduced by half) despite the fact that the MBE indicator varied differently. While Perez MBE remained the same, Reindl was reduced by half and both Klucher and Hay & Davies MBE was reduced to almost zero.

In the view of the results, it is concluded that all the anisotropic transposition models studied have comparable performance. Nevertheless it has been shown that, the use of decomposed DHI and DNI increases model's inaccuracies for steep non south-facing surfaces. Besides, as the surface's slope increases, so too do those inaccuracies introduced by the use of decomposed DHI and DNI data. Therefore, the use of the created decomposition model in Chapter 3 is not recommended for similar installations.

CHAPTER 5

MDPD assessment

After the first investigations on transposition models, results do not show one particular prevailing model over the others. No final conclusions on better performance for this location can be taken. Therefore, all of them were compared to the multi-directional photodiode (MDPD) measurements. In this chapter, results on the novel MDPD sensor tests are presented. Firstly, the MDPD measurements were compared to transposed irradiance to vertical surfaces as a starting point for the second step, an energy yield comparison. A simple BIPV design was created to see the variations in energy production depending on whether measured or transposed data is used. Finally, the MDPD uncertainty was calculated in order to arrive at definitive conclusions.

5.1 MDPD measurements vs transposed irradiance

In order to evaluate what would be the difference or bias error associated with the choice of one transposition model over the others or using measured data by the MDPD, both scenarios were studied. The GHI irradiance measured by a fast silicon photodiode (EKO ML-01) installed in the main weather station will be decomposed and transposed to vertical surfaces (i.e. to the same orientations as the vertical sensors in the MDPD). Then, these results will be compared with actual measured data from the MDPD. It has to be pointed out that the ML-01 PD is an older version of the ML-02 used in the MDPD but they share the same characteristics listed in Table 2.1.

5.1.1 Data acquisition and filtering

The MDPD was installed in September 20^{th} 2019 in the main weather station and its data has been stored in a new database since then. Solar position data was extracted from the main weather database, and GHI measured by a fast silicon sensor (also installed at the main weather station) from another database was used as well. All these data until January 20^{th} 2020 were used for the study.

A similar process to the ones described for the acquisition and filtering steps aforementioned in this document was followed. In the first place, the timestamp format of the different databases was unified. Afterwards, the extraterrestrial irradiance and clearness index were calculated for each timestamp in order to apply the BSRN filters to the measured parameters. The specific filters that were applied in this case are summarized in Table 5.1.

Table 5.1: Filtering conditions applied to the data used for the MDPD assessment

Parameter	lower limit	upper limit
Solar elevation angle [°]	5	-
PD sensor [W/m^2]	0	-
MDPD sensors[1] [W/m^2]	0	-

[1] Represent each of the 6 sensors in the MDPD

At the beginning there were some problems with the set up of the sensor. Extremely high values were registered in the nighttime periods. The code was modified to set irradiance to zero during the night, which was done with an elevation angle constrain. Additionally, in the period between October 2^{nd} 2019 and October 16^{th} 2019, all sensors in the MDPD got frozen at different values (Figure 5.1). The reason for this error was never found but data within this period was removed from the analysis.

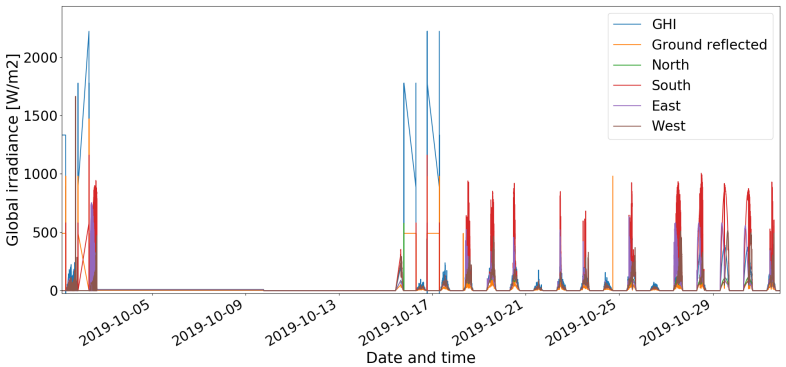

Figure 5.1: MDPD measured data in October 2019

Figure 5.2 shows the evolution in the irradiance measured by the MDPD throughout the day. Four different images are shown in order to appreciate seasonal variations as well as variations due to atmospheric conditions. A sunny day and a cloudy day are shown from September and from January. It can be seen how for overcast days, the four vertical sensors measure similar irradiances. On the contrary, for sunny days,

all sensor measurements throughout the day vary as expected. Nonetheless, it has to be pointed out that the west facing sensor shows peak irradiances much higher than that of the east facing for clear days. Besides, Figure 5.2d shows slightly higher measurements for the west facing sensor.

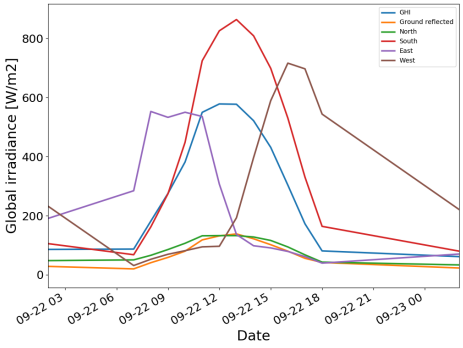

(a) Measured irradiance for a sunny day in September

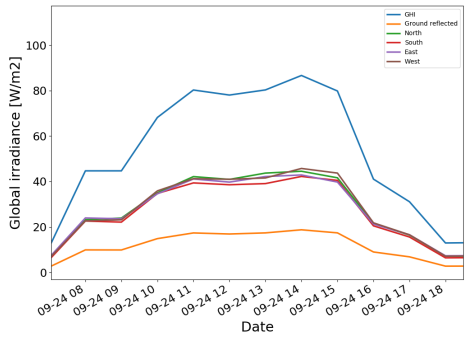

(b) Measured irradiance for a overcast day in September

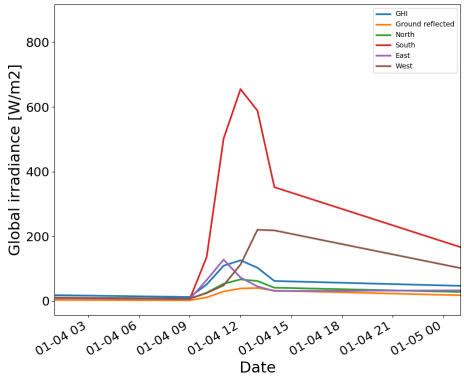

(c) Measured irradiance for a sunny day in January

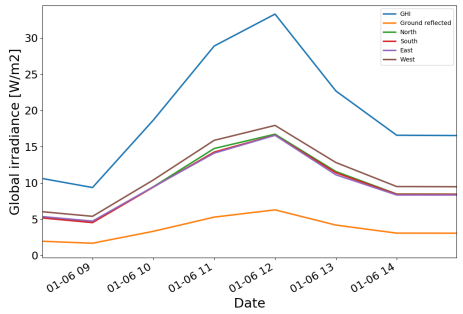

(d) Measured irradiance for a overcast day in January

Figure 5.2: MDPD measurements for different sky conditions and year season

All the data was concatenated into one dataframe and then the filtering steps were applied. Table 5.2 summarizes the number of timestamps available after each of the mentioned steps for the final dataframe and the total available hours for the study within the mentioned period (809 hours).

Table 5.2: Available data rows for scenario 2 after each of the data processing steps

Dataset	Initial	Filtering	Resampling	Final
MDPD comparisons	71,896	39,345	809	**809**

5.1.2 Transposition model comparison

In order to calculate the AOI to each sensor, first the tilt of each of the vertical sensors had to be defined. The MDPD has an inclinometer that stores tilt in two axis: N-S and E-W. These measurements show some fluctuation due to small movements caused by the wind. Figure 5.3 shows the raw inclination data in both axes.

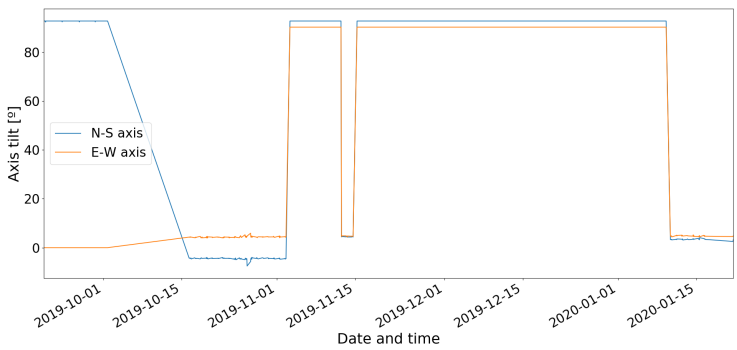

Figure 5.3: Inclinometers raw data for both axis of the MDPD

The MDPD sensor tilt measurements shows frozen values as well. Those points were set to zero first and then, equal to the average tilt measured during "non-frozen" or operational periods. From October 12^{th} a variation of the mean tilt for the N-S axis was introduced in an attempt to better position the sensor. In the absence of the right tools for a perfect fit and knowing that the wind would continue to cause movement, and since $\pm$ 4°was considered acceptable alignment, no further adjustments were made. Finally, the inclination values were averaged for those two periods independently (Figure 5.4).

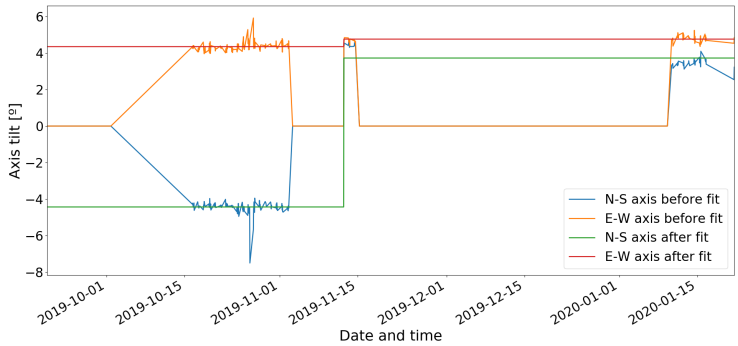

Figure 5.4: Inclinometers data for both axis of the MDPD after adjustments

Each of the four vertical sensors' tilt was adjusted according to the inclinometer measurements. Once, all the vertical sensors surface orientations were defined the AOI, beam and ground reflected irradiances were calculated. A new dataframe for each vertical sensor was created as a copy of the main one and transposed irradiances were calculated for each of them. Figure 5.5 shows the RMSE and MBE calculated for each transposition model grouped by sensors. Additional plots and graphs for each of the sensor can be seen in Appendix C.

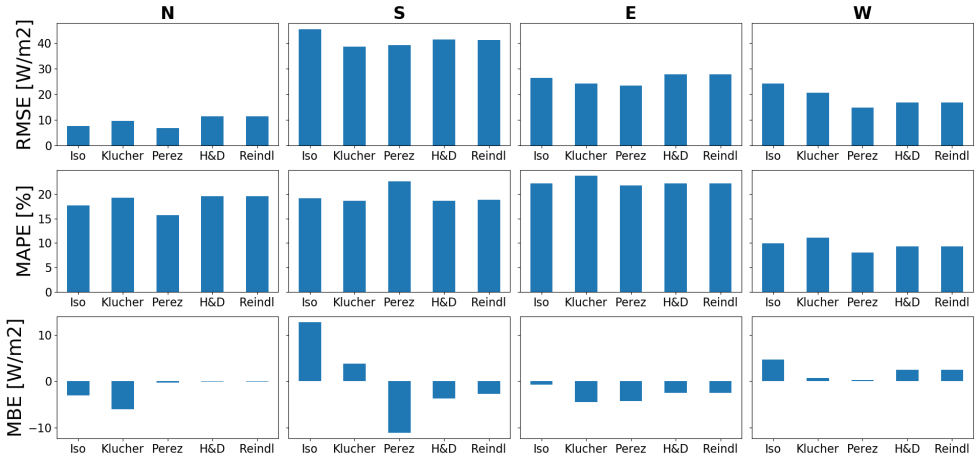

Figure 5.5: Metrics comparison for each transposition model grouped by sensor

Results show, as a general conclusion that, the less time under direct irradiance, the lower irradiances recorded and therefore, the lower errors registered. Based on the RMSE results, it can be seen how the north sensor (only one without direct irradiance during the period studied) shows the lowest error. As the time exposed

to direct beam irradiance increases (higher irradiation measured), so too does the RMSE in approximately the same proportion. The north sensor shows around 10 W/m^2 RMSE, the east and west sensors (which have the sun on their field of view for approximately half a day) show RMSE between 15-25 W/m^2. Finally, the south sensor which is facing the sun the whole day during the period studied shows RMSE around 39-45 W/m^2. Figure C highlights also an unexpected difference between west and east RMSE values. East sensor shows higher RMSE values when both were expected to have similar results. As it has been mentioned above, east and west facing sensors show different peak irradiances under similar conditions (see Figures 5.2a and 5.2c). One hypothesis is that the small deviations from the perfect vertical installation (around 4°on average) might have effects over the measured irradiance.

The same difference between the east and west facing sensors can be seen for the MAPE of the different sensor orientations are compared. All orientations show similar results (around 15-25%) with the exception of the west sensor, which surprisingly shows values around 10%. As previously mentioned, the problem with the MAPE indicator is that big outliers can create high differences, which can be the case here. Figure 5.6 shows a comparison between measured irradiance versus transposed with Perez model for the east and west sensors. In order to make more evident the presence of outliers, only the data points with higher difference between measured and transposed irradiance than the RMSE of each sensor are plotted. It can be seen how, east sensor has a few more outliers. Nonetheless, more than 809 data points during the winter period are needed for more definitive conclusions.

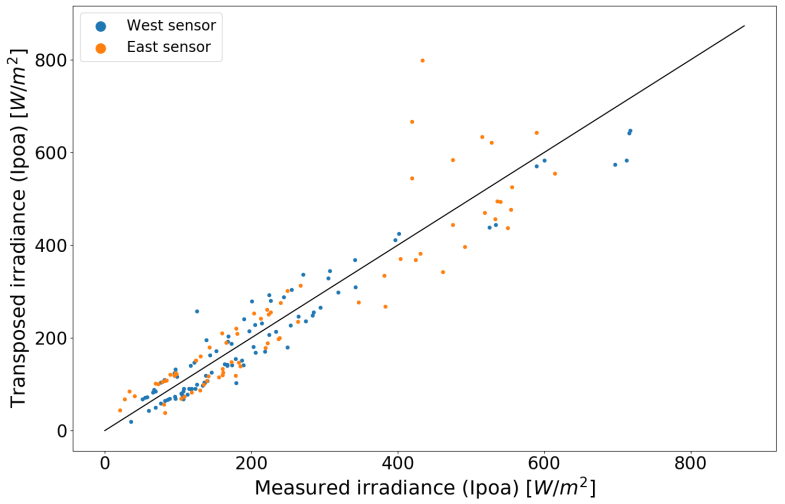

Figure 5.6: Comparison of outliers for east and west facing sensors for the Perez transposition model

The results in this section and in the previous chapter, suggest that Hay & Davies and Reindl models perform equally. RMSE and MAPE results in both scenario 1 and 2 from the previous chapter, as well as both of them in this chapter show exactly the same errors for equal conditions. Regarding the MBE, both models present unnoticeable differences. This result indicates that the horizontal brightening factor that Reindl added to H&D equations has small or no influence in the final result. This could mean that either it must be readjusted for this specific location or horizontal brightening has no influence in the Danish context. Unfortunately, in this case there is only MDPD data available for a few months corresponding to the months of the year with the lowest irradiance values for the studied location and therefore, no final conclusions can be made.

With regard to the north sensor, none of the transposition models consider circumsolar diffuse irradiance. Pvlib functions' code is properly developed to set this component to zero when the sun is not in the field of view of the surface. Nevertheless they differ in the way the other two diffuse components are calculated.

The Perez model uses empirically developed factors chosen from Table 2.2 which influence in the results is difficult to track just by looking at the model. Nevertheless, pvlib function for this model gives the opportunity to get the results separately for the three diffuse components (isotropic, circumsolar and horizon brightening). As expected, circumsolar component is set to zero for all the analyzed hours. Regarding the horizon component, its average value is 1.35 W/m^2 which represents on average the 3% of the total diffuse. This means the horizontal component does not have great influence in the results.

In relation to Klucher model, once the circumsolar component has been set to zero, only the horizon brightening differentiates it from the isotropic model. Results shown by MBE indicate that the Klucher model tends to overestimate irradiance more than isotropic, which results in a higher RMSE. Klucher works better in the other three scenarios. Results show that for surfaces not facing the sun, Klucher does not improve the isotropic model. Nevertheless, the addition of circumsolar and horizontal components together compared with the simple isotropic model improve results for sun-facing or partially sun-facing surfaces.

The MBE indicator results, which show the average deviation in the long-term, are not shown to be greatly influenced by the transposition model chosen for all the sensor orientations (disregarding the south facing sensor). The north and east sensors seem to overestimate solar irradiance on the plane of array by 2 W/m^2 and 2.9 W/m^2 respectively, while the west sensor seems to underestimate solar irradiance by 2 W/m^2. On the other hand, the south facing sensor presents greater differences based on the choice of one transposition model over the other. The Iso and Klucher models underestimate solar irradiance by 12.8 W/m^2 and 3.8 W/m^2 respectively, while the Perez, Hay & Davies and Reindl overestimates it by 11.1 W/m^2 3.7 W/m^2 and 2.7

W/m^2 respectively.

Even though the results show small, long-term variations for each sensor, independent of the transposition model used, further investigations must be made. These should investigate the influence of the RMSE indicator on the final energy production estimation. This RMSE indicator shows the average variation of the transposition model predicted irradiance from each measured value.

5.2 Energy yield

In order to evaluate the difference in energy output by using either transposed data or measured by the MDPD in vertical surfaces PVsyst 6.7.8 software was used. PVsyst is a designing tool for photovoltaic (PV) systems widely used in the industry. Steps followed to reach this goal were: create a simple BIPV system design, irradiance data input and energy output comparison.

A simple square-shaped building with 10kW systems installed in each facade was defined. Figure 5.7 shows the designed building. The black lines define the building facades (all pointing to the 4 different cardinal directions), while the blue lines represent the BIPV system defined in the south facade. Effort was not focused on designing the best possible performing system but just creating a functional one able to serve as a base point for comparison. Therefore, widely used PV panels and inverters were chosen for the simulation.

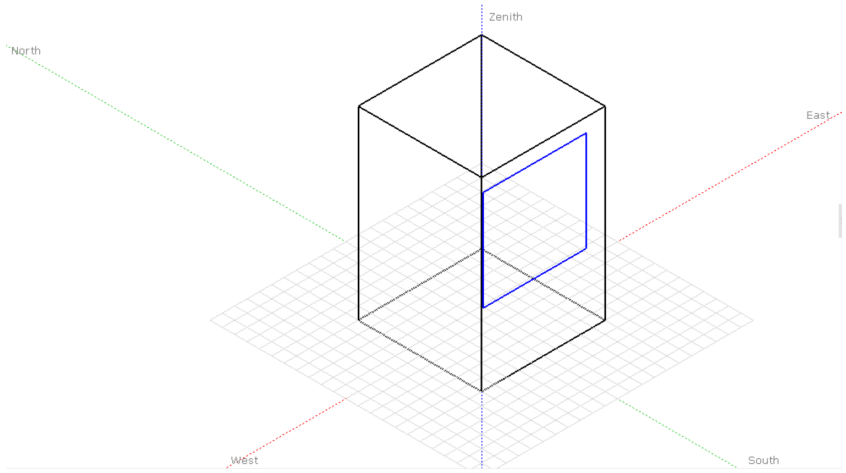

Figure 5.7: BIVP system defined in PVsyst to make energy comparisons

GHI and measured data by each of the vertical sensors of the MDPD were stored in Excel files to be imported in PVsyst. The software has different ways of creating "PVsyst meteo file" and input your own irradiance data, either by using horizontal irradiance (GHI, DHI or DNI) or plane of array irradiance. No problems appeared when importing GHI and running simulations (PVsyst uses Perez or Hay & Davies transposition models). Nevertheless, when plane of array data was imported (MDPD measurements) it was noticed that the software was still using Perez model to transpose data. PVsyst support team was contacted and it was explained the process followed by the software when facing plane of array irradiance. Apparently, PVsyst "retrotansposes" irradiance to a horizontal plane to get all irradiance components and then transposes the irradiance again to the POA. Even though they claim that the possible calculation error associated with this process does not exceed some few per mille, different results were obtained. Measured data by the MDPD sensors was compared to the one retrotansposed and transposed back by PVsyst showing a MBE of -3.15 W/m^2 and a RMSE of 22.40 W/m^2. Figure 5.8 show the difference for each of the hours, reaching mismatches of more than 300 W/m^2 in some occasions.

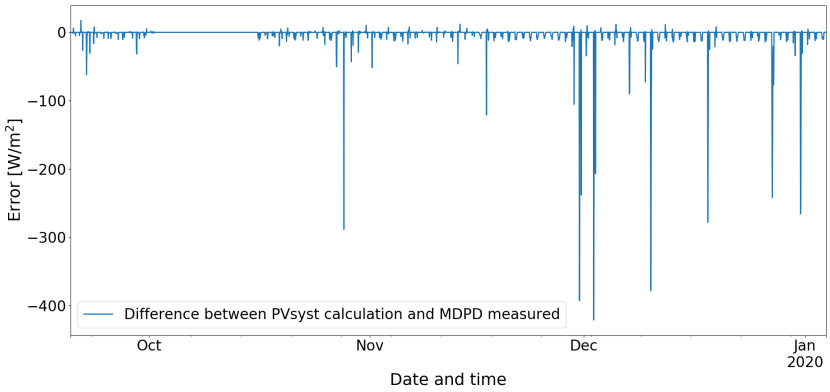

Figure 5.8: Error from Pvsysts "retransposition" method

Even though the MBE is relatively low, as it can be seen in Figure 5.8 hourly differences are noticeable and it would lead to non-comparable results. Therefore, in the view of the results PVsyst was not used to compare energy production predictions.

Other possibilities were investigated such as the System Advisor Model (SAM) developed by the National Renewable Energy Laboratory (NREL) or use of pvlib libraries to design and simulate BIPV systems with python. SAM has already been used to analyze the use of POA measured data [43] validating its use for this type of study. Unfortunately, due to the lack of time, this comparison is proposed as future work.

5.3 MDPD uncertainty assessment

One of the possible advantages of storing irradiance data at different planes is the expected improvement in the measurement's uncertainty. This is due to the additional error introduced by the decomposition-transposition models in addition to the horizontal measurement's uncertainty. This is compared to MDPD sensor where there is only measurement uncertainty as irradiance is already measured in the POA. Uncertainty of irradiance measurements is mostly influenced by the directional response i.e. the inaccuracies associated with oblique sun angles. Therefore, the use of one sensor's measurements over the other at different times of the day is expected to drastically reduce uncertainties according to whichever sensor has the lowest AOI to the sun.

On a similar approach as the one described in Appendix B, the measurement's uncertainties were calculated for each of the MDPD silicon sensors (ML-02) as well as the fast-silicon photodiode used to measured GHI (ML-01). The calculation process is the same for both sensors since they have the same characteristics and is described in Appendix D.

A function was created in python to calculate the uncertainty of each measurement as a function of the sensors' temperature and AOI between the direct irradiance and the sensor. These components change dynamically in the model, while the other sources of uncertainty remain static. MDPD sensor stores the temperature of the printed circuit board inside the sensor, which was assumed to be the same temperature as the sensor. For the ML-01 sensor installed to measure GHI the same temperature has been assumed.

Figure 5.9 shows the probability density distribution of the expanded uncertainties for the six sensors embedded in the MDPD. The python function used calculates Kernel density estimations, which do not represent probability itself but gives a good point for comparison of the uncertainty of one sensor to the others.

As it was expected, the sensors with no direct irradiance (north and ground reflected) present lower average uncertainties as indicated by the peak value of their expanded uncertainty distributions. East and west show almost equal uncertainties. Since they ideally experience same AOI throughout the day with a symmetry around solar noon, these results were to be expected. The GHI and south-facing sensors show similar shapes. For the south sensor, the density distribution is more flat which could be explained by the low sun elevation angles, which result in lower AOIs to the south facing surface within the studied location and time period. Nevertheless, the uncertainties are expected to change in the summer time when elevation angles are higher.

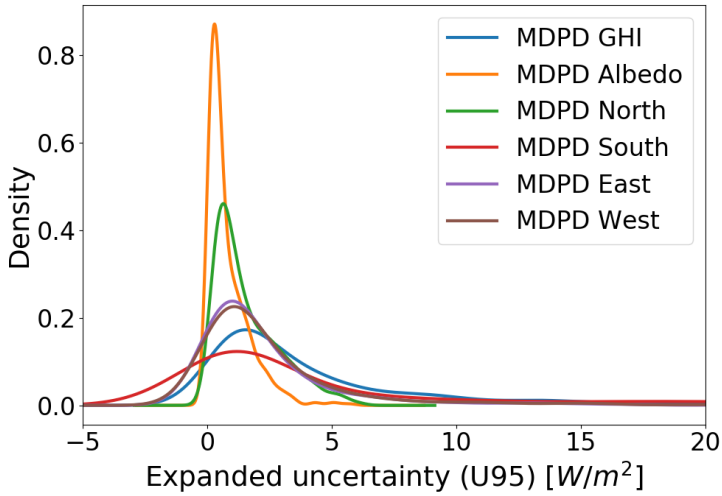

Figure 5.9: Kernel density estimation of the expanded uncertainty for all the MDPD sensors

Figure 5.10 shows the evolution of the expanded uncertainty throughout the day for the six sensor on two different days (September 24^{th} and December 24^{th}). As it can be seen, uncertainty is highly influenced by the angle of incidence.

As it can be seen, due to the influence of the AOI the expanded uncertainty of the sensors varies not only in a seasonal scale but also in a daily and hourly scale. The use of one sensor over the other at different times of the day could decrease the systematic error introduced in the processes used to assess solar resources from POA irradiance that include retrotransposition and transposition of this data. The assessment of the potential advantages of this methodology is proposed as future work.

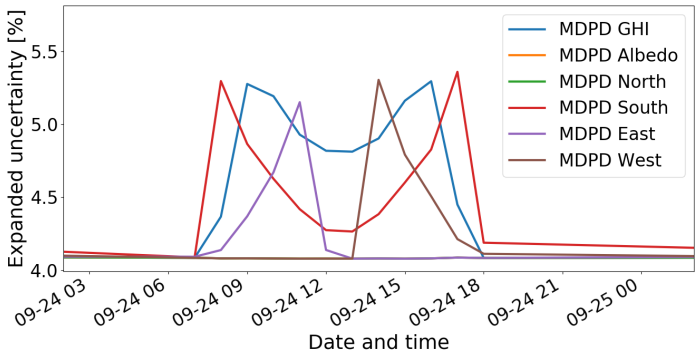

(a) Expanded uncertainty for a sunny day in September

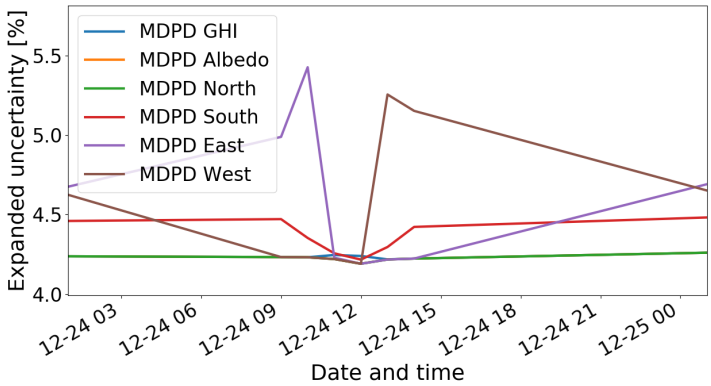

(b) Expanded uncertainty for a sunny day in December

Figure 5.10: Expanded uncertainty of the different MDPD sensors for two different days as function of time of day

In order to have a general view of the uncertainty differences between each vertical sensor and the horizontal one used to transpose horizontal irradiance into their surfaces, histograms of this difference were plotted. Figure 5.11 shows this difference which has been calculated as expanded uncertainty of the vertical sensor minus the expanded uncertainty of the horizontal sensor. Therefore, negative densities represent periods of time with higher uncertainty in the GHI measurement than in the vertical sensor, while positive densities represent the opposite.

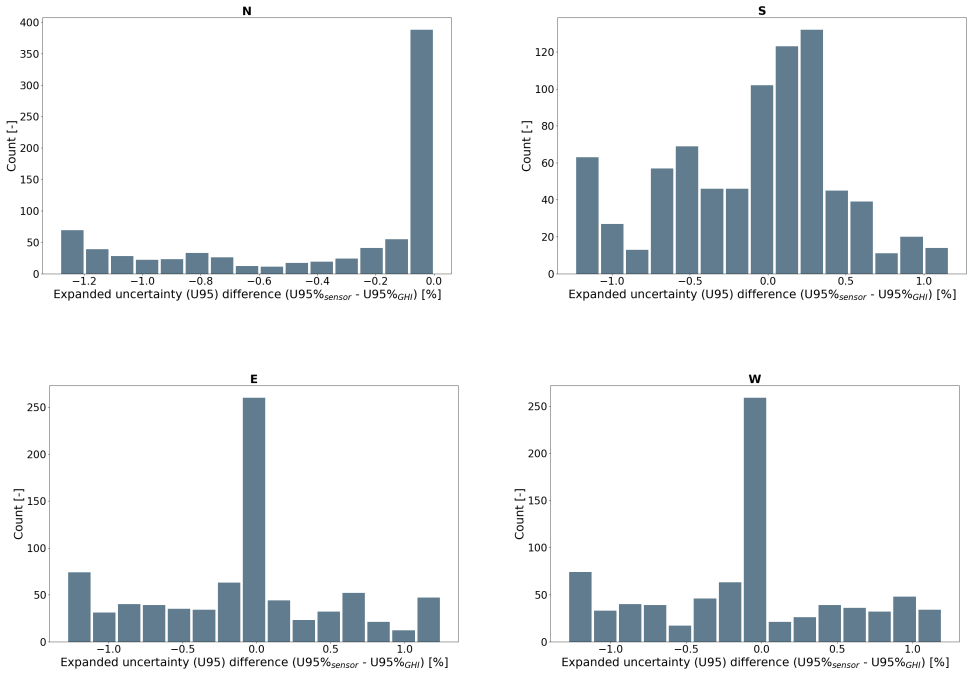

Figure 5.11: Density distributions of the difference between the uncertainty of MDPD vertical sensors measurements and the GHI measurements uncertainty

As it can be seen, they all show small differences overall. All of them have an evenly distribution showing on average no difference with the exception of the north sensor which only shows greater GHI uncertainties or zero difference between the both of them. The explanation can be seen in Figure 5.10. Even though all sensors register lower uncertainties than the GHI sensor in the summer time, thowards the winter time as maximum solar elevation angles decrease, so too do the uncertainty in the GHI sensor which do not get almost beam radiation.

Therefore, in order to have more definitive conclusions, four different cases were studied for the south sensor. Uncertainty in the measurements were added and subtracted from the GHI measurements and the south-facing sensor measurements respectively. In the first case, uncertainties were added to both sensors' measurements while in the second case both were subtracted. In the other two cases, one sensor's uncertainty was added to its measurements while the other sensor's uncertainty was subtracted to the its measurements. Figure 5.12 shows the maximum variations on the RMSE, MAPE and MBE calculated for the comparison between measured and transposed irradiance into the south sensor.

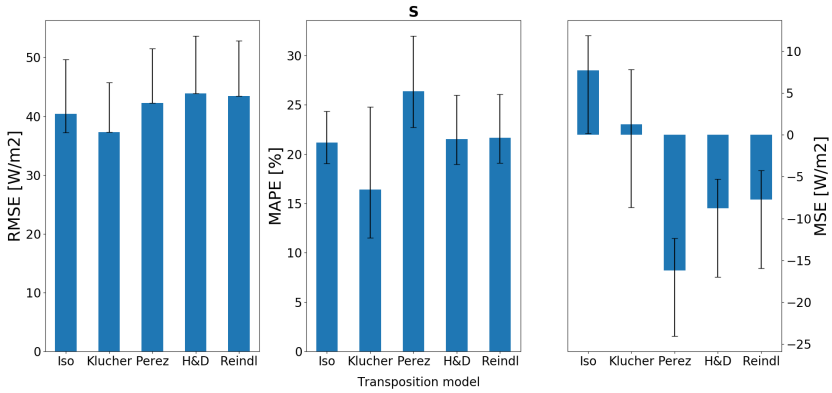

Figure 5.12: Metrics comparison for the south sensor accounting on the GHI PD and the MDPD uncertainties

The error bars show the minimum and maximum errors obtained in the four different cases. Results show that in any of these cases the RMSE of the different anisotropic model is reduced. On the other side, MAPE and MBE show similiar fluctuations for the studied transposition models.

In view of the results, as it has been discuss in Chapter 4, none of the transposition models can be declared as the best performing nor does any particular model demonstrate clear advantages over the others for the location and vertical surfaces studied here. Nonetheless, despite the fact that none energy prediction comparisons were able to be made, these results prove the inherent errors that project developers risk associated to the transposition model choice or whether they used measured data or transposed. It has also been proved the increase in the error by the use of decomposed DHI and DNI over the use of only measured data.

CHAPTER 6

Conclusion

The main objective of the present study was to validate the MDPD sensor manufactured by EKO Instruments and show the benefits of its use for solar PV applications, more specifically for use as vertical solar collectors, such as BIPV or east-west vertical BF plants. In consequence, the advantages of using measured data over the commonly used method to estimated solar irradiance on tilted surfaces were studied. This method involves the use of two mathematical and empirical models to lift horizontal irradiance measurements onto the studied surfaces. In order to carry out this study, the optimal transposition model for vertical surfaces and locations within the Sealand region (Denmark) had to be identified.

To that end, a decomposition model fitted for this region was created. Available measured data at DTU's campus in Risø within a 33 month period for this purpose. The data, measured every 10-seconds was averaged hourly to obtain more relevant irradiance information for the final application of the model. The available measurements were divided into a training dataset to create the decomposition model, and a withhold dataset to validate it.

After creating the decomposition model, available resources at Risø campus were used to conduct two different study cases with the intention of identifying the optimal transposition model among the five studied (Liu & Jordan, Klucher, Perez, Hay & Davies and Reindl). Both study cases were divided into two sub-scenarios depending on the input data: one only used measured GHI, DHI and DNI; the second used measured GHI and decomposed DHI and DNI from the created decomposition model. The purpose of this subdivision was, not only to find the optimal transposition model, but to account for the inaccuracies that the decomposition model might introduce to the process.

The results from the optimal transposition model study led to some interesting results. Regarding the solar resource assessment for south-facing tilted surfaces, none of the studied transposition models were shown to be superior. Furthermore, the results did not show noticeable differences due to the choice of only measured irradiance data over the use of measured and decomposed irradiances. These differences between both sub-scenarios for the RMSE, MAPE and MBE indicators were on average 1.34 W/m^2, 0.45% and 0.62 W/m^2 respectively, validating the use of the created

decomposition model for these surface conditions (25°tilt and south orientation). For the same comparison in the second case (the HSAT comparisons), these "goodness of fit" indicators showed on average differences of 10.19 W/m^2 for the RMSE, -1.17% for the MAPE and 12.66 W/m^2 for the MBE. Furthermore, when the uncertainty of the GHI measurements were included in the analysis, the use of decomposed irradiances could introduce uncertainties within the range of [-1.10, 1.11] W/m^2 for the RMSE, [-3.46, 4.57] % for the MAPE and [-12.95, 12.89] W/m^2 for the MBE. These results highlight the inaccuracies introduced in the solar irradiance assessment for non south-facing and step surfaces, when the use of measured GHI and decomposed DHI and DNI is chosen over the use of only measured irradiances.

With regards to the identification of an optimal transposition model, none of the anisotropic studied models can be declared as the best performing, nor does any particular model demonstrate clear advantages over the others for the location and scenarios studied here. The results relative to scenario 2 when only step inclinations of the HSAT surface were considered (inclinations between 50°and 60°), all anisotropic models underestimate solar irradiance. In this case, the transposition model with the lowest MBE (the Perez model) shows an average underestimation of 7.1 (W/m^2), while the model with the highest results for the same indicator (the Hay & Davies model) underestimates irradiance by 19.9 (W/m^2). Those differences have not been considered sufficient to state a definitive conclusion on an optimal transposition model over the others since they all showed similar RMSE and MAPE results.

After the research on an optimal transposition model for vertical surfaces analysis of the MDPD was carried out. Since non definitive conclusions were made on that matter, the same five transposition models were investigated here. The measurements from the vertical sensors in the MDPD were compared to the transposed irradiance from another PD installed nearby. The results show as a general conclusion that, the less time under direct irradiance, the lower irradiances recorded and therefore, the lower errors registered between each measurement and the predicted irradiance for that instance (RMSE). The RMSE results increases from 10 W/m^2 for the north facing sensor, to 15-25 W/m^2 for the east and west sensors, and around 39-45 W/m^2 for the south facing sensor.

Disregarding the south facing vertical sensor, results show equal performances for all the studied transposition models. They all show RMSE values within a range of approximately 4.5 W/m^2 the north facing sensor. Similar differences were obtained for the other two indicators, within a range of 4.5% for the MAPE and less than 6 W/m^2 for the MBE. The east and west sensor showed similar results. The difference between the different indicators for both sensors are within the ranges of: 4 W/m^2 and 9 W/m^2 for the RMSE, 2% and 3% for the MAPE for east and west sensor respectively, and 4 W/m^2 for the MBE results of both sensors.

The MBE results, which show the average deviation in the long-term, are not

shown to be greatly influenced by the transposition model chosen for all sensor orientations (disregarding the south facing sensor). The north and east sensors overestimate solar irradiance on the plane of array by 2 W/m^2 and 2.9 W/m^2 respectively, while the west sensor underestimates solar irradiance by 2 W/m^2. On the other hand, the south facing sensor presents greater differences based on the choice of transposition model. The isotropic and Klucher models underestimate solar irradiance by 12.8 W/m^2 and 3.8 W/m^2 respectively, while the Perez, Hay & Davies and Reindl overestimate it by 11.1 W/m^2 3.7 W/m^2 and 2.7 W/m^2 respectively.

Even though the results show small variations in the long-term for each sensor, with independence of the transposition model used, further investigation must be made to see the influence of the RMSE on the final energy production estimation. Unfortunately, it was not possible to run energy simulations for a simple BIPV system. Additionally, in this case there is only MDPD data available for a few months corresponding to the winter period and therefore, no final conclusions can be made.

Throughout the project, it has been observed that, both Hay & Davies and Reindl transposition models show negligible differences in their "goodness of fit" indicators results. These unexpected results point out the small (almost nonexistent) influence that the horizon brightening component might have on the diffuse irradiance estimation in the Sealand region (Denmark).

In the final phase of the project, the uncertainty of the MDPD measurements was assessed. As expected, and due to the great influence that the directional response, the uncertainty in the measurements of each sensor show substantial variations not only in a seasonal scale but also in a daily and hourly scale. With the exception of the north facing sensor - which did not receive direct radiation within the studied period, but will in the summer season - and the ground reflectance, which does not receive beam radiation. Therefore, the use of one sensor's measurements over the other at different times of the day is expected to drastically reduce uncertainties according to whichever sensor has the lowest AOI to the sun. This could reduce the systematic error introduced in the assessment of solar resources from POA irradiance, this includes retrotransposition and transposition of this data. The assessment of the potential advantages of this methodology is proposed as future work.

Finally, each of the vertical sensors' uncertainty were compared to the horizontal sensor uncertainty. Even though the expanded uncertainty of all these sensor show hourly variation, those differences on average are around 0.1%. Nonetheless, the process of decomposing GHI data and transpose it to tilted surfaces increased the inaccuracies of the predicted irradiance. These effects combined with the uncertainty of the PD were compared to the uncertainty range of south facing sensor measurements. Results show an increase on the RMSE of 9.22 W/m^2 and variations in the range of [-3.16, 5.21] % for the MAPE and [-8.37, 4.3] W/m^2 for the MBE.

Through this investigation, the inherent errors that project developers of vertical PV systems (such as BIPV or east-west BF plants) should account for in the choice between the use of measured (MDPD) or transposed data (and the associated transposition model choice) has been accurately quantified. For north facing surfaces, the average error of each predicted irradiance value over the measured one (RMSE) can be up to 11.2 W/m^2, overestimating the solar irradiance by 6 W/m^2 should they choose to not use measured data, or the optimal transposition model. In the case of a south-facing surface those errors can be up to 45.5 W/m^2 and 12.8 W/m^2 respectively. The east and west facing surfaces could show RMSE of 26.5 W/m^2 and 24.2 W/m^2, and MBE of -4.5 W/m^2 and 4.6 W/m^2 respectively.

6.1 Future work

A list of possible modifications and improvements to the investigation is presented below:

- An unexpected difference on the peak irradiances measurements and on the "goodness of fit" indicators between east and west sensors was obtained. Therefore, its is recommended to try to adjust the MDPD inclination as close as possible to the horizontal plane to see if this was the cause of such results.

- Additionally, during the course of this project there was only MDPD data available for a few months corresponding to the winter period and energy simulation for a simple BIPV system was not able to be done therefore, no final conclusions can be made. The repetition of the calculations for a full year of data and its use as input for an energy simulation is recommended in order to achieve more definitive conclusions.

- Results show small influence of the horizon brightening component of the diffuse irradiance on this project. Therefore, further research on its influence in the Danish context is suggested.

- Furthermore, the assessment of the potential advantages of the use of one sensor over the other at different times of the day is proposed. It is believed that the systematic error introduced in the processes used to assess solar resources from POA irradiance that include retrotransposition and transposition of this data could be drastically reduced by the by the use of one sensor's measurements over the other at different times of the day according to whichever sensor has the lowest AOI to the sun.

- On a parallel improvement, not related with the purpose of this project, the used pyranometers located at the testing field showed some shadowing issues. Therefore their installed position must be relocated. The pyranometer on the fixed tilt array has already been reinstalled in order to avoid shadowing from the previous array.

In the case of the scenario 2, the pyranometer must be relocated to avoid shadowing from the hill and trees located in its north-west region. Besides, the backtracking system must be readjusted, since it has been seen that shadowing between rows exists.

Bibliography

[1] J. Cook, N. Oreskes, P. T. Doran, W. R. Anderegg, B. Verheggen, E. W. Maibach, J. S. Carlton, S. Lewandowsky, A. G. Skuce, S. A. Green, *et al.*, "Consensus on consensus: A synthesis of consensus estimates on human-caused global warming," *Environmental Research Letters*, volume 11, number 4, page 048 002, 2016.

[2] NASA and S. Callery. (2019). Global climate change: Scientific consensus, [Online]. Available: `https://climate.nasa.gov/scientific-consensus` (visited on 12–2019).

[3] R. K. Pachauri, M. R. Allen, V. R. Barros, J. Broome, W. Cramer, R. Christ, J. A. Church, L. Clarke, Q. Dahe, P. Dasgupta, *et al.*, *Climate change 2014: synthesis report. Contribution of Working Groups I, II and III to the fifth assessment report of the Intergovernmental Panel on Climate Change*. Ipcc, 2014.

[4] D. Wallace-Wells, *The uninhabitable earth: Life after warming*. Tim Duggan Books, 2019.

[5] WMO, "Wmo statement on the state of the global climate in 2018," 2019.

[6] M Allen, P Antwi-Agyei, F Aragon-Durand, M Babiker, P Bertoldi, M Bind, S Brown, M Buckeridge, I Camilloni, A Cartwright, *et al.*, "Technical summary: Global warming of 1.5° c. an ipcc special report on the impacts of global warming of 1.5° c above pre-industrial levels and related global greenhouse gas emission pathways, in the context of strengthening the global response to the threat of climate change, sustainable development, and efforts to eradicate poverty," 2019.

[7] UNEP, "The emissions gap report 2018," United Nations Environment Programme, Nairobi, Tech. Rep., 2018.

[8] IRENA, "Renewable capacity statistics 2019," International Renewable Energy Agency (IRENA), Abu Dhabi, Tech. Rep., 2019.

[9] NREL. (2020). Best research-cell efficiency chart, National Renewable Energy Lab.(NREL), Golden, CO (United States), [Online]. Available: `https://www.nrel.gov/pv/cell-efficiency.html` (visited on 1–2020).

[10] X. Sun, "Global bifacial module market report 2019," Wood Mackenzie, Tech. Rep., 2019.

[11] T. James, A. Goodrich, M. Woodhouse, R. Margolis, and S. Ong, "Building-integrated photovoltaics (bipv) in the residential sector: An analysis of installed rooftop system prices," National Renewable Energy Lab.(NREL), Golden, CO (United States), Tech. Rep., 2011.

[12] L. BESHILAS. (2019). Floating solar photovoltaics could make a big splash in the usa, National Renewable Energy Lab.(NREL), Golden, CO (United States), [Online]. Available: `https://www.nrel.gov/state-local-tribal/blog/posts/floating-solar-photovoltaics-could-make-a-big-splash-in-the-usa.html` (visited on 1–2020).

[13] A. Kreutzmann, "A two-hill island," *Photon*, volume 5-2017, number 1, pages 46–49, 2017.

[14] International Energy Agency. (2019). Renewables 2019, IEA, [Online]. Available: `https://www.iea.org/reports/renewables-2019` (visited on 1–2020).

[15] Y. Xie, M. Sengupta, and M. Dooraghi, "Assessment of uncertainty in the numerical simulation of solar irradiance over inclined pv panels: New algorithms using measurements and modeling tools," *Solar Energy*, volume 165, pages 55–64, 2018.

[16] Y. Xie, M. Sengupta, M. R. Dooraghi, and A. M. Habte, "Reducing pv performance uncertainty by accurately quantifying the pv resource," National Renewable Energy Lab.(NREL), Golden, CO (United States), Tech. Rep., 2019.

[17] EKO Instruments. (2020). Ms-802 pyranometer, sensor information, EKO Instruments, [Online]. Available: `https://eko-eu.com/products/solar-energy/pyranometers/ms-802-pyranometer` (visited on 1–2020).

[18] ——, (2020). Ml-02 si-pyranometer, sensor information, EKO Instruments, [Online]. Available: `https://eko-eu.com/products/solar-energy/si-pyranometers/ml-02-si-pyranometer` (visited on 1–2020).

[19] P. Wang, M Scharling, K. Nielsen, and C Kern-Hansen, *Technical report 13–19: 2001–2010 danish design reference year, climate dataset for technical dimensioning in building, construction and other sectors*, 2010.

[20] Python Core Team, *Python: A dynamic, open source programming language*, Python Software Foundation, 2015. [Online]. Available: `https://www.python.org/`.

[21] J. S. Stein, W. F. Holmgren, J. Forbess, and C. W. Hansen, "Pvlib: Open source photovoltaic performance modeling functions for matlab and python," in *2016 ieee 43rd photovoltaic specialists conference (pvsc)*, IEEE, 2016, pages 3425–3430.

[22] W. Holmgren, C. Hansen, and M. Mikofski, "Pvlib python: A python package for modeling solar energy systems," *Journal of Open Source Software*, volume 3, number 29, page 884, 2018.

[23] K. Mertens, *Photovoltaics: fundamentals, technology, and practice*. John Wiley & Sons, 2018.

[24] J. A. Duffie and W. A. Beckman, *Solar engineering of thermal processes*. Wiley New York, 1991.

[25] C. A. Gueymard, "Smarts code, version 2.9. 5," *USER'S MANUAL For Windows*, 2005.

[26] PV performance modelling collaborative. (2019). Comparison of different decomposition models, PV performance modelling collaborative, [Online]. Available: `https://pvpmc.sandia.gov/modeling-steps/1-weather-design-inputs/irradiance-and-insolation-2/direct-normal-irradiance/piecewise_decomp-models/` (visited on 10–2019).

[27] D. T. Reindl, "Estimating diffuse radiation on horizontal surfaces and total radiation on tilted surfaces," PhD thesis, 1988.

[28] Plant predict. (2019). Reindl's diffuse irradiance model, [Online]. Available: `https://plantpredict.com/algorithm/irradiance-radiation/` (visited on 10–2019).

[29] J. Dragsted and S. Furbo, "Solar radiation and thermal performance of solar collectors for denmark," *DTU Civil Engineering Report R-275*, 2012.

[30] D. G. für Sonnenenergie (DGS), *Planning and installing photovoltaic systems: a guide for installers, architects and engineers*. Routledge, 2013.

[31] A. M. Noorian, I. Moradi, and G. A. Kamali, "Evaluation of 12 models to estimate hourly diffuse irradiation on inclined surfaces," *Renewable energy*, volume 33, number 6, pages 1406–1412, 2008.

[32] B. Y. Liu and R. C. Jordan, "The long-term average performance of flat-plate solar-energy collectors: With design data for the us, its outlying possessions and canada," *Solar energy*, volume 7, number 2, pages 53–74, 1963.

[33] T. M. Klucher, "Evaluation of models to predict insolation on tilted surfaces," *Solar energy*, volume 23, number 2, pages 111–114, 1979.

[34] pvlib-python. (2019). Pvlib klucher transposition model, [Online]. Available: `https://pvlib-python.readthedocs.io/en/stable/generated/pvlib.irradiance.klucher.html` (visited on 10–2019).

[35] R. Perez, P. Ineichen, R. Seals, J. Michalsky, and R. Stewart, "Modeling daylight availability and irradiance components from direct and global irradiance," *Solar energy*, volume 44, number 5, pages 271–289, 1990.

[36] pvlib-python. (2019). Pvlib perez transposition model, [Online]. Available: `https://pvlib-python.readthedocs.io/en/stable/generated/pvlib.irradiance.perez.html` (visited on 10–2019).

[37] J. Hay and J. Davies, "Calculation of the solar radiation incident on an inclined surface. proceedings, first canadian solar radiation data workshop," *Toronto, Ontario, Canada*, 1978.

[38] J. Duffle and W. Beckman, *Solar engineering o] thermal processes, 762pp*, 1980.

[39] pvlib-python. (2019). Pvlib hay & davies transposition model, [Online]. Available: `https://pvlib-python.readthedocs.io/en/stable/generated/pvlib.irradiance.haydavies.html` (visited on 10–2019).

[40] ——, (2019). Pvlib reindl transposition model, [Online]. Available: `https://pvlib-python.readthedocs.io/en/stable/generated/pvlib.irradiance.reindl.html` (visited on 10–2019).

[41] C. N. Long and E. G. Dutton, "Bsrn global network recommended qc tests, v2. x," 2010.

[42] W. F. Marion and A. P. Dobos, "Rotation angle for the optimum tracking of one-axis trackers," National Renewable Energy Lab.(NREL), Golden, CO (United States), Tech. Rep., 2013.

[43] J. Freeman, D. Freestate, W. Hobbs, and C. Riley, "Using measured plane-of-array data directly in photovoltaic modeling: Methodology and validation," in *2016 IEEE 43rd Photovoltaic Specialists Conference (PVSC)*, IEEE, 2016, pages 2653–2656.

[44] J. JCGM *et al.*, "Evaluation of measurement data—guide to the expression of uncertainty in measurement," *Int. Organ. Stand. Geneva ISBN*, volume 50, page 134, 2008.

[45] R Kaarls, "Rapport du groupe de travail sur l'expression des incertitudes au comité international des poids et mesures," *Proc.-Verb. Com. Int. Poids et Mesures*, volume 49, A1–A12, 1981.

[46] I. Reda, "Method to calculate uncertainties in measuring shortwave solar irradiance using thermopile and semiconductor solar radiometers," National Renewable Energy Lab.(NREL), Golden, CO (United States), Tech. Rep., 2011.

[47] J. Konings and A. Habte, "Uncertainty evaluation of measurements with pyranometers and pyrheliometers," National Renewable Energy Lab.(NREL), Golden, CO (United States), Tech. Rep., 2016.

[48] I. O. for Standardization, *Solar Energy-Specification and Classification of Instruments for Measuring Hemispherical Solar and Direct Solar Radiation*. ISO, 1990.

[49] B. N. Taylor and C. E. Kuyatt, "Guidelines for evaluating and expressing the uncertainty of nist measurement results," 1994.

APPENDIX A

BSRN recommendations for QC tests, V2.0

This appendix outlines the recommended filters per the BSRN. For further information about the BSRN guidelines and recommendations refer to BSRN main webpage: https://bsrn.awi.de/.

BSRN Global Network recommended QC tests, V2.0

C. N. Long and E. G. Dutton

Define:

SZA = solar zenith angle

μ_0 = Cos(SZA)

NOTE: In the formulas below, if SZA > 90^O, μ_0 is set to 0.0 in the formula

S_0 = solar constant at mean Earth-Sun distance

AU = Earth – Sun distance in Astronomical Units, 1 AU = mean E-S distance

$S_a = S_0/AU^2$ = solar constant adjusted for Earth – Sun distance

Sum SW = **[**Diffuse SW + (Direct Normal SW) X μ_0**]**

σ = Stephan-Boltzman constant = 5.67×10^{-8} Wm^{-2} K^{-4}

T_a = air temperature in Kelvin [must be in range 170K < T_a < 350K]

Global SWdn: SW measured by unshaded pyranometer

Diffuse SW: SW measured by shaded pyranometer

Direct Normal SW: direct normal component of SW

Direct SW: direct normal SW times the cosine of SZA; **[**(Direct Normal SW) x μ_0**]**

LWdn: downwelling LW measured by a pyrgeometer

LWup: upwelling LW measured by a pyrgeometer

Physically Possible Limits

Global SWdn

Min: -4 Wm^{-2}

Max: $S_a \times 1.5 \times \mu_0^{1.2} + 100$ Wm^{-2}

Diffuse SW

Min: -4 Wm^{-2}

Max: $S_a \times 0.95 \times \mu_0^{1.2} + 50$ Wm^{-2}

Direct Normal SW

Min: -4 Wm^{-2}

Max: S_a

[for Direct SW, Max: $S_a \times \mu_0$]

SWup

Min: -4 Wm^{-2}

Max: $S_a \times 1.2 \times \mu_0^{1.2} + 50$ Wm^{-2}

LWdn

Min: 40 Wm^{-2}

Max: 700 Wm^{-2}

LWup

Min: 40 Wm^{-2}

Max: 900 Wm^{-2}

Extremely Rare Limits

Global SWdn

Min: -2 Wm^{-2}

Max: $S_a \times 1.2 \times \mu_0^{1.2} + 50\ Wm^{-2}$

Diffuse SW

Min: -2 Wm^{-2}

Max: $S_a \times 0.75 \times \mu_0^{1.2} + 30\ Wm^{-2}$

Direct Normal SW

Min: -2 Wm^{-2}

Max: $S_a \times 0.95 \times \mu_0^{0.2} + 10\ Wm^{-2}$

[for Direct SW, Max: $S_a \times 0.95 \times \mu_0^{1.2} + 10\ Wm^{-2}$]

SWup

Min: -2 Wm^{-2}

Max: $S_a \times \mu_0^{1.2} + 50\ Wm^{-2}$

LWdn

Min: 60 Wm^{-2}

Max: 500 Wm^{-2}

LWup

Min: 60 Wm^{-2}

Max: 700 Wm^{-2}

Comparisons

Ratio of Global over Sum SW:
(Global)/(Sum SW) should be within +/- 8% of 1.0 for SZA < 75^{O}, Sum > 50 Wm^{-2}
(Global)/(Sum SW) should be within +/- 15% of 1.0 for 93^{O} > SZA > 75^{O}, Sum > 50 Wm^{-2}
For Sum SW < 50 Wm^{-2}, test not possible

Diffuse Ratio:
(Dif SW)/(Global SW) < 1.05 for SZA < 75^{O}, GSW > 50 Wm^{-2}
(Dif SW)/(Global SW) < 1.10 for 93^{O} > SZA > 75^{O}, GSW > 50 Wm^{-2}
For Global SW < 50 Wm^{-2}, test not possible

Swup comparison
Swup < (Sum SW) [or Global SW if Sum SW missing or "bad"]
For Sum SW [or Global SW] > 50 Wm^{-2}
For Sum SW [or Global SW] < 50 Wm^{-2}, test not possible

LWdn to Air Temperature comparison
$0.4 \times \sigma T_a^4 < LWdn < \sigma T_a^4 + 25$

LWup to Air Temperature comparison
$\sigma(T_a - 15\ K)^4 < LWup < \sigma(T_a + 25\ K)^4$

LWdn to Lwup comparison
LWdn < Lwup + 25 Wm^{-2}
LWdn > Lwup - 300 Wm^{-2}

The limits listed for these tests are set in order to accommodate all latitudes and climate regimes in the BSRN Program. Naturally, these limits could be further refined for specific latitude/climate and achieve better results.

It is recommended that these tests be performed in the order listed above to achieve maximum benefit and minimum impact for "missing" or "bad" cases of some values.

APPENDIX B

Uncertainty calculations I: GHI pyranometer uncertainty in measurement assessment. Process and results.

In this appendix the process followed to calculate the uncertainty in the measurements of the MS-802F pyranometer (SN: F14513FR) is detailed.

B.1 Measurement equation

The above mention thermo-piled based pyranometer uses the following equation to calculate irradiance (I) measurements:

$$I(W/m^2) = \frac{E(\mu V)}{S(\mu V/(W/m^2))} \tag{B.1}$$

Where E represents the output voltage of the thermopile and S the pyranometer sensitivity which is determined by calibration. Both have been considered independent with no correlation since different methods are used to measure or calculate them.

B.2 Standard uncertainties

In the GUM report [44] it is introduced the translation to English of the Recommendation INC-1 (1980) from the original text by the Bureau International des Poids et Mesures (BIPM) [45], which is originally written in French. This recommendation groups the components of the uncertainty into two categories according to the way their numerical value is calculated. A first group (**Category A**) which is evaluated by statistical methods, and characterized by the estimated variances (or standard deviations) and number of degrees of freedom. The second group (**Category B**) is evaluated by other means, and should be characterized by quantities, which may be considered as approximations to the corresponding variances, the existence of which is assumed.

The GUM approach requires stating the type of statistical distribution used for the uncertainty calculations, which is either normal, rectangular or triangular. The NREL summarizes in their report how to calculate the standard uncertainty from the expanded uncertainty for the most common distributions. The above mentioned distributions can be seen in Table B.1. The commonly used terminology is used to calculate uncertainties, where u will represent standard uncertainties, while U is used for extended uncertainties. When extended uncertainty comes accompanied by a subscript, it represents its level of confidence.

Table B.1: Standard uncertainty estimation for common distributions. Source: NREL [46]

Distribution	Source	Standard uncertainty
Normal: Standard deviation = σ number of reading = n or Expanded uncertainty = U and coverage factor = k	Statistical (Type A)	$u = \frac{\sigma}{\sqrt{n}}$ OR $u = \frac{U}{k}$
Rectangular	Non-statistical (Type B)	$u = \frac{U}{\sqrt{3}}$
Triangular	Non-statistical (Type B)	$u = \frac{U}{\sqrt{6}}$
Normal k=2 (or t)	Non-statistical (Type B)	$u = \frac{U}{2}$ OR $u = \frac{U}{t}$

However, irradiance is never constant; the 60 readings within a minute are not truly repeated observations. The variation within the minute can be caused by instrumental variation, but just as well by atmospheric variations on short timescales. Therefore, we argue that the standard deviation associated to the averaging of these values *should not be taken into account when calculating the measurement uncertainty of a pyranometer or pyrheliometer measurement.*[47]

Both parameters introduced in the measurement equation (Equation (B.1)) are considered uncertainty contributors from category B, which means that they are not calculated by statistical means.

1. **Uncertainty in the output voltage (E) measurement**. Campbell Scientific's data logger model CR6 is used for the output voltage measurement, and it's expanded uncertainty calculated for the voltage range used after calibration is equal to 0.08 %.

2. **Uncertainty in the pyranometer's sensitivity (S)**. After the last calibration of the MS-802F, the sensitivity of the pyranometer has been listed as 7.109 ($\mu V/(W/m^2)$).

In the case of the pyranometers's sensitivity, defining it as a function of the zenith angle has proved to reduce the uncertainty in the measurement in 38 % for the same kind of pyranometer and clear-sky conditions[46]. If any of the proposed NREL methods or similar would have been used to fit sensitivity, as a zenith angle function, that fit would have to be treated as type A uncertainty. Nonetheless, it has not been necessary since, for the extend of this project, S have been considered constant.

Yet, and since measurements are not taken in the same conditions that the calibration was performed under, calibration uncertainty is not enough to quantify the pyranometer sensitivity's uncertainty. Other parameters influence in the pyranometer's sensitivity, and therefore, these sources of uncertainties must be also included in

the evaluation of the sensitivity's uncertainty. The most common set of characteristics influencing S uncertainty is listed in the ISO 9060 [48]. In this norm, the pyranometer and pyrheliometer characteristics are defined, as well as the requirements for different classifications. Table B.2 shows the main uncertainty-influencing characteristics of the MS-802F compared with the ISO 9060 secondary-standard requirements (defined as Class A in the newest version - ISO 9060:2018).

Table B.2: EKO MS-802F pyranometer specifications.

Characteristics	**MS-802F**	Secondary-Standard (class A) requirements
Zero Off-set A	**<6** W/m^2	<7 W/m^2
Zero Off-set B	**<2** W/m^2	<2 W/m^2
Long-term Stability	**<0.5 %**	<0.8 %
Non-linearity	**<0.2 %**	<0.5 %
Directional Response	**<10** W/m^2	<10 W/m^2
Spectral Sensitivity	**<1 %**	<3 %
Temperature Response	**<1 %**	<2 %
Tilt Response	**<0.2 %**	<0.5 %

After the uncertainty contributors have been identified, their distribution form and degrees of freedom must be categorized. The following list enumerates and explains how each of these contributors have been considered to influence the measurements uncertainty. For unknown distributions of the expanded uncertainty, it is common to assume rectangular distribution with infinite degrees of freedom [49].

Parameters affecting output voltage (E):

- **Data logger accuracy:** the tolerance stated in the calibration sheet of the CR6, equal to 0.08%, has been assumed to be a symmetric limit specification.

Parameters affecting pyranometer's sensitivity (S):

- **Calibration uncertainty:** last calibration sheet (June 2017) states a sensitivity value of 7.109 $\mu V/(W/m^2)$ with a 95% confidence interval of ± 1.1%. Nevertheless, as a conservative assumption due to the need of re-calibration, it has been doubled to ± 2.2%.
- **Long-term stability:** This value is relevant if the sensor has not been recalibrated recently. Nevertheless, manufacturer specification has been used. The most common source of non-stability in this kind of pyranometers is degradation of the pyranometers black coating that absorbs solar radiation. Even though ISO 9060 lists non-stability as a symmetric source, since this degradation produces a a reduction in sensitivity over time, a one side distribution has been assumed.

- **Non-linearity:** expresses the change in S for irradiance conditions other than the reference ones. The manufacturer's specification has been applied to the full measurement range.

- **Directional response:** is the error caused by assuming the sensitivity to beam radiation is the same regardless its direction. It can be assumed constant and equal to the maximum limit of 10 W/m^2 or, on a similar approach to the one used by Konings et al. [47], calculated as a function of beam radiation and solar zenith angle. For a beam radiation source of 1000 W/m^2 applied normal (θ_Z=0º) to the sensor, the limit of 10 W/m^2 would represent a deviation of 1 % from the real value. Nevertheless, if the same source was applied at bigger angles, and the 10 W/m^2 deviation was constant for all the different incidence angles, the expanded uncertainty for the directional response would vary for instance from 1 % to 2 % for θ_Z=60º, and would be greater than 5 % for θ_Z=80º (Figure B.1). It has therefore been assumed equal to (Lambert's cosine law): $\frac{10}{1000 \cdot cos(\theta_z)}$

- **Temperature response:** specifies the maximum change in S for different temperatures than the reference one (25ºC) within an interval of 50ºC. Manufacturer's specification of 1% has been applied.

- **Tilt response:** Even though the manufacturer has specified it as 0.2 %, it represents the change in S for mounting positions other than reference position (horizontal), and since in this application is horizontally set up, its contribution to the uncertainty assessment is not considered.

- **Maintenance:** ISO 9060 outlines that other effects can be considered. An uncertainty related to maintenance has also be considered. Sensors are cleaned weekly preventing them from fouling, and therefore, an extra expanded uncertainty of only 0.5 % has been included in the calculations.

Parameters affecting irradiance measurement (I):

- **Zero off-set a:** is the response to net thermal radiation. The pyranometer's dome exchanges radiation with the surroundings. This means that the dome may heat up and transfer some extra long-wave radiation to the thermopile, which would increase solar radiation measured. To apply it pyrgeometer data is needed to know the net heat exchange. Since this data was not available during the test period and the manufacture estimates it as just 6 W/m^2 it has been considered negligible.

- **Zero off-set b:** is the response to temperature gradients. The manufacturer has set its value at 2 W/m^2. In order to simplify the calculation, it was also considered negligible.

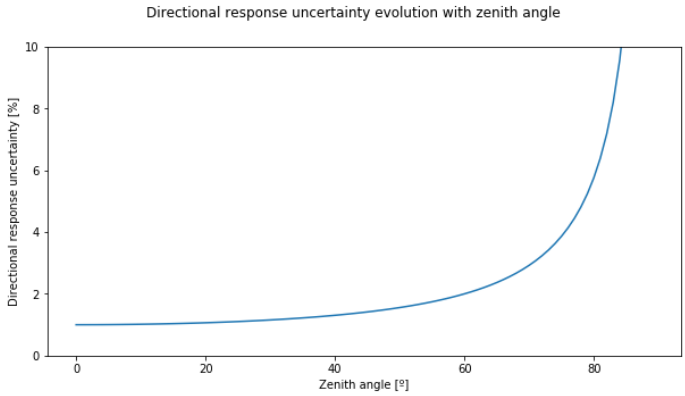

Figure B.1: Directional response uncertainty as a function of the zenith angle.

Once all the sources of uncertainty were characterized, they have been summarized in Table B.3 as well as the assumptions taken on their uncertainty category, distribution and shape.

Table B.3: Summary of uncertainty contributions for the MS-802F pyranometer

Uncertainty source	Parameter	Specification limit	Type	Distribution	Shape
Data logger accuracy	E	0.08 %	B	Rectangular	Symmetric
Calibration uncertainty	S	2.2 %	B	normal (k=2)	Symmetric
Long-term stability	S	0.5 %	B	Rectangular	One-sided (negative)
Non-linearity	S	0.2 %	B	Rectangular	Symmetric
Directional Response	S	$\frac{10}{1000 \cdot cos(\theta_z)}$	B	Rectangular	Symmetric
Spectral response	S	1 %	B	Rectangular	Symmetric
Temperature response	S	1 %	B	Rectangular	Symmetric
Maintenance	S	0.5 %	B	Rectangular	Symmetric
Zero Off-set A[1]	I	6 W/m^2	B	Rectangular	One-sided (negative)
Zero Off-set B[1]	I	2 W/m^2	B	Rectangular	Symmetric

[1] Zero off-sets were not considered for the uncertainty calculations

Even though the shape of some sources of uncertainty have been defined as one-sided, they have been doubled and treated as symmetric to simplify the uncertainty assessment. All the different sources have been considered uncorrelated for the same reason. To calculate the expanded uncertainty of the sensitivity, root-sum-of-squares (RSS), also known as the *law of propagation of uncertainty*, has been applied to all sensitivity related parameters[49]. Table B.4 summarizes how to calculate the standard uncertainty for both variables in the measurement equation.

Table B.4: Standard uncertainties for the measurement equation parameters of the MS-802F.

Variable	Distribution	Coverage Factor	$\%U_{95}$	U_{95}	u
Output voltage (E)	Rectangular	$\sqrt{3}$	0.08 %	($e^1 \cdot 0.0008$)	$(e \cdot 0.0008)/\sqrt{3}$
Sensor's sensitivity (S)	Normal	1.96	RSS_S[2] %	(S· RSS_S)	(S· RSS_S)/1.96

[1] Where e represents the measured output voltage (E) [2] Where RSS_S represents the root-sum-of-squares of the uncertainty sources related with the sensor's sensitivity. It includes directional responses and therefore it varies as a function of the zenith angle

B.3 Combined standard uncertainty

In order to get combined standard uncertainty, sensitivity factors (c) must be calculated. It is calculated for each variable of the measurement equation as the partial derivative of the global solar irradiance (I) with respect to the variable as follows [46][49]:

$$c_E = \frac{\partial I}{\partial E} = \frac{1}{S} \tag{B.2}$$

$$c_S = \frac{\partial I}{\partial S} = -\frac{E}{S^2} \tag{B.3}$$

The combined standard uncertainty for type B uncertainties (u_B) is:

$$u_B = \sqrt{\sum_{j=1}^{n} (c_j \cdot u_j)^2} \tag{B.4}$$

Where j is the variable and n the number of variables.

After applying the standard uncertainties to Equation B.4, and since there are no type A uncertainties and the sensitivity is assumed constant, the combined uncertainty (u_C) can be expressed as:

$$u_C = \sqrt{\cancelto{0}{(u_A)^2} + (u_B)^2} = \sqrt{(c_E \cdot u_E)^2 + (c_S \cdot u_S)^2} \tag{B.5}$$

$$u_C = \sqrt{(0.141 \cdot \frac{0.0008}{\sqrt{3}} \cdot e)^2 + (-0.141 \cdot \frac{RSS_S}{1.96} \cdot e)^2}$$

As it can be seen, the combined uncertainty is a function of the voltage measured (e) and the RSS of the sensitivity's standard uncertainty contributors, since the sensitivity itself is a constant value.

B.4 Expanded uncertainty

For a confidence level of 95%, expanded uncertainty can be calculated as follows:

$$U_{95} = k \cdot u_C \tag{B.6}$$

In order to get the coverage factor (k), the effective degrees of freedom has to be calculated first. It is calculated with the following equation:

$$DF_{B,eff} = \frac{(u_B)^4}{\sum_{j=1}^{n} \frac{(c_j \cdot u_j)^4}{df_j}} \tag{B.7}$$

Since E has infinite degrees of freedom and the S has more than 500 data points, the effective degrees of freedom is considered equal to infinite, and therefore, from the student "t" tables a coverage factor equal to 1.96 has been obtained. Therefore, the final expanded uncertainty (in W/m^2) can be expressed as follows:

$$U_{95} = 1.96 \cdot u_C \tag{B.8}$$

B.5 Application of the uncertainty measurement

Uncertainty has been assessed for two different cases: one sunny day in the summer time, and one sunny day in the winter time. In Figure B.2 it can be seen how the uncertainty evolves during a sunny summer day (B.2a) with a minimum uncertainty of 2.82% at noon, while this value is equal to 4.37% for same condition on a sunny winter day (B.2b).

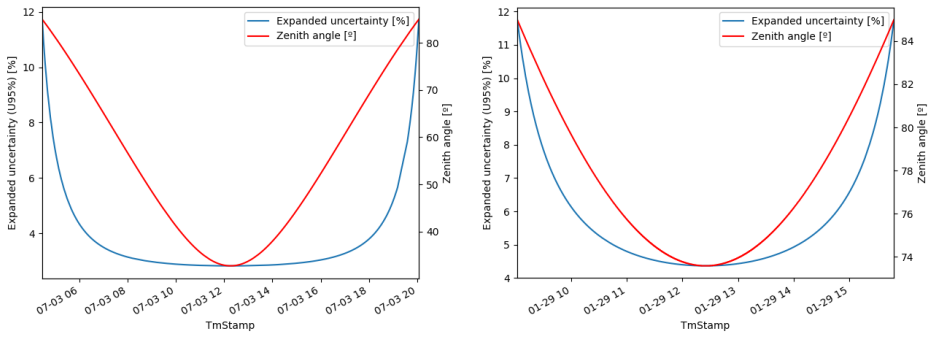

(a) Summer day - 3rd July 2018 (b) Winter day - 29th January 2019

Figure B.2: Evolution of the uncertainty in the GHI measurement for two sunny days

APPENDIX C

MDPD plots and graphs.

In this appendix extra graphs and plots regarding the MDPD study described in Chapter 5 are presented.

C.1 MDPD north sensor additional plots

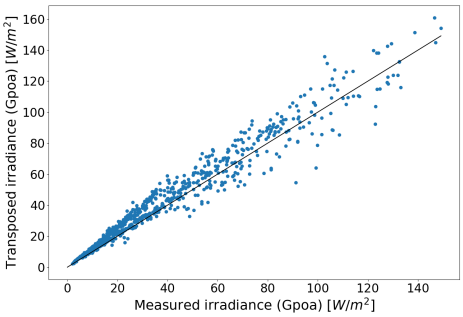

(a) Isotropic (Liu & Jordan) model

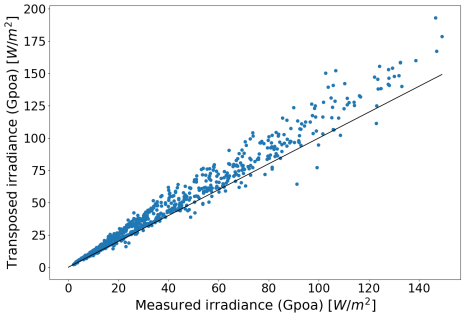

(b) Klucher model

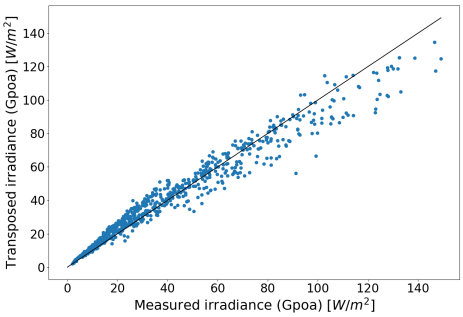

(c) Perez model

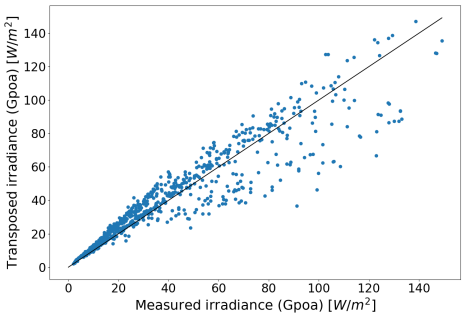

(d) Hay & Davies model

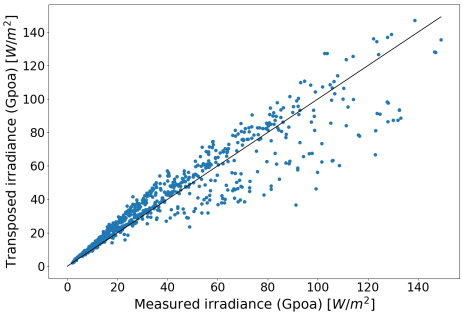

(e) Reindl model

Figure C.1: Comparison between the MDPD north sensor measured irradiance and transposed to that surface

C.2 MDPD south sensor additional plots

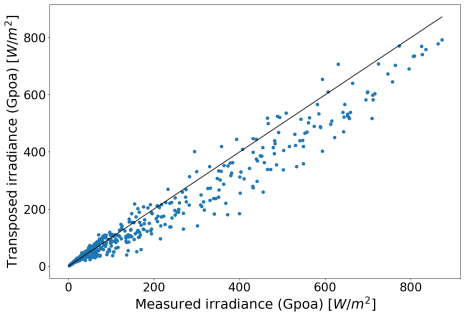

(a) Isotropic (Liu & Jordan) model

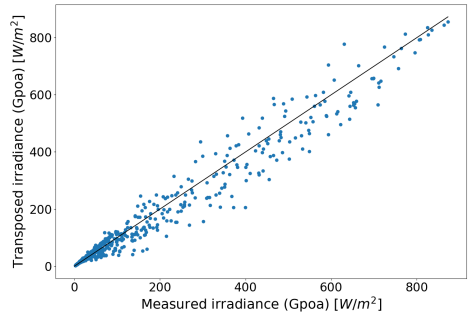

(b) Klucher model

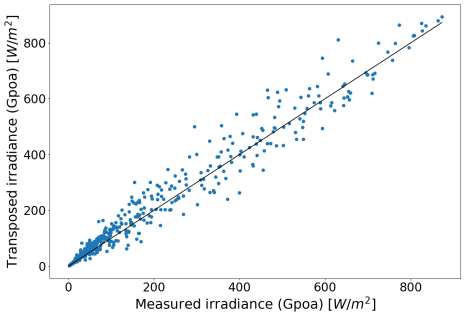

(c) Perez model

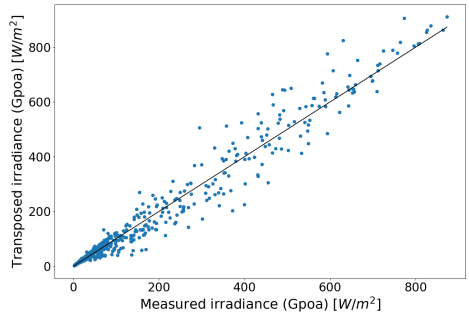

(d) Hay & Davies model

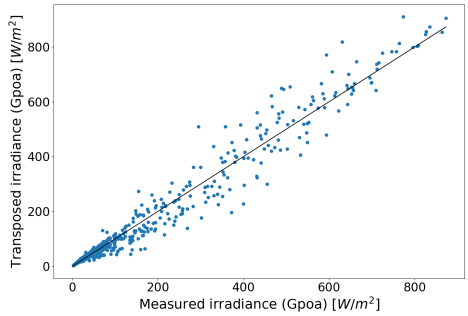

(e) Reindl model

Figure C.2: Comparison between the MDPD south sensor measured irradiance and transposed to that surface

C.3 MDPD east sensor additional plots

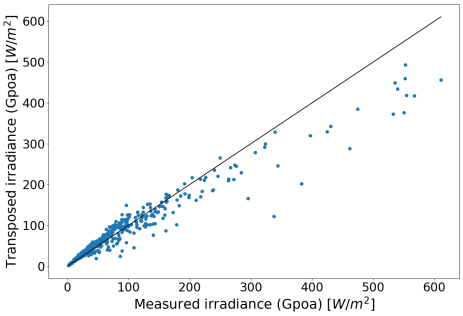

(a) Isotropic (Liu & Jordan) model

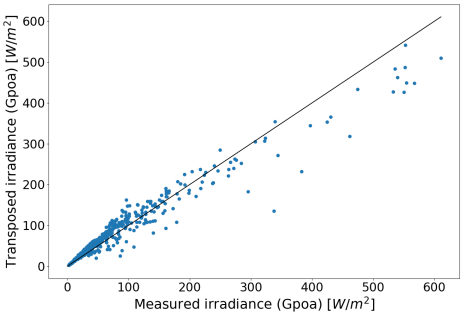

(b) Klucher model

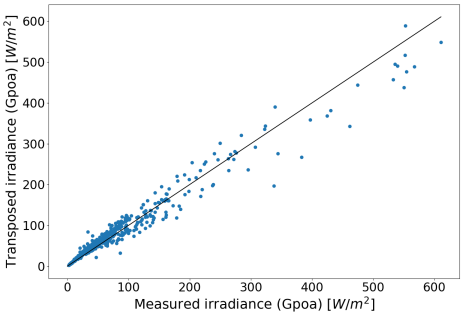

(c) Perez model

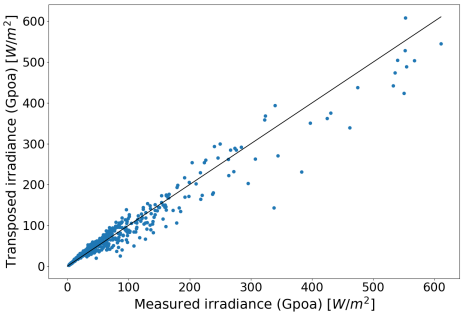

(d) Hay & Davies model

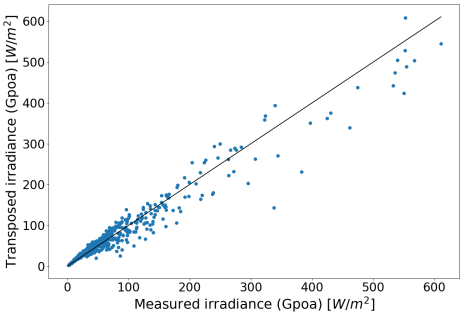

(e) Reindl model

Figure C.3: Comparison between the MDPD east sensor measured irradiance and transposed to that surface

C.4 MDPD west sensor additional plots

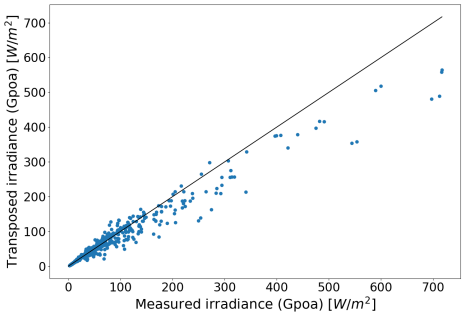

(a) Isotropic (Liu & Jordan) model

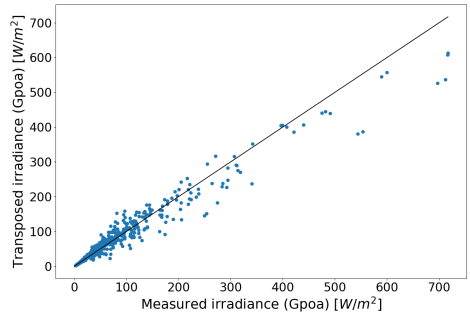

(b) Klucher model

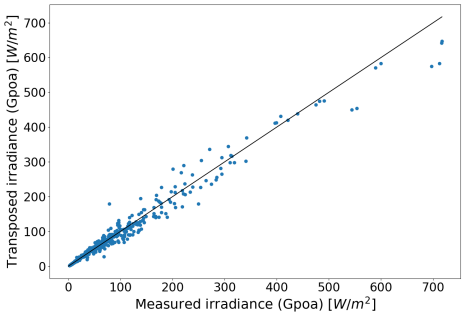

(c) Perez model

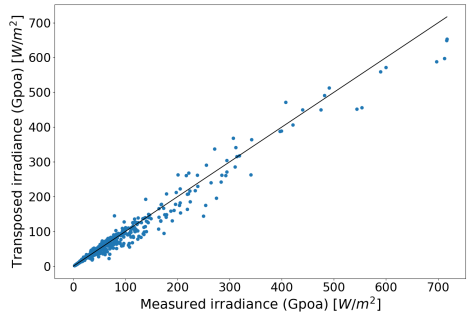

(d) Hay & Davies model

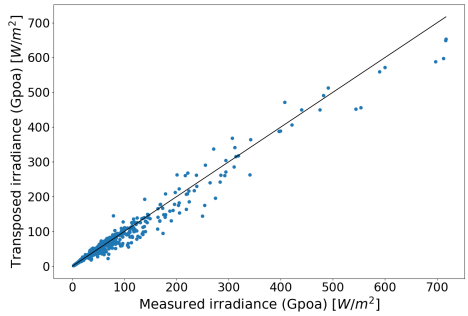

(e) Reindl model

Figure C.4: Comparison between the MDPD west sensor measured irradiance and transposed to that surface

APPENDIX D

Uncertainty calculations II: MDPD uncertainty in measurement assessment. Process and results.

In this appendix the process followed to calculate the uncertainty in the measurements of the MDPD sensors and the GHI fast-silicon sensor (both are ML-02 Si-Pyranometer) is detailed.

D.1 Measurement equation

The MDPD device manufactured by EKO Instruments is composed of six silicon pyranometers (ML-02) also manufactured by them. Same sensor is used to measure GHI at the main weather station. These low-profile pyranometer uses the same equation as the previous studied pyranometer(MS-802F):

$$I(W/m^2) = \frac{E(\mu V)}{S(\mu V/(W/m^2))} \tag{D.1}$$

Where E represents the output voltage and S the pyranometer sensitivity which is determined by calibration. Both have been considered independent with no correlation since different methods are used to measure or calculate them.

D.2 Standard uncertainties

Theoretical explanations and terminology has been described in Appendix B therefore, only the most important steps of the process and results will be presented.

As considered for the MS-802F pyranometer, both parameters in the measurement equation have been assumed category B uncertainty contributors (non-statistical).

1. **Uncertainty in the output voltage (E) measurement**. Same data logger (Campbell Scientific's CR6 model) as the one described for MS-802F pyranometer is used, which expanded uncertainty calculated for the voltage range used is equal to 0.08 %.

2. **Uncertainty in the pyranometer's sensitivity (S)**. The MDPD was recently manufactured. Therefore, a sensitivity of 50 ($\mu V/(W/m^2)$) listed in the manufacturer's datasheet has been used.

Uncertainty contributors for the sensitivity have been assumed in the same way as in Appendix B, excluding the directional response. Directional response as a function of incident angle has been given by the manufacturer and can be seen represented in Figure D.1.

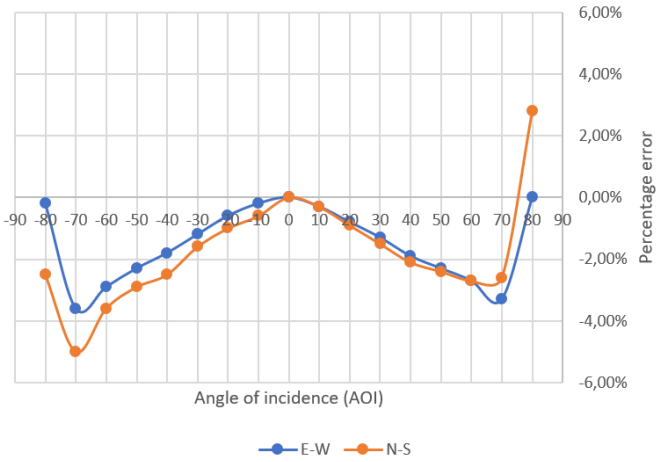

Figure D.1: Laboratory measurements of the directional response error as a function of the angle of incidence.

The E-W curve is more representative of the typical behavior of the sensors, hence its values were used. Since it is symmetric, it was averaged for the absolute values of the AOI and an interpolation function was made to be able to fit any AOI within the interval 0-80°(Figure D.2). These values were used to calculate the contribution of the directional response to the sensitivity's standard uncertainty. For greater AOI than 80°it was considered that no direct irradiance is measured and therefore, no directional response involved.

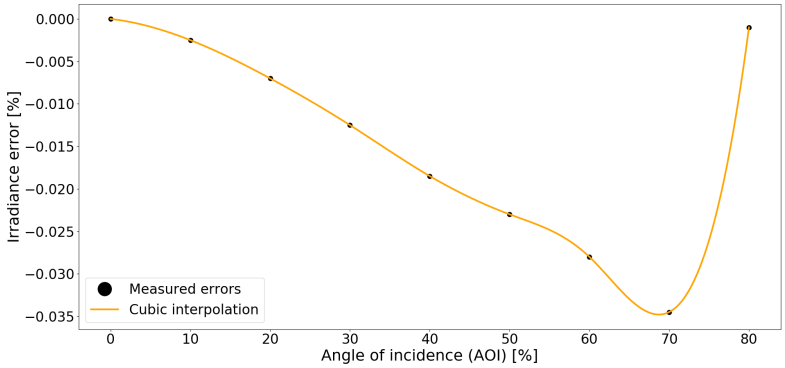

Figure D.2: Directional response contribution to the sensitivity's uncertainty as a function of the angle of incidence.

Considered sources of uncertainty are summarized in Table D.1.

Table D.1: Summary of uncertainty contributions

Uncertainty source	Parameter	Specification limit	Type	Distribution	Shape
Data logger accuracy	E	0.08 %	B	Rectangular	Symmetric
Calibration uncertainty	S	1.7[1] %	B	normal (k=2)	Symmetric
Long-term stability	S	2 %	B	Rectangular	One-sided (negative)
Non-linearity	S	0.2 %	B	Rectangular	Symmetric
Directional Response	S	f(AOI)[1]	B	Rectangular	Symmetric
Spectral response	S	3.07 %	B	Rectangular	Symmetric
Temperature response	S	0.15 %/°C	B	Rectangular	Symmetric
Maintenance	S	0.5 %	B	Rectangular	Symmetric
Zero Off-set A	I	0 W/m^2	B	Rectangular	One-sided (negative)
Zero Off-set B	I	0 W/m^2	B	Rectangular	Symmetric

[1] Given by external supervisor

Similarly to Appendix B all sources were considered symmetric and uncorrelated. The expanded uncertainty of the sensitivity was calculated as the RSS of its uncertainty contributors as well. Table D.2 shows how to calculate standard uncertainty for the output voltage and the sensitivity.

Table D.2: Standard uncertainties for the measurement equation parameters.

Variable	Distribution	Coverage Factor	$\%U_{95}$	U_{95}	u
Output voltage (E)	Rectangular	$\sqrt{3}$	0.08 %	(e[1] · 0.0008)	(e · 0.0008)/$\sqrt{3}$
Sensor's sensitivity (S)	Normal	1.96	RSS_S[2] %	(S· RSS_S)	(S· RSS_S)/1.96

[1] Where e represents the measured output voltage (E) [2] Where RSS_S represents the root-sum-of-squares of the uncertainty sources related with the sensor's sensitivity. It includes directional responses and therefore it varies as a function of the zenith angle

D.3 Combined standard uncertainty

Sensitivity factors (c) as described in Appendix B.3 were calculated for both equation parameters in order to be able to calculate the combined standard uncertainty (u_C). It can be expressed as follows:

$$u_C = \sqrt{(c_E \cdot u_E)^2 + (c_S \cdot u_S)^2} \tag{D.2}$$

$$u_C = \sqrt{(\tfrac{1}{S} \cdot \tfrac{0.0008}{\sqrt{3}} \cdot e)^2 + (\tfrac{-e}{S^2} \cdot \tfrac{S \cdot RSS_S}{1.96} \cdot e)^2}$$

$$u_C = \sqrt{(0.02 \cdot \tfrac{0.0008}{\sqrt{3}} \cdot e)^2 + (-0.02 \cdot \tfrac{RSS_S}{1.96} \cdot e)^2}$$

As it can be seen, the combined uncertainty is a shown as a function of the out voltage measured (e) and the RSS of the sensitivity's standard uncertainty contributors, since the sensitivity itself is a constant value. The RSS is calculated as a function of the AOI and the sensor's temperature difference with the calibration temperature

(assumed to be equal to 25°C).

D.4 Expanded uncertainty

Expanded uncertainty with a confidence level of 95% can be calculated as follows:

$$U_{95} = k \cdot u_C \tag{D.3}$$

Same conditions regarding the degrees of freedom were applied in this case, therefore same coverage factor used (equal to 1.96). Obtaining a final expanded uncertainty equal to:

$$U_{95} = 1.96 \cdot u_C \tag{D.4}$$

Expanded uncertainty as a function of the AOI and sensor temperature was calculated for each sensor of the MDPD and the ML-02 used for GHI.

{2.7182818284}